Order Number 8920677

Computation of nonequilibrium chemically reacting flows in hypersonic flow field

Chiang, Ting-Lung, Ph.D.

The University of Texas at Austin, 1989

U·M·I
300 N. Zeeb Rd.
Ann Arbor, MI 48106

COMPUTATION OF NONEQUILIBRIUM CHEMICALLY REACTING FLOWS IN HYPERSONIC FLOW FIELD

by

Ting-Lung Chiang, B.S., M.S.

DISSERTATION

Presented to the Faculty of the Graduate School of

The University of Texas at Austin

in Partial Fulfillment

of the Requirements

for the Degree of

DOCTOR OF PHILOSOPHY

THE UNIVERSITY OF TEXAS AT AUSTIN

May 1989

COMPUTATION OF NONEQUILIBRIUM CHEMICALLY REACTING FLOWS IN HYPERSONIC FLOW FIELD

APPROVED BY

SUPERVISORY COMMITTEE:

John D. Anderson

Parker Lamb

D S Dolling

Klaus A. Hoffmann

C P Li

To my Parents for their love, understanding and encouragement, and in memory of Lih-Wei Chen.

Acknowledgments

The author wishes to express his sincere appreciation to Dr. John J. Bertin and Dr. Klaus A. Hoffmann who led him to this field of research and provided encouragement and guidance. Heartfelt gratitude goes to Dr. Klaus A. Hoffmann, Mr. Walter H. Rutledge and Mrs. Karen K. Rutledge for the precious friendship they bring to the author. Without their friendship the author could not have restored his courage on those difficult days he had and this dissertation would not have been completed. Also, most of the editing work of this dissertation has been done with their help. The author would like to express his thanks to Dr. David S. Dolling, Dr. J. Parker Lamb, Jr. and Dr. Chien-Peng Li for serving as his committee; and special thanks to Mrs. Jeanie Paterson for her skillful and efficient typing and her assistance in editing. Finally, the author would like to express his gratitude to all who have helped him in these years. With their kindness, this dissertation is completed.

Ting-Lung Chiang

The University of Texas at Austin

May 1989

COMPUTATION OF NONEQUILIBRIUM CHEMICALLY REACTING FLOWS IN HYPERSONIC FLOW FIELD

Publication No. _____

Ting-Lung Chiang, Ph.D.

The University of Texas at Austin, 1989

Supervising Professors: Dr. J. J. Bertin and Dr. K. A. Hoffmann

In recent years a renewed interest in the design of various hypersonic vehicles has necessitated the inclusion of chemically reacting flows for the solution of hypersonic flowfields. From the physical point of view, all chemical reactions take some time to reach equilibrium state. Therefore, finite-rate (nonequilibrium) chemistry models must be utilized for hypersonic flowfield computations. A compelling difficulty in the numerical simulation of chemically reacting flow is the selection of the marching time step. Usually the characteristic time scale of the gas dynamic equations is different from that of the chemistry equations. A numerical algorithm that determines the chemistry marching time step is developed in this investigative work. Von Neumann stability analysis is applied to the chemistry equations to provide a criteria for the selection of time step for a stable solution. Both the quasi one-dimensional nozzle problem and the two-dimensional/axisymmetric blunt body problem are used for numerical validation. Unsteady Euler equations and chemistry equations are written in the conservative form so that the shock capturing scheme

can be applied. A five species model is selected for the air compositions. The governing equations are discretized by an implicit, flux-splitting finite difference formulation to provide a better stability characteristic and faster convergence. The gas dynamic equations and chemistry equations are solved interactively and communicated by the loosely-coupled scheme.

Table of Contents

List of Tables

List of Figures

Nomenclature

a	speed of sound
CFL	Courant-Friedricks-Lewy number
C_s	mass-fraction of species s
D	Damkohler number
e	internal energy per unit mass
e_t	total internal energy per unit mass
G_{ex}	(explicit) stability amplification factor
h	enthalpy
$h_{o,s}$	heat of formation of species s
h_t	total enthalpy
J	coordinate transformation Jacobian $= \xi_x \eta_y - \xi_y \eta_x$
K_b	backward reaction rate
K_e	equilibrium constant
K_f	forward reaction rate
L	characteristic length
M_s	molecular weight of species s
P	pressure
P_c	critical pressure
P_r	reduced pressure
R	mixture gas constant
R_u	universal gas constant
S	cross-sectional area of nozzle
T	temperature
T_c	critical temperature
T_r	reduced temperature
u	x-component velocity in physical domain
U	ξ-component velocity in computational domain, i.e., $U = u\xi_x + v\xi_y$

v	y-component velocity in physical domain
V	η-component velocity in computational domain, i.e., $V = u\eta_x + v\eta_y$
$\dot{w}_s$	mass-production rate of species s
X	eigenvector matrix of convective Jacobian
X^{-1}	inverse of X
$[X_s]$	concentration of species s (i.e., mole number per unit volume)
z	compressibility factor of gas

Greek Symbols

α	$\left\{ \begin{array}{l} = 0 \text{ for two-dimensional planar flow} \\ = 1 \text{ for two-dimensional/axisymmetric flow} \end{array} \right\}$
γ	variable, defined by $\gamma = h/e$
Δt_c	time step for chemistry equations, dimensional form
Δt_e	time step corresponds to $G_{ex} = 1$
Δt_g	time step for gas dynamic equations, dimensional form
Δx	grid spacing in x direction
$\Delta\tau$	time step for gas dynamic equations, nondimensional form
ϵ	prescribed convergence criterion value, or error in the von Neumann analysis
$\epsilon_{e,s}$	electronic mode of internal energy of species s
$\epsilon_{o,s}$	zero-point energy of species s
$\epsilon_{r,s}$	rotational mode of internal energy of species s
$\epsilon_{t,s}$	translational mode of internal energy of species s
ϵ_s	internal energy of species s
$\epsilon_{v,s}$	vibrational mode of internal energy of species s
$\Delta\eta$	grid spacing in η direction
θ	collision frequency of gas
θ_s	characteristic temperature of species s

λ	eigenvalue of convective Jacobian
$\Delta\xi$	grid spacing in ξ direction
Π	product symbol
ρ	density of mixture

Subscripts

∞	free stream conditions
c	property corresponds to chemistry equations
s	property corresponds to species s

Superscripts

+ (positive)	properties correspond to positive eigenvalues of convective Jacobian
− (negative)	properties correspond to negative eigenvalues of convective Jacobian
— (bar)	properties in the computational domain
*	nondimensional properties, or intermediate solution
n	transient solution at time level n, (i.e., with values known)
$n+1$	transient solution at time level $n+1$ (i.e., with values being sought)

Chapter 1

Introduction

The investigation of hypersonic flow fields can be traced back to the 1950's, during the early design of intercontinental ballistic missiles. Subsequent re-entry vehicle development programs and the initiation of manned space programs continued the study of hypersonics through the late 1960's. Current interest in the AOTV (Aero-assisted Orbital Transfer Vehicle) [1,2] and NASP (National Aero-Space Plane) [3,4,5] requires accurate information on the entire flow field so that the thermal protection systems, propulsion systems, and control systems can be properly designed. For these hypersonic vehicles, which may reach velocities as high as 32 kft/sec (for AOTV) [6,7], blunt noses and leading edges are required to reduce the aerodynamic heating. Therefore, the ability to accurately calculate the hypersonic flow field about a blunt body is very important, both for the aerodynamic and for the thermodynamic analysis.

For the hypersonic blunt body flow, there is always a detached strong shock; and the flow is decelerated to subsonic speed in the nose region. The temperature distributions in the vicinity of the stagnation region evaluated by the calorically perfect gas model (ideal gas model) will yield extremely high values. However, the actual physical temperature is indeed much lower than the predicted values by the ideal gas model.

The reason for this phenomenon is that for the flow behind the strong

shock, a large portion of kinetic energy of the free stream is changed into the form of internal energy. The internal energy for the molecule is composed of translational, rotational, vibrational and electronic energies (according to the quantum mechanics theory [8]); and each of these energies can exist only at certain discrete values (i.e., they are quantized). If the vibrational mode of the molecule is strongly excited (i.e., the vibrational energy is very large), the molecule might simply break into atoms. This dissociation process will absorb a large amount of internal energy and will change the energy into the "heat of formation". As a result, the total amount of internal energy in the form of translational, rotational, and vibrational modes (if the electronic mode is ignored) is decreased. Therefore, the temperature is much lower than the values evaluated by the ideal gas model (since the ideal gas model does not include this chemically reacting effect). Basically, the ideal gas model is just a simple model of the frozen flow. It does not consider the vibrational mode of energy, only the translational and rotational modes.

Since the temperature distribution will effect the boundary layer properties, the aerodynamic properties (i.e., skin friction, drag force, ...) and thermodynamic properties (i.e., heat transfer coefficient) are very sensitive to the temperature distribution. The effect of chemically reacting flows on the pressure distribution is secondary. The flight data of the U.S. Space Shuttle has indicated a much higher pitching moment than predicted by the ideal gas inviscid flow field calculations [9]. The reason for this discrepancy is due to the effects of a chemically reacting shock layer. With an "equilibrium" chemistry model, the pressure distribution along the shuttle surface provides a much more accurate pitching moment than predicted by the ideal gas model, although the

difference in the pressure distributions by the two models is small.

Therefore, from the phenomena just described, it is obvious that the chemistry effects for the hypersonic flow field investigations cannot be ignored. During the 1950's and 1960's, Newtonian and Modified Newtonian theories were popular methods used to evaluate the surface pressure distributions for the hypersonic blunt body flows. Today, due to their simplicity, these methods are still useful in providing a conceptual picture for preliminary design work. Other approximate methods have been developed to provide better solutions for engineering practice. Such methods are the "constant density theory" and the "thin shock layer theory" [10]. However, all these approximate methods can be used only on simple configurations, such as sharp cone, slender blunt bodies, wedges, etc.

For complex configurations, the approximate methods do not provide satisfactory solutions. A comparison of the local drag force evaluated by the modified Newtonian theory and an ideal gas Euler equations shows an error of about 35% for a dented configuration [11]. Therefore, a method which provides accurate shock structure and pressure distributions is required for hypersonic flow problems.

Moretti [12] developed a "time-dependent technique" in 1966 which successfully solved a blunt body flow. The "time-dependent technique" works by solving the unsteady governing equations with arbitrary initial conditions throughout the computational domain, whether or not the flow is locally subsonic (elliptic type equation for steady problem) or supersonic (hyperbolic type equation for steady problem). The reason is that the unsteady governing equa-

tions are hyperbolic with respect to time; therefore, a time marching scheme is employed. A steady state solution is approached for a large number of time steps.

The equations of motion are solved numerically within a domain defined by the body and an outer boundary. There are two methods to prescribe the outer domain; they are the "shock fitting" method and the "shock capturing" method. The shock fitting method, presented by Gary [13], uses the bow shock as the outer boundary of the computational domain, and was used to solve supersonic blunt body flow by Moretti and Abbett [12] and by Moretti and Bleick [14].

In applying the shock fitting method, *a priori* knowledge about the shock shape and location is needed/assumed, which may be accomplished by extrapolation. Subsequently, the Rankine-Hugoniot equations are used to update the post-shock properties.

When the outer boundary is extended far into the free stream such that the bow shock as well as any other internal shocks are predicted as a part of the overall solution, it is referred to as "shock capturing". For this purpose, the governing equations must be expressed in conservative law form. Some disadvantages of shock capturing are: (a) the shock waves captured by this scheme are somewhat smeared over a few mesh intervals; (b) the grid points in the free stream are essentially wasted insofar as useful flow field information is concerned. Nevertheless, the simplicity of the "capturing" method outweighs the weaknesses mentioned and is adopted in this research work. Also, it is emphasized that shock fitting procedures are usually explicit and, therefore,

introduce additional stability constraints, whereas shock capturing scheme used in this investigation do not impose additional stability requirements.

In considering the high temperature chemistry effects, an important point to recognize is the very different flight regime of the hypersonic vehicles. A typical flight regime for the AOTV includes altitudes of 500,000 ft. to 250,000 ft. with velocities of 32 kft/sec to 24 kft/sec. Whereas for the NASP, the flight regime will be from earth's surface to an altitude of 250,000 ft. with velocities of up to 27 kft/sec. The very different altitudes and velocities will influence the post-shock properties (pressure, density, temperature, ...etc.) of the fluid by several orders of magnitude. Thus, the chemical reactions in the shock layer behave in a very different manner for the two vehicles.

A molecule cannot dissociate before it is fully vibrationally excited. The vibrational excitation process is performed by molecular collisions and, therefore, the molecular collision is the most important issue in the chemical reacting process. However, the collision process takes time to occur. If the fluid element has enough time for the necessary number of collisions to occur under the local pressure and temperature, then it is called the "equilibrium system". In some cases, however, the fluid element passes through the shock front too quickly. As a result, gas does not have enough time to acquire the collisions for the "equilibrium state" under the local pressure and temperature. This phenomenon is then called "nonequilibrium state". So "equilibrium" or "nonequilibrium" is determined by comparing the time scale for the chemical reaction rate and the time scale for the fluid to pass the region of interest. One way to measure (describe) the degree of nonequilibrium is by using the Damkohler number [15] $D = \ell/(U\tau_c)$, where ℓ, U, and τ_c are characteristic

length, velocity, and chemical conversion time, respectively, and τ_c can be expressed as a curve fitting function (Gnoffo [16]).

From the Damkohler number, it is seen that the body geometry/size (ℓ), velocity (U), and density/temperature (related with τ_c) are all very important for the determination of whether the flow is "equilibrium" or "nonequilibrium".

Also, the inverse of the collision frequency is a way to measure the time needed for the molecular collision and the collision frequency, $\theta\alpha\rho\sqrt{T}$ [8]. Therefore, for high altitude (low ρ) and low velocity (low T in the shock layer) flight, the chemistry effects will be closer to the nonequilibrium state, and vice versa.

For flow fields with a large Damkohler number (chemical time scale is much less than the gas dynamic time scale), an "equilibrium chemistry model" (where the chemical reaction rate is infinite) can be used [17–19] to perform the chemistry effects. Otherwise, a "finite rate (nonequilibrium) model" should be used to reveal the non-equilibrium effects.

Generally speaking, for low altitude (below 60 km) hypersonic problems, the equilibrium formulation can be employed. However, since all the chemical reactions are finite rate, the nonequilibrium formulation is still applicable for such problems. The only consideration is computation time, as the nonequilibrium model is more time-consuming than the equilibrium model. For high altitude hypersonic problems, the nonequilibrium model is the only one which may be used. Note that even for the low altitude problems, it is possible to have some "locally" nonequilibrium regions within the shock layer

where the use of an equilibrium model cannot predict this effect. Therefore, the nonequilibrium model is a more general formulation and is more flexible for the hypersonic problems.

Early works on the nonequilibrium chemistry effects were related to one-dimensional flow problems, e.g., the nozzle flow or the shock tube problems. These works have developed rather well the theory and ideas of the nonequilibrium problems [20].

Blottner [21,22] applied the nonequilibrium model in solving the boundary layer equations by using an implicit finite difference formulation. Moss [23] used the viscous shock layer equations developed by Davis [24], with a shock fitting method, to solve the 2-D/Axisymmetric nonequilibrium chemically reacting flows. In Blottner's [21] numerical investigation where a cone with a speed of 21,000 fps at 100,000 ft. altitude (i.e., low altitude) is used, the flow remained in nonequilibrium state within a 60 ft. distance from the nose tip. This result suggests that one should employ the nonequilibrium model even at low altitudes. In the investigation of Moss [23], the nonequilibrium model produces (1) a thicker thermal boundary layer compared to that of the ideal gas model (frozen flow), (2) less aerodynamic heating effects on the downstream of the body, (3) a smaller shock stand-off distance, and (4) a reduced skin friction (C_f).

Two approaches are used to include the finite rate chemistry effects into the hypersonic flow calculation. One is to solve both the gas dynamic equations (Navier-Stokes or Euler) and the chemistry equations simultaneously. This is called the "coupled method" [25, 26, 27, 28]. The second approach is to

solve the two sets of equations separately and iteratively. It is called the "loosely coupled method" or "chemistry-split" technique [29, 30, 31, 32]. The coupled method can offer a faster convergence and accounts fully for all the nonequilibrium effects. Candler [33] used this method to solve the Navier-Stokes equations with both nonequilibrium thermodynamics (multi-temperature model) and nonequilibrium chemistry. However, the coupled method will result in a complex, large block matrix system. The inversion of the large matrices is very (computer) time consuming, especially when there is a large number of chemical species. On the other hand, the loosely coupled method allows for easy addition or deletion of species without any changes in the finite difference formulation of the gas dynamic equations. Thus, many existing gas dynamic codes (written with the ideal gas model) can be easily modified to include the chemistry effects by the loosely coupled method. To do this, the "variable effective gamma" method (Gnoffo [34]) or the "β-method" (Balakrishnan [31, 35]) can be utilized to relate the two different sets of equations. The weaknesses in the loosely coupled approach are: first, it is numerically less stable; secondly, it is not well-suited for solving real-time problems. However, it is very flexible and works well for the steady-state problems.

One of the most difficult problems encountered in solving chemistry equations is the "stiffness problem." This means that the source terms (mass production rate terms) in the chemistry equations are sometimes too large as compared with the convective terms. As a result, the relaxation time step is very small compared with the time step used in the gas dynamic equations. Hence, a time step based on the converging CFL number of gas dynamic equations may be too large for the chemistry equations, thus resulting in an unstable

solution.

Glaz [36] suggested that the solution was to "make the spatial mesh in the reaction region small enough to bring the two time scales into balance". Basically, this requires one to decrease the time step used in the gas dynamic equations (for a fixed CFL number).

Palmer [37] noted that the mass production rate terms can sometimes be large relative to the flux terms and cause nonphysical species densities, (e.g., negative species density). He used a "scaling coefficient" (approximately 0.0004) to reduce the "global time step" and used the reduced "effective time step" in the chemistry equations. However, by doing so, the time accurate solution cannot be achieved even with the coupled scheme. Therefore, it is important to understand how the source terms effect the stability of the chemistry equations and how to decide on a marching time step that can be used to approach a converged solution. Park [38] used a simple scalar chemistry equation to explain how the source term influences the stability of the problem, and developed a criterion for a stable time step both for the explicit and implicit (for source term) formulations.

The objective of the current research is to provide some mathematical insight for the chemical source terms, such as how they produce the "stiff" problem, and how to decide the time step required in assuring a converged solution. The analysis employs the von Neumann stability analysis. The criterions are tested first in a quasi one-dimensional nozzle flow problem, and subsequently extended to a two-dimensional/axisymmetric blunt body problem. Due to computer memory and time restrictions, Euler equations are used.

A nonequilibrium chemistry model is employed which is loosely coupled with the gas dynamic equations. An implicit finite difference formulation is utilized to discretize the original partial differential equations, and the flux-splitting method is used to avoid the introduction of the artificial viscosity.

Chapter 2

Euler Equations

2.1 Introductory Remarks

To solve for a physical flow problem, the Navier-Stokes equations can provide the most satisfactory solutions. However, inclusion of the viscous and heat transfer terms requires large computation times and a very large memory. In addition, a large number of grid points is required within the boundary layer to assure both the accuracy and convergence of the numerical solution. Therefore, to solve the Navier-Stokes equations is sometimes impractical and unnecessary for many preliminary design analyses or the investigation of numerical methodology.

Without the viscous and heat transfer terms, Euler equations can economically provide useful information about the pressure and temperature distributions outside the boundary layer. Therefore, to investigate numerical schemes and to include chemically reacting flows, Euler equations were selected.

In this chapter, the flux-splitting method is employed to solve the implicitly formulated, unsteady Euler equations. Both the quasi one-dimensional nozzle problem as well as the two-dimensional/axisymmetric blunt body problem are considered.

2.2 Quasi One-Dimensional Euler Equations

The Euler equations for a quasi one-dimensional flow may be expressed as:

continuity,

$$\frac{\partial}{\partial t}(\rho S) + \frac{\partial}{\partial x}(\rho u S) = 0 \tag{2.1}$$

momentum,

$$\frac{\partial}{\partial t}(\rho u S) + \frac{\partial}{\partial x}[(\rho u^2 + P)S] - P\frac{dS}{dx} = 0 \tag{2.2}$$

energy,

$$\frac{\partial}{\partial t}(\rho e_t S) + \frac{\partial}{\partial x}[(\rho e_t + P)uS] = 0 \tag{2.3}$$

where S is the cross-sectional area assumed independent of time, i.e., $S = S(x)$, and

$$e_t = e + \frac{1}{2}u^2 \tag{2.4}$$

Equations (2.1) through (2.3) are expressed in a flux vector form as

$$\frac{\partial}{\partial t}(SQ) + \frac{\partial E}{\partial x} - H = 0 \tag{2.5}$$

where

$$Q = \begin{bmatrix} \rho \\ \rho u \\ \rho e_t \end{bmatrix}, \quad E = S\begin{bmatrix} \rho u \\ \rho u^2 + P \\ (\rho e_t + P)u \end{bmatrix}, \quad \text{and} \quad H = \frac{dS}{dx}\begin{bmatrix} 0 \\ P \\ 0 \end{bmatrix}$$

Now, consider an implicit finite difference algorithm for equation (2.5). The time derivative is approximated by a first-order backward difference ap-

proximation to provide

$$S\frac{Q^{n+1}-Q^n}{\Delta t}+\left(\frac{\partial E}{\partial x}\right)^{n+1}-H^{n+1}=0 \tag{2.6}$$

Since an implicit formulation is sought, second and third terms have been expressed at the $n+1$ time level. The change in flow properties per time step is defined as

$$\Delta Q = Q^{n+1}-Q^n$$

The FDE shall be formulated in terms of ΔQ, which is referred to as the delta formulation. Since equation (2.5) is nonlinear, a linearization procedure is adapted.

Consider a Taylor series expansion about time level n as follows:

$$E^{n+1}=E^n+\frac{\partial E}{\partial t}\Delta t+O(\Delta t)^2 \tag{2.7}$$

Since $E=f(Q,S)$, the chain rule of differentiation yields

$$\frac{\partial E}{\partial t}=\frac{\partial E}{\partial Q}\frac{\partial Q}{\partial t}+\frac{\partial E}{\partial S}\frac{\partial S}{\partial t}$$

from which

$$\frac{\partial E}{\partial t}=\frac{\partial E}{\partial Q}\frac{\partial Q}{\partial t}\cong\frac{\partial E}{\partial Q}\frac{Q^{n+1}-Q^n}{\Delta t}=\frac{\partial E}{\partial Q}\frac{\Delta Q}{\Delta t} \tag{2.8}$$

Substitute (2.8) into equation (2.7) to obtain

$$E^{n+1}=E^n+\frac{\partial E}{\partial Q}\frac{\Delta Q}{\Delta t}\Delta t+O(\Delta t)^2$$

or

$$E^{n+1}=E^n+\frac{\partial E}{\partial Q}\Delta Q+O(\Delta t)^2 \tag{2.9}$$

In a similar fashion the following may be derived:

$$H^{n+1} = H^n + \frac{\partial H}{\partial Q}\Delta Q + O(\Delta t)^2 \tag{2.10}$$

The Jacobian matrix $\frac{\partial E}{\partial Q}$ will be denoted by A and is

$$A = \frac{\partial E}{\partial Q} = S \begin{bmatrix} 0 & 1 & 0 \\ \left(\frac{\gamma-3}{2}\right) u^2 & -(\gamma-3)u & (\gamma-1) \\ -\gamma u e_t + (\gamma-1)u^3 & \gamma e_t - \frac{3(\gamma-1)}{2}u^2 & \gamma u \end{bmatrix} \tag{2.11}$$

The Jacobian matrix $\frac{\partial H}{\partial Q}$ is denoted by B and is

$$B = \frac{\partial H}{\partial Q} = (\gamma-1)\frac{dS}{dx} \begin{bmatrix} 0 & 0 & 0 \\ \frac{1}{2}u^2 & -u & 1 \\ 0 & 0 & 0 \end{bmatrix} \tag{2.12}$$

The total energy e_t in the Jacobian matrix A is expressed in terms of the speed of sound. Thus,

$$e_t = \frac{a^2}{\gamma(\gamma-1)} + \frac{1}{2}u^2 \tag{2.13}$$

Equation (2.13) is used to rearrange the Jacobian matrix A as

$$A = S \begin{bmatrix} 0 & 1 & 0 \\ \left(\frac{\gamma-3}{2}\right) u^2 & -(\gamma-3)u & (\gamma-1) \\ -\frac{ua^2}{\gamma-1} + \left(\frac{1}{2}\gamma-1\right)u^3 & \frac{a^2}{\gamma-1} + \left(\frac{3}{2}-\gamma\right)u^2 & \gamma u \end{bmatrix} \tag{2.14}$$

Before a numerical scheme is proposed to solve the model equation (2.5), some of the properties of this PDE will be explored.

The first order hyperbolic equation (2.5) has the property that the flux vector E is a homogeneous function of degree one in Q; i.e., for any value of α, $E(\alpha Q) = \alpha E(Q)$. This property is referred to as the homogeneous property. In general, Euler equations possess this property. To be a hyperbolic system of equations, the Jacobian matrix A must possess real eigenvalues. The eigenvalues of A represent the characteristic directions of the hyperbolic system and thus provide the directions of the propagation of information. If a matrix has real eigenvalues and associated eigenvectors, it may be diagonalized, i.e., a similarity transformation exists such that

$$A = XDX^{-1}$$

where D is a diagonal matrix with its elements being the eigenvalues of A, and X is the eigenvector matrix.

To find the analytical forms of the eigenvalues of matrix A, program MACSYMA [39] is used and the resulting eigenvalues are

$$\lambda_1 = u \tag{2.15a}$$

$$\lambda_2 = u + a \tag{2.15b}$$

$$\lambda_3 = u - a \tag{2.15c}$$

and the associated eigenvectors are

$$X_1 = \begin{bmatrix} 1 \\ u \\ \frac{1}{2}u^2 \end{bmatrix}, \; X_2 = \begin{bmatrix} 1 \\ u + a \\ \frac{1}{2}u^2 + ua + \frac{a^2}{\gamma - 1} \end{bmatrix}, \; X_3 = \begin{bmatrix} 1 \\ u - a \\ \frac{1}{2}u^2 - ua + \frac{a^2}{\gamma - 1} \end{bmatrix}$$

Since the flux Jacobian matrix A possesses a complete set of eigenvalues and eigenvectors, a similarity transformation exists such that

$$A = XDX^{-1}$$

where

$$D = S \begin{bmatrix} u & 0 & 0 \\ 0 & u+a & 0 \\ 0 & 0 & u-a \end{bmatrix} \tag{2.16}$$

and

$$X = \begin{bmatrix} 1 & \alpha & \alpha \\ u & \alpha(u+a) & \alpha(u-a) \\ \frac{1}{2}u^2 & \alpha\left(\frac{1}{2}u^2 + ua + \frac{a^2}{\gamma-1}\right) & \alpha\left(\frac{1}{2}u^2 - ua + \frac{a^2}{\gamma-1}\right) \end{bmatrix} \tag{2.17}$$

where $\alpha = \frac{\rho}{\sqrt{2}a}$. The inverse of the eigenvector matrix X is

$$X^{-1} = \begin{bmatrix} 1 - \frac{u^2}{2}\frac{\gamma-1}{a^2} & (\gamma-1)\frac{u}{a^2} & -(\gamma-1)a^2 \\ \beta\left[(\gamma-1)\frac{u^2}{2} - ua\right] & \beta[a-(\gamma-1)u] & \beta(\gamma-1) \\ \beta\left[(\gamma-1)\frac{u^2}{2} + ua\right] & -\beta[a+(\gamma-1)u] & \beta(\gamma-1) \end{bmatrix} \tag{2.18}$$

where $\beta = \frac{1}{\rho a\sqrt{2}}$.

Note that the flux vector E equals AQ. Also, recall that the flux vector E possesses the homogeneous property; therefore, it may be split into

subvectors such that each subvector is associated with positive or negative eigenvalues of the flux matrix Jacobian. Thus, the eigenvalues may be grouped as positive or negative. For a subsonic flow, two of the eigenvalues, namely u and $u + a$, are positive, whereas the third eigenvalue, $u - a$, is negative. Therefore, the Jacobian matrix A is split according to

$$A = A^+ + A^-$$

where

$$A^+ = XD^+X^{-1}$$

and

$$A^- = XD^-X^{-1}$$

The elements of the diagonal matrices D^+ and D^- are the positive and negative eigenvalues, i.e.,

$$D = S\begin{bmatrix} u & 0 & 0 \\ 0 & u+a & 0 \\ 0 & 0 & u-a \end{bmatrix} = S\begin{bmatrix} u & 0 & 0 \\ 0 & u+a & 0 \\ 0 & 0 & 0 \end{bmatrix} + S\begin{bmatrix} 0 & 0 & 0 \\ 0 & 0 & 0 \\ 0 & 0 & u-a \end{bmatrix}$$

Now, the flux vector E may be split according to

$$E^+ = A^+Q \tag{2.19a}$$

and

$$E^- = A^-Q \tag{2.19b}$$

However, for a supersonic flow, all three eigenvalues are positive and, therefore,

$$A^+ = A$$

and

$$A^- = 0$$

The flux Jacobian matrices A^+ and A^- (for the subsonic flow) are also determined by MACSYMA. The result is

$$A^+ = S \begin{bmatrix} -\dfrac{(\gamma-1)u^3+a(3-\gamma)u^2-2a^2u}{4a^2} & \dfrac{(\gamma-1)u^2+a(2-\gamma)u+a^2}{2a^2} & -\dfrac{(\gamma-1)u-\gamma a+a}{2a^2} \\ -\dfrac{(\gamma-1)u^4+2a(2-\gamma)u^3+a^2(1-\gamma)u^2+2a^3u}{4a^2} & \dfrac{(\gamma-1)u^3+a(3-2\gamma)u^2+a^2(3-\gamma)u+a^3}{2a^2} & -\dfrac{(\gamma-1)u^2+2a(1-\gamma)u-\gamma a^2+a^2}{2a^2} \\ -\Big[(\gamma^2-2\gamma+1)u^5+(-3\gamma^2+8\gamma-5)au^4 & \Big[(\gamma^2-2\gamma+1)u^4+(-3\gamma^2+7\gamma-4)au^3 & -\dfrac{(\gamma-1)u^3+3a(1-\gamma)u^2-2\gamma a^2u-2a^3}{4a^2} \\ -2a^2(\gamma^2-2\gamma+1)u^3+2a^3(\gamma+1)u^2 & -a^2(2\gamma^2-5\gamma+3)u^2+2a^3(u+a)\Big] & \\ +4a^4u\Big] \,/\, \Big[8a^2(\gamma-1)\Big] & \,/\, \Big[4a^2(\gamma-1)\Big] & \end{bmatrix} \tag{2.20}$$

$$A^- = S \begin{bmatrix} \dfrac{(u-a)[(\gamma-1)u^2+2au]}{4a^2} & -\dfrac{(u-a)[(\gamma-1)u+a]}{2a^2} & \dfrac{(\gamma-1)(u-a)}{2a^2} \\ \dfrac{(u-a)^2[(\gamma-1)u^2+2au]}{4a^2} & -\dfrac{(u-a)^2[(\gamma-1)u+a]}{2a^2} & \dfrac{(\gamma-1)(u-a)^2}{2a^2} \\ \dfrac{(u-a)\left[\frac{1}{2}u^2-au+\frac{a^2}{\gamma-1}\right][(\gamma-1)u^2+2au]}{4a^2} & -\dfrac{(u-a)\left[\frac{1}{2}u^2-au+\frac{a^2}{\gamma-1}\right][(\gamma-1)u+a]}{2a^2} & \dfrac{(\gamma-1)(u-a)\left[\frac{1}{2}u^2-au+\frac{a^2}{\gamma-1}\right]}{2a^2} \end{bmatrix} \tag{2.21}$$

Therefore,

$$E^+ = S\frac{\rho}{2\gamma}\begin{bmatrix} 2\gamma u + a - u \\ 2(\gamma-1)u^2 + (u+a)^2 \\ (\gamma-1)u^3 + \frac{(u+a)^3}{2} + \frac{(3-\gamma)(u+a)a^2}{2(\gamma-1)} \end{bmatrix} \tag{2.22}$$

and

$$E^- = S\frac{\rho}{2\gamma}\begin{bmatrix} u - a \\ (u-a)^2 \\ \frac{(u-a)^3}{2} + \frac{(3-\gamma)(u-a)a^2}{2(\gamma-1)} \end{bmatrix} \tag{2.23}$$

Application [40] of the von Neumann stability analysis for equation (2.5) indicates that if one-sided differencing is used for the spatial derivatives, it must be a forward differencing for the terms associated with the negative eigenvalues and a backward differencing for the terms associated with the positive eigenvalues. This requirement is used to write the FDE.

Returning to equation (2.6), substitute the linearizations (2.9) and (2.10) to obtain

$$S\frac{\Delta Q}{\Delta t} + \frac{\partial}{\partial x}\left(E^n + \frac{\partial E}{\partial Q}\Delta Q\right) - \left(H^n + \frac{\partial H}{\partial Q}\Delta Q\right) = 0 \tag{2.24}$$

This equation may be expressed in terms of the Jacobian matrices A and B as

$$S\frac{\Delta Q}{\Delta t} + \frac{\partial}{\partial x}(A\Delta Q) - B\Delta Q = -\frac{\partial E^n}{\partial x} + H^n \tag{2.25}$$

and is factored as

$$\left[SI + \Delta t\left(\frac{\partial A}{\partial x}\right) - B\Delta t\right]\Delta Q = -\Delta t\left(\frac{\partial E^n}{\partial x} - H^n\right) \tag{2.26}$$

where I is the identity matrix and $\frac{\partial A}{\partial x}\Delta Q$ implies $\frac{\partial}{\partial x}(A\Delta Q)$. Now the flux vector E and the flux Jacobian matrix A are split according to the stability consideration to provide

$$\left[SI + \Delta t\left\{\frac{\partial}{\partial x}(A^+ + A^-) - B\right\}\right]\Delta Q = -\Delta t\left[\frac{\partial}{\partial x}(E^+ + E^-) - H^n\right]$$

A first-order backward difference approximation is used for the positive terms, and a first-order forward difference approximation is used for the negative terms. Hence,

$$\left[SI + \frac{\Delta t}{\Delta x}(A_i^+ - A_{i-1}^+ + A_{i+1}^- - A_i^-) - \Delta t\, B_i\right]\Delta Q =$$
$$-\Delta t\left[\frac{1}{\Delta x}(E_i^+ - E_{i-1}^+ + E_{i+1}^- - E_i^-) - H_i\right]$$

This equation is rearranged to give

$$-\left(\frac{\Delta t}{\Delta x}A_{i-1}^+\right)\Delta Q_{i-1} + \left[SI + \frac{\Delta t}{\Delta x}(A_i^+ - A_i^-) - \Delta t B_i\right]\Delta Q_i$$
$$+\left(\frac{\Delta t}{\Delta x}A_{i+1}^-\right)\Delta Q_{i+1} = -\frac{\Delta t}{\Delta x}(E_i^+ - E_{i-1}^+ + E_{i+1}^- - E_i^-) + \Delta t\, H_i \quad (2.27)$$

In order to write this equation in a manageable fashion, the following is defined:

$$\begin{aligned} AM &= -\frac{\Delta t}{\Delta x}A_{i-1}^+ \\ AA &= \left[SI + \frac{\Delta t}{\Delta x}(A_i^+ - A_i^-) - B_i\,\Delta t\right] \\ AP &= \frac{\Delta t}{\Delta x}A_{i+1}^- \\ RHS &= -\frac{\Delta t}{\Delta x}(E_i^+ - E_{i-1}^+ + E_{i+1}^- - E_i^-) + \Delta t\, H_i \end{aligned}$$

Thus, equation (2.27) is expressed as

$$AM_i\Delta Q_{i-1} + AA_i\Delta Q_i + AP_i\Delta Q_{i+1} = RHS_i \quad (2.28)$$

This equation is solved in a computational domain shown in Figure 2-1. Once equation (2.28) is applied to each grid point i, a block tridiagonal system is produced. The block tridiagonal system can be written in a matrix form as:

$$\begin{bmatrix} AA_2 & AP_2 & & & & \\ AM_3 & AA_3 & AP_3 & & & \\ & & & & & \\ & & AM_{IMM2} & AA_{IMM2} & AP_{IMM2} & \\ & & & AM_{IMM1} & AA_{IMM1} \end{bmatrix} \begin{bmatrix} \Delta Q_2 \\ \Delta Q_3 \\ | \\ \Delta Q_{IMM2} \\ \Delta Q_{IMM1} \end{bmatrix} = \begin{bmatrix} RHS_2 - AM_2 \Delta Q_1 \\ RHS_3 \\ | \\ RHS_{IMM2} \\ RHS_{IMM1} - AP_{IMM1} \Delta Q_{IM} \end{bmatrix} \tag{2.29}$$

Any standard block tridiagonal solver may be used to solve this system. Note that, for the supersonic region of the flow field, AP is zero (because A^- is zero) resulting in a lower diagonal banded matrix (bidiagonal system) which is inverted more efficiently than the tridiagonal system.

2.3 Boundary Conditions

For a given PDE, a set of boundary conditions must be specified. We shall refer to them as the "analytical boundary conditions". Once the PDE is approximated by a FDE, it may be higher order than the PDE. Thus the FDE will require additional boundary conditions. These boundary conditions will be referred to as "numerical boundary conditions" [41].

Now, consider the specification of the boundary conditions for the quasi one-dimensional problem. Recall that the eigenvalues of the flux Jacobian matrix A are u, $u+a$, and $u-a$. As mentioned previously, these eigenvalues indicate how information is fed into the domain. To illustrate this point, assume a supersonic inflow and a supersonic outflow. For a supersonic flow, all three eigenvalues are positive. At the inflow, three characteristics enter into the domain and, therefore, three analytical boundary conditions may be specified. At the outflow all the characteristics leave the domain and, as a result, no boundary condition can be specified.

The values of the dependent variables at the outflow must be evaluated based on the information reaching the outflow from the interior points. Note that these numerical boundary conditions cannot be specified arbitrarily and must be consistent with the direction of propagation of information determined by the sign of the eigenvalues of A. Usually, extrapolation schemes are used for this purpose. The extrapolation procedure may be either explicit or implicit. Some extrapolation schemes reported in the literature are (extrapolation for the value of a property f at $i = IM$ from interior points at $IMM1$ or $IMM1$ and $IMM2$):

$$f_{IM}^{n+1} = f_{IMM1}^{n+1} \tag{2.30a}$$

$$f_{IM}^{n+1} = 2f_{IMM1}^{n+1} - f_{IMM2}^{n+1} \tag{2.30b}$$

$$f_{IM}^{n+1} = f_{IMM1}^{n} \tag{2.30c}$$

$$f_{IM}^{n+1} = 2f_{IMM1}^{n} - f_{IMM2}^{n-1} \tag{2.30d}$$

$$f_{IM}^{n+1} = 2f_{IMM1}^{n} - f_{IMM2}^{n} \tag{2.30e}$$

If the outflow is subsonic, two of the eigenvalues are positive, i.e., outgoing, and one is negative, i.e., incoming from the outside. Therefore, one analytical boundary condition may be specified; and the other two are determined from the interior solution by extrapolation.

A summary for inflow and outflow boundary conditions for subsonic and supersonic conditions is given in Table 2-1 along with graphical illustrations.

It must be pointed out that, according to a linear stability analysis, the implicit formulation is stable. However, this does not guarantee the unconditional stability of the original nonlinear equations. In practice some stability limits are encountered. That is especially true for highly nonlinear problems, such as domains with shocks. However, the linear stability analysis is valuable in providing some guidelines for the stability requirements of the numerical schemes. In addition, the manner in which boundary conditions are specified will affect the stability of the numerical scheme. Therefore, stability analysis must be extended to include the boundary conditions. Some findings on the effect of boundary condition implementation are reported in Reference [42].

2.4 Two-Dimensional and Axisymmetric Euler Equations

The procedure for solution of the quasi one-dimensional Euler equations, along with some guidelines on stability, implementation of boundary conditions, and specification of the initial condition, was established in the preceding sections. In this section, two-dimensional and axisymmetric Euler

equations will be considered.

The governing equations of motion for the two-dimensional/axisymmetric inviscid flow in nondimensional form are:

$$\frac{\partial Q}{\partial t} + \frac{\partial E}{\partial x} + \frac{\partial F}{\partial y} + \alpha H = 0 \tag{2.31}$$

where

$$Q = \begin{bmatrix} \rho \\ \rho u \\ \rho v \\ \rho e_t \end{bmatrix} \quad (2.32), \quad E = \begin{bmatrix} \rho u \\ \rho u^2 + P \\ \rho uv \\ (\rho e_t + P)\, u \end{bmatrix} \quad (2.33), \quad F = \begin{bmatrix} \rho v \\ \rho vu \\ \rho v^2 + P \\ (\rho e_t + P)v \end{bmatrix} \quad (2.34)$$

$$H = \frac{1}{y} \begin{bmatrix} \rho v \\ \rho vu \\ \rho v^2 \\ (\rho e_t + P)v \end{bmatrix} \quad (2.35)$$

$$e_t = e + \frac{1}{2}(u^2 + v^2)$$

The following definitions were used to nondimensionalize the above equations:

$$u^* = \frac{u}{u_\infty} \quad , \quad v^* = \frac{v}{u_\infty} \quad , \quad T^* = \frac{T}{T_\infty} \, ,$$

$$e^* = \frac{e}{u_\infty^2} \quad , \quad e_t^* = \frac{e_t}{u_\infty^2} \quad , \quad \rho^* = \frac{\rho}{\rho_\infty} \, ,$$

$$p^* = \frac{p}{\rho_\infty u_\infty^2} \quad , \quad x^* = \frac{x}{L} \quad , \quad y^* = \frac{y}{L} \, ,$$

$$t^* = \frac{t}{L/U_\infty}$$

where the subscript ∞ indicates "free stream value" and L represents the characteristic length. Furthermore, the superscript "$*$" is deleted from the nondimensional quantities, and

$$\alpha = \begin{cases} 0 & \text{for a two-dimensional planar flow} \\ 1 & \text{for a two-dimensional axisymmetric flow} \end{cases}$$

The equations of motion were transformed from physical space to computational space as in Figure 2-2 [43]. With the generalized coordinate transformation, the Euler equations in the computational space become

$$\frac{\partial \bar{Q}}{\partial \tau} + \frac{\partial \bar{E}}{\partial \xi} + \frac{\partial \bar{F}}{\partial \eta} + \alpha \bar{H} = 0 \tag{2.36}$$

where

$$\bar{Q} = \frac{Q}{J} \tag{2.37}$$

$$\bar{E} = \frac{1}{J}[\xi_t Q + \xi_x E + \xi_y F] \tag{2.38}$$

$$\bar{F} = \frac{1}{J}[\eta_t Q + \eta_x E + \eta_y F] \tag{2.39}$$

$$\bar{H} = \frac{H}{J} \tag{2.40}$$

$$J = \xi_x \eta_y - \xi_y \eta_x = \frac{1}{x_\xi y_\eta - x_\eta y_\xi} \tag{2.41}$$

2.5 Finite Difference Formulation

The implicit finite difference formulation used in the preceding sections for the quasi one-dimensional Euler equations is extended to the two-dimensional/axisymmetric Euler equations. Since the details of the procedure were discussed previously, only a brief deliberation will follow.

The time derivative is approximated by a first-order backward difference quotient and the remaining terms are evaluated at time level $n+1$. Thus:

$$\frac{\bar{Q}^{n+1}-\bar{Q}^{n}}{\Delta\tau}+\left(\frac{\partial\bar{E}}{\partial\xi}\right)^{n+1}+\left(\frac{\partial\bar{F}}{\partial\eta}\right)^{n+1}+\alpha(\bar{H})^{n+1}=0 \tag{2.42}$$

Since, equation (2.42) is nonlinear, the following approximations are used to linearize the equation:

$$\bar{E}^{n+1} = \bar{E}^{n}+\left(\frac{\partial\bar{E}}{\partial\bar{Q}}\right)\Delta\bar{Q}+O(\Delta\tau)^{2} \tag{2.43}$$

$$\bar{F}^{n+1} = \bar{F}^{n}+\left(\frac{\partial\bar{F}}{\partial\bar{Q}}\right)\Delta\bar{Q}+O(\Delta\tau)^{2} \tag{2.44}$$

$$\bar{H}^{n+1} = \bar{H}^{n}+\left(\frac{\partial\bar{H}}{\partial\bar{Q}}\right)\Delta\bar{Q}+O(\Delta\tau)^{2} \tag{2.45}$$

where $\frac{\partial\bar{E}}{\partial\bar{Q}}$, $\frac{\partial\bar{F}}{\partial\bar{Q}}$ and $\frac{\partial\bar{H}}{\partial\bar{Q}}$ are the flux Jacobian matrices defined as $\frac{\partial\bar{E}}{\partial\bar{Q}}=A$, $\frac{\partial\bar{F}}{\partial\bar{Q}}=B$, and $\frac{\partial\bar{H}}{\partial\bar{Q}}=C$.

The Jacobian matrices A, B and C are

$$A = \frac{\partial \bar{E}}{\partial \bar{Q}} = \left[\begin{array}{c|c|c|c} \xi_t & \xi_x & \xi_y & 0 \\ \hline -u(u\xi_x + v\xi_y) & \xi_t + \xi_x(3-\gamma)u & -(\gamma-1)\xi_x v & (\gamma-1)\xi_x \\ +\xi_x\left[\frac{1}{2}(\gamma-1)(u^2+v^2)\right] & +\xi_y v & +\xi_y u & \\ \hline -v(u\xi_x + v\xi_y) & \xi_x v - (\gamma-1)\xi_y u & \xi_t + \xi_x u & (\gamma-1)\xi_y \\ +\xi_y\left[\frac{1}{2}(\gamma-1)(u^2+v^2)\right] & & +\xi_y(3-\gamma)v & \\ \hline (\xi_x u + \xi_y v)\cdot & \xi_x\left[\frac{a^2}{\gamma-1} + \frac{1}{2}(u^2+v^2)\right] & \xi_y\left[\frac{a^2}{\gamma-1} + \frac{1}{2}(u^2+v^2)\right] & \xi_t + \\ \left[-\frac{a^2}{\gamma-1} + (\frac{1}{2}\gamma-1)(u^2+v^2)\right] & -(\gamma-1)(\xi_x u + \xi_y v)u & -(\gamma-1)(\xi_x u + \xi_y v)v & \gamma(\xi_x u + \xi_y v) \end{array}\right] \tag{2.46}$$

$$B = \frac{\partial \bar{F}}{\partial \bar{Q}} = \left[\begin{array}{c|c|c|c} \eta_t & \eta_x & \eta_y & 0 \\ \hline -u(u\eta_x + v\eta_y) & \eta_t + \eta_x(3-\gamma)u & -(\gamma-1)\eta_x v & (\gamma-1)\eta_x \\ +\eta_x\left[\frac{1}{2}(\gamma-1)(u^2+v^2)\right] & +\eta_y v & +\eta_y u & \\ \hline -v(\eta_x u + \eta_y v) & \eta_x v - (\gamma-1)\eta_y u & \eta_t + \eta_x u & (\gamma-1)\eta_y \\ +\eta_y\left[\frac{1}{2}(\gamma-1)(u^2+v^2)\right] & & +\eta_y(3-\gamma)v & \\ \hline (u\eta_x + v\eta_y)\cdot & \eta_x\left[\frac{a^2}{\gamma-1} + \frac{1}{2}(u^2+v^2)\right] & \eta_y\left[\frac{a^2}{\gamma-1} + \frac{1}{2}(u^2+v^2)\right] & \eta_t + \\ \left[-\frac{a^2}{\gamma-1} + (\frac{\gamma}{2}-1)(u^2+v^2)\right] & -(\gamma-1)(\eta_x u + \eta_y v)u & -(\gamma-1)(\eta_x u + \eta_y v)v & \gamma(\eta_x u + \eta_y v) \end{array}\right] \tag{2.47}$$

$$C = \frac{\partial \bar{H}}{\partial \bar{Q}} = \frac{1}{y} \begin{bmatrix} 0 & 0 & 1 & 0 \\ -uv & v & u & 0 \\ -v^2 & 0 & 2v & 0 \\ v[-\gamma e_t + (\gamma - 1)(u^2 + v^2)] & -(\gamma - 1)uv & \gamma e_t - \left(\frac{\gamma - 1}{2}\right)(3v^2 + u^2) & \gamma v \end{bmatrix} \tag{2.48}$$

Relations (2.43) through (2.45) are substituted into equation (2.42) and rearranged as

$$\Delta\bar{Q} + \Delta\tau \left\{ \frac{\partial}{\partial\xi}[\bar{E}^n + A^n\Delta\bar{Q}] + \frac{\partial}{\partial\eta}[\bar{F}^n + B^n\Delta\bar{Q}^n] \right.$$
$$\left. + \alpha[\bar{H}^n + C^n\Delta\bar{Q}] \right\} = 0$$

or

$$\left\{ I + \Delta\tau \left[\frac{\partial}{\partial\xi}(A^n) + \frac{\partial}{\partial\eta}(B^n) + \alpha C^n \right] \right\} \Delta\bar{Q} =$$
$$-\Delta\tau \left\{ \frac{\partial\bar{E}^n}{\partial\xi} + \frac{\partial\bar{F}^n}{\partial\eta} + \alpha\bar{H}^n \right\} \tag{2.49}$$

The approximate factorization approach is used in equation (2.49) in order to reduce the pentadiagonal coefficient matrix into two tridiagonal systems.

The approximate factorization of equation (2.49) is

$$\left[I + \Delta\tau\frac{\partial A^n}{\partial\xi} \right] \left[I + \Delta\tau\frac{\partial B^n}{\partial\eta} + \alpha\Delta\tau C^n \right] \Delta\bar{Q} =$$
$$-\Delta\tau \left\{ \frac{\partial\bar{E}^n}{\partial\xi} + \frac{\partial\bar{F}^n}{\partial\eta} + \alpha\bar{H}^n \right\} \tag{2.50}$$

Note that the terms on the right-hand side of this equation are evaluated at the known time level n. The unknown is the vector $\Delta\bar{Q}$.

A flux vector splitting scheme similar to that employed previously is used in equation (2.50). The eigenvalues of matrix A, determined by MACSYMA are as follows:

$$\lambda_{\xi_1} = \xi_t + \xi_x u + \xi_y v \tag{2.51}$$

$$\lambda_{\xi_2} = \xi_t + \xi_x u + \xi_y v \tag{2.52}$$

$$\lambda_{\xi_3} = \xi_t + \xi_x u + \xi_y v + a\sqrt{\xi_x^2 + \xi_y^2} \tag{2.53}$$

$$\lambda_{\xi_4} = \xi_t + \xi_x u + \xi_y v - a\sqrt{\xi_x^2 + \xi_y^2} \tag{2.54}$$

The eigenvector matrix as determined by MACSYMA is

$$X_A = \begin{bmatrix} 0 & 1 & 1 & 1 \\ -\frac{\xi_y}{\xi_x} & \frac{u\xi_x + v\xi_y}{\xi_x} & u + \frac{a\xi_x}{\sqrt{\xi_x^2 + \xi_y^2}} & u - \frac{a\xi_x}{\sqrt{\xi_x^2 + \xi_y^2}} \\ 1 & 0 & v + \frac{a\xi_y}{\sqrt{\xi_x^2 + \xi_y^2}} & v - \frac{a\xi_y}{\sqrt{\xi_x^2 + \xi_y^2}} \\ \frac{v\xi_x - u\xi_y}{\xi_x} & \frac{2uv\xi_y + (u^2 - v^2)\xi_x}{2\xi_x} & \frac{u^2 + v^2}{2} + \frac{a^2}{\gamma - 1} + \frac{a(u\xi_x + v\xi_y)}{\sqrt{\xi_x^2 + \xi_y^2}} & \frac{u^2 + v^2}{2} + \frac{a^2}{\gamma - 1} - \frac{a(u\xi_x + v\xi_y)}{\sqrt{\xi_x^2 + \xi_y^2}} \end{bmatrix}$$

and the inverse of the eigenvector matrix X_A is

$$X_A^{-1} = \begin{bmatrix} \frac{(1-\gamma)v(u^2+v^2)}{2a^2} + & \frac{(\gamma-1)uv}{a^2} + & \frac{(\gamma-1)v^2}{a^2} + & -\frac{(\gamma-1)v}{a^2} \\ + \frac{\xi_y(u\xi_x+v\xi_y)}{\xi_x^2+\xi_y^2} & - \frac{\xi_x\xi_y}{\xi_x^2+\xi_y^2} & + \frac{\xi_x^2}{\xi_x^2+\xi_y^2} & \\ 1 + \frac{(1-\gamma)(u^2+v^2)}{2a^2} & \frac{(\gamma-1)u}{a^2} & \frac{(\gamma-1)v}{a^2} & -\frac{\gamma-1}{a^2} \\ \frac{(\gamma-1)(u^2+v^2)}{4a^2} + & \frac{(1-\gamma)u}{2a^2} + \frac{\xi_x}{2a\sqrt{\xi_x^2+\xi_y^2}} & \frac{(1-\gamma)v}{2a^2} + \frac{\xi_y}{2a\sqrt{\xi_x^2+\xi_y^2}} & \frac{\gamma-1}{2a^2} \\ - \frac{u\xi_x+v\xi_y}{2a\sqrt{\xi_x^2+\xi_y^2}} & & & \\ \frac{(\gamma-1)(u^2+v^2)}{4a^2} + & \frac{(1-\gamma)u}{2a^2} + & \frac{(1-\gamma)v}{2a^2} - \frac{\xi_y}{2a\sqrt{\xi_x^2+\xi_y^2}} & \frac{\gamma-1}{2a^2} \\ + \frac{u\xi_x+v\xi_y}{2a\sqrt{\xi_x^2+\xi_y^2}} & - \frac{\xi_x}{2a\sqrt{\xi_x^2+\xi_y^2}} & & \end{bmatrix}$$

Similarly, the eigenvalues of B are determined as

$$\lambda_{\eta_1} = \eta_t + \eta_x u + \eta_y v \tag{2.55}$$

$$\lambda_{\eta_2} = \eta_t + \eta_x u + \eta_y v \tag{2.56}$$

$$\lambda_{\eta_3} = \eta_t + \eta_x u + \eta_y v + a\sqrt{\eta_x^2+\eta_y^2} \tag{2.57}$$

$$\lambda_{\eta_4} = \eta_t + \eta_x u + \eta_y v - a\sqrt{\eta_x^2+\eta_y^2} \tag{2.58}$$

with the associated eigenvector matrix X_B of

$$X_B = \begin{bmatrix} 0 & 1 & 1 & 1 \\ -\frac{\eta_y}{\eta_x} & \frac{u\eta_x + v\eta_y}{\eta_x} & u + \frac{a\eta_x}{\sqrt{\eta_x^2 + \eta_y^2}} & u - \frac{a\eta_x}{\sqrt{\eta_x^2 + \eta_y^2}} \\ 1 & 0 & v + \frac{a\eta_y}{\sqrt{\eta_x^2 + \eta_y^2}} & v - \frac{a\eta_y}{\sqrt{\eta_x^2 + \eta_y^2}} \\ \frac{v\eta_x - u\eta_y}{\eta_x} & \frac{2uv\eta_y + (u^2 - v^2)\eta_x}{2\eta_x} & \frac{u^2 + v^2}{2} + \frac{a^2}{\gamma - 1} + \frac{a(u\eta_x + v\eta_y)}{\sqrt{\eta_x^2 + \eta_y^2}} & \frac{u^2 + v^2}{2} + \frac{a^2}{\gamma - 1} + \frac{a(u\eta_x + v\eta_y)}{\sqrt{\eta_x^2 + \eta_y^2}} \end{bmatrix}$$

and the inverse

$$X_B^{-1} = \left[\begin{array}{c|c|c|c} \frac{(1-\gamma)v(u^2+v^2)}{2a^2} + & \frac{(\gamma-1)uv}{a^2} + & \frac{(\gamma-1)v^2}{a^2} + & -\frac{(\gamma-1)v}{a^2} \\ + \frac{\eta_y(u\eta_x + v\eta_y)}{\eta_x^2+\eta_y^2} & - \frac{\eta_x\eta_y}{\eta_x^2+\eta_y^2} & + \frac{\eta_x^2}{\eta_x^2+\eta_y^2} & \\ \hline 1 + \frac{(1-\gamma)(u^2+v^2)}{2a^2} & \frac{(\gamma-1)u}{a^2} & \frac{(\gamma-1)v}{a^2} & -\frac{\gamma-1}{a^2} \\ \hline \frac{(\gamma-1)(u^2+v^2)}{4a^2} + & \frac{(1-\gamma)u}{2a^2} + \frac{\eta_x}{2a\sqrt{\eta_x^2+\eta_y^2}} & \frac{(1-\gamma)v}{2a^2} + \frac{\eta_y}{2a\sqrt{\eta_x^2+\eta_y^2}} & \frac{\gamma-1}{2a^2} \\ - \frac{u\eta_x + v\eta_y}{2a\sqrt{\eta_x^2+\eta_y^2}} & & & \\ \hline \frac{(\gamma-1)(u^2+v^2)}{4a^2} + & \frac{(1-\gamma)u}{2a^2} + & \frac{(1-\gamma)v}{2a^2} - \frac{\eta_y}{2a\sqrt{\eta_x^2+\eta_y^2}} & \frac{\gamma-1}{2a^2} \\ + \frac{u\eta_x + v\eta_y}{2a\sqrt{\eta_x^2+\eta_y^2}} & - \frac{\eta_x}{2a\sqrt{\eta_x^2+\eta_y^2}} & & \end{array}\right]$$

For grid systems where ξ_x becomes zero, the following Jacobian matrix A is used.

$$A = \begin{bmatrix} 0 & 0 & \xi_y & 0 \\ -\xi_y uv & \xi_y v & \xi_y u & 0 \\ \xi_y\left[\frac{(\gamma-1)u^2+(\gamma-3)v^2}{2}\right] & \xi_y u(1-\gamma) & \xi_y(3-\gamma)v & \xi_y(\gamma-1) \\ \xi_y v\left[-\frac{a^2}{\gamma-1} + \left(\frac{\gamma-2}{2}\right)(u^2+v^2)\right] & \xi_y(1-\gamma)uv & \xi_y\left[\frac{a^2}{\gamma-1} + \frac{u^2}{2} + \left(\frac{3}{2}-\gamma\right)v^2\right] & \gamma\xi_y v \end{bmatrix}$$

where the eigenvalues of A are

$$\lambda_{\xi_1} = \xi_y v \tag{2.59}$$

$$\lambda_{\xi_2} = \xi_y v \tag{2.60}$$

$$\lambda_{\xi_3} = (v+a)\xi_y \tag{2.61}$$

$$\lambda_{\xi_4} = (v-a)\xi_y \tag{2.62}$$

The eigenvector matrix is

$$X_A = \begin{bmatrix} 0 & 1 & 1 & 1 \\ 1 & 0 & u & u \\ 0 & v & v+a & v-a \\ u & \frac{v^2-u^2}{2} & \frac{a^2}{\gamma-1}+\frac{(u^2+v^2+2av)}{2} & \frac{a^2}{\gamma-1}+\frac{(u^2+v^2-2av)}{2} \end{bmatrix}$$

and the inverse of the eigenvector matrix X_A is

$$X_A^{-1} = \begin{bmatrix} -\frac{(\gamma-1)(u^3+uv^2)}{2a^2} & 1+\frac{(\gamma-1)u^2}{a^2} & \frac{(\gamma-1)uv}{a^2} & \frac{-(\gamma-1)u}{a^2} \\ 1-\frac{(\gamma-1)(u^2+v^2)}{2a^2} & \frac{(\gamma-1)u}{a^2} & \frac{(\gamma-1)v}{a^2} & \frac{-(\gamma-1)}{a^2} \\ \frac{(\gamma-1)(u^2+v^2)-2av}{4a^2} & \frac{-(\gamma-1)u}{2a^2} & \frac{a-(\gamma-1)v}{2a^2} & \frac{(\gamma-1)}{2a^2} \\ \frac{(\gamma-1)(u^2+v^2)+2av}{4a^2} & \frac{-(\gamma-1)u}{2a^2} & -\frac{[a+(\gamma-1)v]}{2a^2} & \frac{(\gamma-1)}{2a^2} \end{bmatrix}$$

Notice that if $\eta_x = 0$, then $B = \Big[$same as A, but replace ξ_y by $\eta_y\Big]$. The eigenvalues of B are

$$\lambda_{\eta_1} = \eta_y v \tag{2.63}$$

$$\lambda_{\eta_2} = \eta_y v \tag{2.64}$$

$$\lambda_{\eta_3} = (v+a)\eta_y \tag{2.65}$$

$$\lambda_{\eta_4} = (v-a)\eta_y \tag{2.66}$$

and

$$X_B = X_A$$
$$X_B^{-1} = X_A^{-1}$$

Once the eigenvalues of flux Jacobian matrices A and B are determined, they may be split according to

$$A = A^+ + A^-$$

and

$$B = B^+ + B^-$$

where

$$A^+ = X_A D_A^+ X_A^{-1} \tag{2.67}$$
$$A^- = X_A D_A^- X_A^{-1} \tag{2.68}$$
$$B^+ = X_B D_B^+ X_B^{-1} \tag{2.69}$$

and

$$B^- = X_B D_B^- X_B^{-1} \tag{2.70}$$

As before, matrix D_A^+ is a diagonal matrix whose elements are the positive eigenvalues of A; and D_A^- is a diagonal matrix whose elements are the negative eigenvalues of A. The same analogy is extended to D_B^+ and D_B^-.

Returning back to the flux vector splitting, $\bar{E}$ and $\bar{F}$ vectors are split according to

$$\bar{E} = \bar{E}^+ + \bar{E}^-$$

and

$$\bar{F} = \bar{F}^+ + \bar{F}^-$$

where

$$\bar{E}^+ = A^+\bar{Q}$$

$$\bar{E}^- = A^-\bar{Q}$$

$$\bar{F}^+ = B^+\bar{Q}$$

and

$$\bar{F}^- = B^-\bar{Q}$$

Now, consider the FDE (2.50) where flux vector splitting is used. Hence,

$$\left\{I + \Delta\tau\left[\frac{\partial}{\partial\xi}(A^+ + A^-)\right]\right\}\left\{I + \Delta\tau\left[\frac{\partial}{\partial\eta}(B^+ + B^-)\right] + \alpha\Delta\tau C\right\}\Delta\bar{Q} =$$
$$-\Delta\tau\left\{\frac{\partial}{\partial\xi}(\bar{E}^+ + \bar{E}^-) + \frac{\partial}{\partial\eta}(\bar{F}^+ + \bar{F}^-) + \alpha\bar{H}\right\}$$

As discussed previously, a first-order backward difference approximation is used for the positive terms, and a first-order forward difference approximation is used for the negative terms. Therefore,

$$\left[I + \frac{\Delta\tau}{\Delta\xi}(A^+_{i,j} - A^+_{i-1,j} + A^-_{i+1,j} - A^-_{i,j})\right]\left[I + \frac{\Delta\tau}{\Delta\eta}(B^+_{i,j} - B^+_{i,j-1} + B^-_{i,j+1}\right.$$
$$\left. - B^-_{i,j}) + \alpha\Delta\tau C_{i,j}\right]\Delta\bar{Q} = -\Delta\tau\left[\frac{1}{\Delta\xi}(\bar{E}^+_{i,j} - \bar{E}^+_{i-1,j} + \bar{E}^-_{i+1,j} - \bar{E}^-_{i,j})\right.$$
$$\left. + \frac{1}{\Delta\eta}(\bar{F}^+_{i,j} - \bar{F}^+_{i,j-1} + \bar{F}^-_{i,j+1} - \bar{F}^-_{i,j}) + \alpha\bar{H}_{i,j}\right] \tag{2.71}$$

Equation (2.70) is solved in two stages as

$$\left[I + \frac{\Delta\tau}{\Delta\eta}(B^+_{i,j} - B^+_{i,j-1} + B^-_{i,j+1} - B^-_{i,j}) + \alpha\Delta\tau C_{i,j}\right]\Delta\bar{Q}^* =$$

$$-\Delta\tau\left[\frac{1}{\Delta\xi}(\bar{E}^{+}_{i,j}-\bar{E}^{+}_{i-1,j}+\bar{E}^{-}_{i+1,j}-\bar{E}^{-}_{i,j})\right.$$
$$\left.+\frac{1}{\Delta\eta}(\bar{F}^{+}_{i,j}-\bar{F}^{+}_{i,j-1}+\bar{F}^{-}_{i,j+1}-\bar{F}^{-}_{i,j})+\alpha\bar{H}_{i,j}\right]$$

and

$$\left[I+\frac{\Delta\tau}{\Delta\xi}(A^{+}_{i,j}-A^{+}_{i-1,j}+A^{-}_{i+1,j}-A^{-}_{i,j})\right]\Delta\bar{Q}=\Delta\bar{Q}^{*} \tag{2.72}$$

where each equation is a block tridiagonal form. These equations are rearranged as

$$\left(-\frac{\Delta\tau}{\Delta\eta}B^{+}_{i,j-1}\right)\Delta\bar{Q}^{*}_{i,j-1}+\left[I+\frac{\Delta\tau}{\Delta\eta}(B^{+}_{i,j}-B^{-}_{i,j})+\alpha\Delta\tau C_{i,j}\right]\Delta\bar{Q}^{*}_{i,j}$$
$$+\left(\frac{\Delta\tau}{\Delta\eta}B^{-}_{i,j+1}\right)\Delta\bar{Q}^{*}_{i,j+1}=(RHS)_{i,j} \tag{2.73}$$

and

$$\left(-\frac{\Delta\tau}{\Delta\xi}A^{+}_{i-1,j}\right)\Delta\bar{Q}_{i-1,j}+\left[I+\frac{\Delta\tau}{\Delta\xi}(A^{+}_{i,j}-A^{-}_{i,j})\right]\Delta\bar{Q}_{i,j}$$
$$+\left(\frac{\Delta\tau}{\Delta\xi}A^{-}_{i+1,j}\right)\Delta\bar{Q}_{i+1,j}=\Delta\bar{Q}^{*}_{i,j} \tag{2.74}$$

The terms in equations (2.73) and (2.74) are redefined as

$$\begin{aligned}
CBM &= -\frac{\Delta\tau}{\Delta\eta}B^{+}_{i,j-1}\\
CB &= \left[I+\frac{\Delta\tau}{\Delta\eta}(B^{+}_{i,j}-B^{-}_{i,j})+\alpha\Delta\tau C_{i,j}\right]\\
CBP &= \frac{\Delta\tau}{\Delta\eta}B^{-}_{i,j+1}\\
CAM &= -\frac{\Delta\tau}{\Delta\xi}A^{+}_{i-1,j}\\
CA &= \left[I+\frac{\Delta\tau}{\Delta\xi}(A^{+}_{i,j}-A^{-}_{i,j})\right]\\
CAP &= \frac{\Delta\tau}{\Delta\xi}A^{-}_{i+1,j}
\end{aligned}$$

Therefore, equations (2.72) and (2.73) become

$$CBM_{i,j}\Delta\bar{Q}^*_{i,j-1} + CB_{i,j}\Delta\bar{Q}^*_{i,j} + CBP_{i,j}\Delta\bar{Q}^*_{i,j+1} = (RHS)_{i,j} \tag{2.75}$$

and

$$CAM_{i,j}\Delta\bar{Q}_{i-1,j} + CA_{i,j}\Delta\bar{Q}_{i,j} + CAP_{i,j}\Delta\bar{Q}_{i+1,j} = \Delta\bar{Q}^*_{i,j} \tag{2.76}$$

If a grid line is aligned along the stagnation streamline, which for the axisymmetric configuration at zero degree angle of attack is coincident with the body axis, some difficulty in convergence is observed. Therefore, the first constant ξ grid line ($i = 1$) is set below the body axis, and the second constant ξ line ($i = 2$) is set by symmetry as illustrated in Figure 2-2. The steps in the ξ and η sweeps in the computational domain are shown in Figure 2-3.

2.6 Boundary Conditions

When equation (2.75) is written at each ξ for all j from $j = 2$ to $j = JMM1$, a block tridiagonal system is obtained. This system is expressed as

$$\begin{bmatrix} [CB]_{i,2} & [CBP]_{i,2} & & & \\ [CBM]_{i,3} & [CB]_{i,3} & [CBP]_{i,3} & & \\ & & & & \\ & [CBM]_{i,JMM2} & [CB]_{i,JMM2} & [CBP]_{i,JMM2} & \\ & & [CBM]_{i,JMM1} & [CB]_{i,JMM1} & \end{bmatrix} \begin{bmatrix} \Delta\bar{Q}^*_{i,2} \\ \Delta\bar{Q}^*_{i,3} \\ | \\ \Delta\bar{Q}^*_{i,JMM2} \\ \Delta\bar{Q}^*_{i,JMM1} \end{bmatrix} =$$

$$\begin{bmatrix} (RHS)_{i,2} - [CBM]_{i,2}\Delta\bar{Q}^*_{i,1} \\ (RHS)_{i,3} \\ \vdots \\ (RHS)_{i,JMM2} \\ (RHS)_{i,JMM1} - [CBP]_{i,JMM1}\Delta\bar{Q}^*_{i,JM} \end{bmatrix} \tag{2.77}$$

If the outer boundary of the domain (i.e., $j = JM$) is set at the free stream, $\Delta\bar{Q}^*_{i,JM}$ is zero. Note that for this statement to be valid, the spatial grid is assumed to be independent of time, i.e., grid points do not move; as a result, $J^n_{i,j} = J^{n+1}_{i,j}$. But what about $\Delta\bar{Q}^*_{i,1}$? For the time being, its value will be set to zero. Later, this value will be computed and updated. By setting $\Delta\bar{Q}^*_{i,1}$ equal to zero, the system (2.77) may be solved for all the $\Delta\bar{Q}^*_{i,j}$ from $j = 2$ to $JMM1$ for each ξ from $i = 2$ to $i = IMM1$, i.e., the ξ sweep. Once $\Delta\bar{Q}^*_{i,j}$ is computed, the RHS of equation (2.76) is known. When this equation is applied for all i from $i = 2$ to $i = IMM1$, one obtains the following block tridiagonal system:

$$\begin{bmatrix} [CA]_{2,j} & [CAP]_{2,j} & & \\ [CAM]_{3,j} & [CA]_{3,j} & [CAP]_{3,j} & \\ & & & \\ & [CAM]_{IMM2,j} & [CA]_{IMM2,j} & [CAP]_{IMM2,j} \\ & & [CAM]_{IMM1,j} & [CA]_{IMM1,j} \end{bmatrix} \begin{bmatrix} \Delta\bar{Q}_{2,j} \\ \Delta\bar{Q}_{3,j} \\ \vdots \\ \Delta\bar{Q}_{IMM2,j} \\ \Delta\bar{Q}_{IMM1,j} \end{bmatrix} =$$

$$\begin{bmatrix} \Delta\bar{Q}^*_{2,j} - [CAM]_{2,j}\Delta\bar{Q}_{1,j} \\ \Delta\bar{Q}^*_{3,j} \\ \vdots \\ \Delta\bar{Q}^*_{IMM2,j} \\ \Delta\bar{Q}^*_{IMM1,j} - [CAP]_{IMM1,j}\Delta\bar{Q}_{IM,j} \end{bmatrix} \tag{2.78}$$

At $i = 1$, symmetry is imposed. Note that, due to the symmetry of grid lines $i = 1$ and $i = 2$, the Jacobians of transformation are equal, i.e., $J_{1,j} = J_{2,j}$ for all (j)s. From the physical point of view, the following constraints hold for both the flow and thermodynamics properties.

$$\begin{aligned} \rho_{1,j} &= \rho_{2,j} \\ u_{1,j} &= u_{2,j} \\ v_{1,j} &= -v_{2,j} \\ e_{t1,j} &= e_{t2,j} \end{aligned}$$

Therefore,

$$\Delta\bar{Q}_{1,j} = \frac{1}{J_{1,j}} \begin{bmatrix} (\Delta\rho)_{1,j} \\ (\Delta\rho u)_{1,j} \\ (\Delta\rho v)_{1,j} \\ (\Delta\rho e_t)_{1,j} \end{bmatrix} = \frac{1}{J_{2,j}} \begin{bmatrix} (\Delta\rho)_{2,j} \\ (\Delta\rho u)_{2,j} \\ -(\Delta\rho v)_{2,j} \\ (\Delta\rho e_t)_{2,j} \end{bmatrix}$$

Hence, the first equation represented as the first row of the block tridiagonal system (2.78) is modified according to

$$\left[\overline{CA}\right]_{2,j} \Delta\bar{Q}_{2,j} + [CAP]_{2,j} \Delta\bar{Q}_{3,j} = \Delta\bar{Q}^*_{2,j}$$

where

$$\left[\overline{CA}\right]_{2,j} = [CA]_{2,j} + [CAM]_{2,j} \cdot \begin{bmatrix} 1 & 0 & 0 & 0 \\ 0 & 1 & 0 & 0 \\ 0 & 0 & -1 & 0 \\ 0 & 0 & 0 & 1 \end{bmatrix}$$

Assuming $i = IM$ is for downstream, such that the flow is supersonic, extrapolation is used. For simplicity, the following zero-order extrapolation is

employed.

$$\Delta\bar{Q}_{IM,j} = \Delta\bar{Q}_{IMM1,j}$$

With this simple extrapolation, the last equation of the block tridiagonal system (2.78) is modified according to

$$[CAM]_{IMM1,j}\,\Delta\bar{Q}_{IMM2,j} + \left[\overline{CA}\right]_{IMM1,j}\Delta\bar{Q}_{IMM1,j} = \Delta\bar{Q}^{*}_{IMM1,j}$$

where

$$\left[\overline{CA}\right]_{IMM1,j} = [CA]_{IMM1,j} + [CAP]_{IMM1,j}$$

Finally, the block tridiagonal system is expressed as

$$\begin{bmatrix} [\overline{CA}]_{2,j} & [CAP]_{2,j} & & \\ [CAM]_{3,j} & [CA]_{3,j} & [CAP]_{3,j} & \\ & \ddots & \ddots & \ddots \\ & [CAM]_{IMM2,j} & [CA]_{IMM2,j} & [CAP]_{IMM2,j} \\ & & [CAM]_{IMM1,j} & \left[\overline{CA}\right]_{IMM1,j} \end{bmatrix} \begin{bmatrix} \Delta\bar{Q}_{2,j} \\ \Delta\bar{Q}_{3,j} \\ \vdots \\ \Delta\bar{Q}_{IMM2,j} \\ \Delta\bar{Q}_{IMM1,j} \end{bmatrix} = \begin{bmatrix} \Delta\bar{Q}^{*}_{2,j} \\ \Delta\bar{Q}^{*}_{3,j} \\ \vdots \\ \Delta\bar{Q}^{*}_{IMM2,j} \\ \Delta\bar{Q}^{*}_{IMM1,j} \end{bmatrix} \tag{2.79}$$

Now it is possible to sweep in the η direction. The system (2.79) is solved for all $\Delta\bar{Q}$s from $i = 2$ to $i = IMM1$ for each η from $j = 2$ to $j = JMM1$.

2.7 Properties at the Body Surface

For an inviscid flow over nonporous surfaces, the velocity slip condition may be applied. A unit vector normal to the surface can be determined according to

$$\hat{n} = \frac{\nabla\eta}{|\nabla\eta|}$$

where

$$\nabla\eta = \eta_x\hat{\imath} + \eta_y\hat{\jmath} = J(-y_\xi\hat{\imath} + x_\xi\hat{\jmath})$$

The velocity vector for a 2-D flow in Cartesian coordinate is expressed as

$$\vec{V} = u\hat{\imath} + v\hat{\jmath}$$

For mutually perpendicular vectors

$$\vec{V}\cdot\hat{n} = 0$$

Thus

$$u\eta_x + v\eta_y = 0$$

which results in

$$\frac{u}{v} = -\frac{\eta_y}{\eta_x} \tag{2.80}$$

A relationship between pressure and other flow properties is derived in Appendix A, with the following result:

$$\begin{aligned}&\eta_x\left(\frac{\rho uU}{J}\right)_\xi + \eta_y\left(\frac{\rho vU}{J}\right)_\xi + \eta_x\left(\frac{\rho uV}{J}\right)_\eta + \eta_y\left(\frac{\rho vV}{J}\right)_\eta \\ &+ \eta_x\left(\frac{\xi_x P}{J}\right)_\xi + \eta_x\left(\frac{\eta_x P}{J}\right)_\eta + \eta_y\left(\frac{\xi_y P}{J}\right)_\xi + \eta_y\left(\frac{\eta_y P}{J}\right)_\eta = 0\end{aligned} \tag{2.81}$$

where U and V are the contravariant velocities, defined as $U = u\xi_x + v\xi_y$, $V = u\eta_x + v\eta_y$.

The stagnation enthalpy is assumed constant along the body surface and equal to that of the free stream, i.e.,

$$h_t = h + \frac{1}{2}(u^2 + v^2)$$

The reasoning for this assumption is as follows. Recall that the energy equation may be expressed as

$$\rho \frac{Dh_t}{Dt} = \frac{\partial P}{\partial t}$$

For a time marching procedure, the value of pressure will obviously change. However, as one approaches steady-state, this change approaches zero. Therefore, this condition is forced on the solution. The nondimensional stagnation enthalpy is expressed as

$$h_t = \frac{E_t + P}{\rho} = \frac{1}{\rho}\left\{\left[e + \frac{1}{2}(u^2 + v^2)\right]\rho + (\gamma - 1)\rho e\right\}$$

(Note that as discussed previously the notation *, representing the nondimensional quantities, is dropped) or

$$h_t = \frac{1}{2}(u^2 + v^2) + \gamma e$$

Since $u = 1$ and $v = 0$ for the free stream, therefore

$$(h_t)_\infty = \gamma e_\infty + \frac{1}{2} = (h_t)_{\text{wall}} \tag{2.82}$$

The unknowns at the surface include u, v, ρ, and P or e. Up to this point, three equations have been discussed which are applicable at the surface. They are equations (2.80), (2.81), and (2.82). As a fourth relation, an iteration scheme will be proposed.

In order to write various expressions which will be used later in a compact form, the following expressions are defined:

$$\begin{aligned} A_i &= \sqrt{(\rho u)_{i,2}^2 + (\rho v)_{i,2}^2} \\ B_i &= \sqrt{(\eta_x^2 + \eta_y^2)_{i,1}} \\ C_i &= \frac{A_i \eta_{y_{i,1}}}{B_i} \\ D_i &= -\frac{A_i \eta_{x_{i,1}}}{B_i} \end{aligned}$$

Now, the iteration scheme proceeds as follows:

(1) Assume $\rho_{i,1}^k = \rho_{i,2}$ for all (i)s.

(2) Compute A_i, B_i, C_i, and D_i.

(3) Compute

$$u_{i,1} = \frac{C_i}{\rho_{i,1}^k}$$

$$v_{i,1} = \frac{D_i}{\rho_{i,1}^k}$$

for all (i)s. The expressions above for $u_{i,1}$ and $v_{i,1}$ are described in Appendix B.

(4) Now equation (2.81) is used to evaluate the pressure at the surface. Note that at the boundaries $i = 1$ and $i = IM$, the following are enforced:

$$\begin{aligned} P_{1,1} &= P_{2,1} \quad \text{due to symmetry} \\ P_{IM,1} &= P_{IMM1,1} \frac{J_{IM,1}}{J_{IMM1,1}} \quad \text{zero-order extrapolation.} \end{aligned}$$

To numerically solve equation (2.81), an FDE is obtained by using a second-order central difference approximation in the ξ direction and a

second-order one-sided approximation in the η direction. The FDE is provided in Appendix A.

(5) Now the energy equation is used to compute the density at the wall. This equation may be expressed as

$$\rho_{i,1}^{k+1} = \frac{1}{2(h_t)_{\text{wall}}(\gamma-1)}\left\{\gamma P_{i,1} + \sqrt{(\gamma P_{i,1})^2 + 2(h_t)_{\text{wall}}(\gamma-1)^2(C_i^2+D_i^2)}\right\}$$

which is shown in Appendix B.

(6) Convergence is checked according to

$$\text{error} = \sum_{i=2}^{IM}\left|\frac{\rho_{i,1}^{k+1}-\rho_{i,1}^{k}}{\rho_{i,1}^{k+1}}\right| \leq \epsilon$$

where ϵ is a specified small number (typically 0.01).

(7) If the convergence criterion is not met, then

$$\begin{aligned} C_i &= C_i \cdot R \\ D_i &= D_i \cdot R \end{aligned}$$

where

$$R = \frac{1}{\rho_{i,1}^{k}}\left[W_1\rho_{i,1}^{k+1} + W_2\rho_{i,2}\right]$$

W_1 and W_2 are weighting functions, such that $W_1 + W_2 = 1.0$.

Now $\rho_{i,1}^{k}$ is set equal to $\rho_{i,1}^{k+1}$ and steps 3 through 7 are repeated. The iteration will continue until a converged solution is reached.

2.8 Initial Solution and Marching Time Step Determination

For hyperbolic equations, initial conditions must be specified. To solve the finite difference equation, either a fixed or variable time step may be used for the marching process. The CFL (or Courant) number criterion has been used in the explicit formulations and can also be treated as the reference for $\Delta\tau$ in the implicit formulations. Therefore, for the one-dimensional problem,

$$\Delta\tau = \frac{[CFL] \cdot \Delta x}{\lambda_{\max}}$$

For the two-dimensional/axisymmetric problem,

$$\Delta\tau = \left(\frac{[CFL_\xi]\Delta\xi}{|\lambda_\xi|_{\max}} \quad , \quad \frac{[CFL_\eta]\Delta\eta}{|\lambda_\eta|_{\max}} \right)_{\min}$$

There are various methods to specify the initial solutions. A simple way of doing this is to use the free stream properties for the entire domain (except the boundaries). This procedure is usually referred to as cold start. Another scheme is to presume a shock wave in the domain and determine the post shock properties by the Rankine-Hugoniot relations. However, for blunt body problems, the improperly specified properties in the subsonic region can easily cause the solution to diverge. Therefore, for multi-dimensional problems, the "cold start" will be used in this investigation.

Chapter 3

Nonequilibrium Chemistry Equations

3.1 Introductory Remarks

In this chapter, the nonequilibrium chemistry model is applied to the species continuity equations for quasi one-dimensional nozzle flow and for two-dimensional/axisymmetric flow. The translational, rotational, and vibrational modes of internal energy for molecules are described by the quantum mechanics theory, and a five reactant species model (N_2, O_2, NO, O, N) is employed for the high temperature air composition. A loosely coupled method of communicating the gas dynamic and chemistry equations is performed by utilizing the effective γ scheme (or the β method [31, 35]).

3.2 General Description of Gases

3.2.1 Thermally Perfect Gas Assumption

Gases considered in this research are assumed to follow the thermally perfect relation. That is, for a species s of the gases, the following relation holds:

$$P_s = \rho_s R_s T \tag{3.1}$$

where P_s is the partial pressure contributed by species s, ρ_s is the partial density contributed by species s, R_s is the gas constant for species s (note that $R_s = \frac{R_u}{M_s}$ where R_u is the universal gas constant and M_s is the molecular

weight of s) and T is the temperature. The perfect gas assumption implies that (i) the volume of the gas molecules is negligible, and (ii) the forces between the molecules are neglected. This assumption holds for a real gas at low pressures; however, a real gas approximates a perfect gas as long as the gas temperature is high. The discrepancies from the perfect gas law can be expressed by a departure from unity of $z = P_s/\rho_s R_s T$, defined as the compressibility factor. The compressibility factor z is plotted as functions of the reduced pressure $P_r = P/P_c$ and reduced temperature $T_r = T/T_c$ (Figure 3-1 [44]). The values of P_c, T_c for different gases are listed in Table 3-1.

For hypersonic problems, high pressures are always associated with high temperatures (post shock properties) and low temperatures with low pressures (free stream properties), thus z will be approximately equal to unity for most cases. Therefore, the perfect gas assumption may be used for such situations.

3.2.2 Dalton's Law of Partial Pressures

For a perfect gas, Dalton's law of partial pressures can be utilized to evaluate the pressure of a mixture of different gases. That is

$$\begin{aligned} P &= \sum_s P_s = \sum_s \rho_s R_s T = \sum_s (\rho C_s)\left(\frac{R_u}{M_s}\right) T = \rho T \sum_s \left(\frac{C_s R_u}{M_s}\right) \\ &= \rho T R \end{aligned} \tag{3.2}$$

where C_s is the mass fraction of species s defined by:

$$C_s = \rho_s/\rho \tag{3.3}$$

which leads to the obvious conclusion that

$$\sum_s C_s = 1 \tag{3.4}$$

From equation (3.2), the gas constant of a mixture can be defined as

$$R = \sum_s \frac{C_s R_u}{M_s} \tag{3.5}$$

3.2.3 Thermodynamic Properties for a Single Species

The internal energy (per unit of mass) of a gas according to its different origination can be written as

$$\epsilon_s = \epsilon_{t,s} + \epsilon_{e,s} + \epsilon_{o,s} \tag{3.6}$$

for atoms and

$$\epsilon_s = \epsilon_{t,s} + \epsilon_{r,s} + \epsilon_{v,s} + \epsilon_{e,s} + \epsilon_{o,s} \tag{3.7}$$

for molecules. Note the subscript s represents the species s. In the above equations, $\epsilon_{t,s}$ represents the translational energy. Since a molecule (or an atom) has three components of translational velocity, the corresponding kinetic energies about the center of mass contribute to the translational energy. From classical kinetic theory (theorem of equipartition of energy) as well as modern statistical thermodynamics, the translational energy is expressed as

$$\epsilon_{t,s} = \frac{3}{2}\left(\frac{R_u}{M_s}\right) T \tag{3.8}$$

The term $\epsilon_{r,s}$ represents the rotational energy about the center of mass of a molecule; for atoms, the moment of inertia is negligible and, therefore,

rotational energy is ignored. For a diatomic molecule with a "dumbbell" model, the rotational energy is described as

$$\epsilon_{r,s} = \frac{2}{2}\left(\frac{R_u}{M_s}\right)T \tag{3.9}$$

The term $\epsilon_{v,s}$ represents the vibrational energy for a molecule. It includes the kinetic energy of the linear motion of the atoms as they vibrate back and forth and the intramolecular potential energy. It is predicted to be $\left(\frac{R_u}{M_s}\right)T$ by the classical kinetic theory, but modern quantum mechanics theory determines it to be

$$\epsilon_{v,s} = \left(\frac{R_u}{M_s}\right)\cdot\theta_s/\left[exp(\theta_s/T)-1\right] \tag{3.10}$$

where θ_s is the characteristic temperature. Equation (3.10) is the one used in this research.

The term $\epsilon_{e,s}$ represents the electronic energy. It is composed of the kinetic energy due to electron's orbital motion about the nucleus and potential energy due to the electromagnetic force field established between the electron and nucleus. However, there is no available closed-form expression for $\epsilon_{e,s}$ [45]. When the fluid of concern is air, the errors due to neglecting this energy is less than 1% [28]. In this research, the electronic energy is neglected.

The term $\epsilon_{o,s}$ represents the zero-point energy, i.e., the energy of any species at absolute zero temperature. Under these conditions, molecules still have some finite translational motion (although very small) as well as some vibrational motion. In addition, there should be some energy in maintaining

electronic motion; otherwise, electrons would fall into the nucleus and the atom would collapse. However, $\epsilon_{o,s}$ cannot be calculated or measured. What is important in a chemical reaction is the change in zero-point energy and not the zero-point energy itself. Therefore, the change of zero-point energy from atoms to molecules (the heat of formation, $h_{o,s}$) can be used to replace the absolute value of $\epsilon_{o,s}$.

Now equations (3.8), (3.9) and (3.10) are substituted into equations (3.6), (3.7), and the zero-point energy ($\epsilon_{o,s}$) is replaced by the heat of formation ($h_{o,s}$). As discussed previously, both the electronic energy ($\epsilon_{e,s}$) in equation (3.6) and equation (3.7) are neglected. Thus, the internal energy per unit mass of species s can be expressed as

$$\epsilon_s = \frac{3}{2}\left(\frac{R_u}{M_s}\right)T + h_{o,s} \quad \text{for atoms} \tag{3.11}$$

and

$$\epsilon_s = \frac{5}{2}\left(\frac{R_u}{M_s}\right)T + \frac{R_u}{M_S}\cdot\theta_s/\left[\exp(\theta_s/T)-1\right] + h_{o,s} \quad \text{for molecules} \tag{3.12}$$

Values of R_u, M_s, θ_s, $h_{o,s}$ for the 5 species are listed in Table 3-2. Now the internal energy for a mixture of gases can be expressed as

$$e = \sum_{s=1}^{5} C_s\epsilon_s \tag{3.13}$$

where, by definition, $h = e + pv$.

3.3 Chemical Reactions and Rate Equations

3.3.1 Chemical Reactions

Chemical reactions considered in this research work are:

$$O_2 + M \underset{\leftarrow}{\rightarrow} 2O + M \tag{3.14}$$

$$N_2 + M \underset{\leftarrow}{\rightarrow} 2N + M \tag{3.15}$$

$$NO + M \underset{\leftarrow}{\rightarrow} N + O + M \tag{3.16}$$

$$NO + O \underset{\leftarrow}{\rightarrow} N + O_2 \tag{3.17}$$

$$O + N_2 \underset{\leftarrow}{\rightarrow} N + NO \tag{3.18}$$

where M represents the "non-reacting heavy particles" and can be any one of the five reactants (i.e., O_2, N_2, NO, O, N).

The five reactions (Equations (3.14) through (3.18)) are the most important reactions for air with temperature lower than 8000 K. However, another reaction which may occur but is neglected is the "dissociative-recombination reaction", that is

$$N + O \underset{\leftarrow}{\rightarrow} NO^+ + e^-$$

The reason for neglecting this reaction is first due to computational concern, i.e., if this reaction is included, then the total species number will be seven and more computer time and memory size will be required. Second, from a physical point of view, the amounts of ionized species (i.e., NO^+ and e^-) are not so prominent compared with the other five species for temperatures lower than 8000 K [8].

3.3.2 Rate Equations

For a chemical reaction with n reacting species, the general chemical reaction can be written as

$$\sum_{s=1}^{n} a_s X_s \underset{K_b}{\overset{K_f}{\rightleftharpoons}} \sum_{s=1}^{n} b_s X_s \tag{3.19}$$

where a_s and b_s represent the stoichiometric mole numbers of the reactants and products of species s, respectively.

K_f and K_b represent the forward reaction rate and backward reaction rate, respectively. Usually, K_f is empirically determined and correlated in the form as

$$K_f = CT^n \exp[-E/KT] \tag{3.20}$$

where K is the Boltzmann constant, E is the activation energy, C and n are constants. The values of E, C, and n are determined experimentally [46], and are listed in Appendix C for the five reactions in Section 3.3.1. Note that K_b can be evaluated by

$$K_b = K_f/K_e \tag{3.21}$$

where K_e is the equilibrium constant and is written in the following form

$$K_e = \exp(A_1 + A_2 \ell nZ + A_3 Z + A_4 Z^2 + A_5 Z^3) \tag{3.22}$$

where $Z = 10{,}000/T$. All the curve-fitting coefficients A_1 through A_5 can be found in Appendix C. Also, note that the rate constants (K_f, K_b, K_e) are functions of temperature only. If the concentration X_s (the mole number of

species s per unit volume, i.e., $[X_s] = \rho C_s/M_s$) is written as $[X_s]$, the net rate of formation of $[X_s]$ from equation (3.19) is expressed as

$$\left.\frac{d[X_s]}{dt}\right|_{\text{net}} = \left.\frac{d[X_s]}{dt}\right|_{\text{forward}} + \left.\frac{d[X_s]}{dt}\right|_{\text{backward}} \tag{3.23}$$

where

$$\left.\frac{d[X_s]}{dt}\right|_{\text{forward}} = (b_s - a_s)K_f \cdot \Pi_s[X_s]^{a_s} \tag{3.24}$$

is the rate of formation of $[X_s]$ as reaction (3.19) takes place from left to right and

$$\left.\frac{d[X_s]}{dt}\right|_{\text{backward}} = -(b_s - a_s)K_b\Pi_s[X_s]^{b_s} \tag{3.25}$$

is the rate of formation of $[X_s]$ as reaction (3.19) takes place from right to left. Note that if $\left.\frac{d[X_s]}{dt}\right|_{\text{net}} = 0$, then the reaction is in the "equilibrium" state.

The total net rate of $[X_s]$ is the summation of the net rate of $[X_s]$ from the five reactions (equations (3.14) through (3.18)), and the final closed form of $\frac{d[X_s]}{dt}$ for the five species is listed in Appendix D.

3.4 Quasi One-Dimensional Species Continuity Equations

The nonequilibrium species continuity equations for a quasi one-dimensional flow can be written in a vector form as [47]

$$\frac{\partial SQ_c}{\partial t_c} + \frac{\partial E_c}{\partial x} + SW = 0 \tag{3.26}$$

where S is the cross-section area and

$$Q_c = \begin{bmatrix} \rho C_1 \\ \rho C_2 \\ \rho C_3 \\ \rho C_4 \\ \rho C_5 \end{bmatrix} \qquad E_c = \begin{bmatrix} \rho u C_1 S \\ \rho u C_2 S \\ \rho u C_3 S \\ \rho u C_4 S \\ \rho u C_5 S \end{bmatrix} \qquad W = - \begin{bmatrix} \dot{w}_1 \\ \dot{w}_2 \\ \dot{w}_3 \\ \dot{w}_4 \\ \dot{w}_5 \end{bmatrix}$$

The subscript number used above represents reactant as:

1	for	O_2
2	for	N_2
3	for	NO
4	for	O
5	for	N

$\dot{w}_s$ represents the mass production rate of species s and

$$\dot{w}_s = M_s \cdot \frac{d[X_s]}{dt} \tag{3.27}$$

$\frac{d[X_s]}{dt}$ for the five species are listed in Appendix D.

Note that, from the mass conservation principle, $\sum_{s=1}^{5} \dot{w}_s = 0$ (total mass of the system is conserved). Therefore, the 5 species continuity equations (3.26) must sum to the global continuity equation (2.1). A similar linearization procedure used for equations (2.7) and (2.9) is employed for equation (3.26)

which results in the Jacobian matrix A_c as

$$A_c = \frac{\partial E_c}{\partial Q_c} = S \begin{bmatrix} u & & & 0 \\ & u & & \\ & & u & \\ & & & u \\ 0 & & & u \end{bmatrix} \tag{3.28}$$

Also, the Jacobian matrix D is defined as $D = \frac{\partial W}{\partial Q_c}$. The closed form of D is expressed in Appendix E. Note that $\dot{w}_s$ in W is assumed to be a function of density and species mass-fraction only; the K_f and K_b are treated as constant during each time level.

The matrix A_c has multiple eigenvalues given as Su. For a one-dimensional flow, u is always positive and, therefore, for the flux-splitting method, $A_c^+ = A_c$, $A_c^- = 0$, $E_c^+ = E_c$, and $E_c^- = 0$. The flux-split implicit finite difference equation of (3.26) can be expressed as

$$S_i \left(\frac{Q_{c(i)}^{n+1} - Q_{c(i)}^{n}}{\Delta t_c} \right) + \left(\frac{E_{c(i)}^{n+1} - E_{c(i-1)}^{n+1}}{\Delta x} \right) + S_i W_i^{n+1} = 0 \tag{3.29}$$

One can substitute $E_c^{n+1} = E_c^n + A_c \Delta Q_c$ and $W^{n+1} = W^n + D\Delta Q_c$ into equation (3.29) and rearrange terms, so that equation (3.29) can be expressed as:

$$CBM_i \Delta Q_{c(i-1)} + CB_i \Delta Q_{c(i)} = RHS_i \tag{3.30}$$

where

$$\begin{aligned} CBM_i &= \frac{-\Delta t_c}{\Delta x} A_{c(i-1)} \\ CB_i &= S_i I + \Delta t_c \left(\frac{A_{c(i)}}{\Delta x} + S_i D_i \right) \\ RHS_i &= \left[\frac{E_{c(i-1)} - E_{c(i)}}{\Delta x} - S_i W_i \right] \Delta t_c \end{aligned}$$

A bidiagonal block matrix system is formed when equation (3.30) is applied to each grid point i of the computational domain (see Figure 2.1), the matrix system is written as

$$\begin{bmatrix} CB_2 & & & \\ CBM_3 & CB_3 & & \\ & & CBM_{IMM2} & CB_{IMM2} \\ & & & CBM_{IMM1} \end{bmatrix} \begin{bmatrix} \Delta Q_{c(2)} \\ \Delta Q_{c(3)} \\ \vdots \\ \Delta Q_{c(IMM2)} \\ \Delta Q_{c(IMM1)} \end{bmatrix} = \quad (3.31)$$

$$\begin{bmatrix} RHS_2 - CBM_2 \Delta Q_{c(1)} \\ RHS_3 \\ \vdots \\ RHS_{IMM2} \\ RHS_{IMM1} - CB_{IM} \Delta Q_{c(IM)} \end{bmatrix}$$

With the boundary condition $\Delta Q_{c(1)} = 0$ for free stream and $\Delta Q_{c(IM)} = \Delta Q_{c(IMM1)}$ (zero order extrapolation) for exit plane, equation (3.31) can be rewritten as

$$\begin{bmatrix} CB_2 & & & \\ CBM_3 & CB_3 & & \\ & & CBM_{IMM2} & CB_{IMM2} \\ & & & \overline{CBM}_{IMM1} \end{bmatrix} \begin{bmatrix} \Delta Q_{c(2)} \\ \Delta Q_{c(3)} \\ \vdots \\ \Delta Q_{c(IMM2)} \\ \Delta Q_{c(IMM1)} \end{bmatrix} =$$

$$\begin{bmatrix} RHS_2 \\ RHS_3 \\ \vdots \\ RHS_{IMM2} \\ RHS_{IMM1} \end{bmatrix} \quad (3.32)$$

where $\overline{CBM}_{IMM1} = CBM_{IMM1} + CB_{IM}$.

The manner in which this system is coupled to the Euler equations is presented in Section 3.7.

3.5 Two-Dimensional and Axisymmetric Species Continuity Equations

The nonequilibrium species continuity equations for the two-dimensional/ axisymmetric flow are written in a vector form as

$$\frac{\partial Q_c}{\partial t_c} + \frac{\partial E_c}{\partial x} + \frac{\partial F_c}{\partial y} + \alpha H_c + W = 0 \tag{3.33}$$

where

$$Q_c = \begin{bmatrix} \rho C_1 \\ \rho C_2 \\ \rho C_3 \\ \rho C_4 \\ \rho C_5 \end{bmatrix} , \; E_c = \begin{bmatrix} \rho u C_1 \\ \rho u C_2 \\ \rho u C_3 \\ \rho u C_4 \\ \rho u C_5 \end{bmatrix} , \; F_c = \begin{bmatrix} \rho v C_1 \\ \rho v C_2 \\ \rho v C_3 \\ \rho v C_4 \\ \rho v C_5 \end{bmatrix} , \; H_c = F_c/y \; , \; W = \begin{bmatrix} -\dot{w}_1 \\ -\dot{w}_2 \\ -\dot{w}_3 \\ -\dot{w}_4 \\ -\dot{w}_5 \end{bmatrix}$$

and

$$\alpha = \begin{cases} 0 & \text{for a two-dimensional planar flow} \\ 1 & \text{for a two-dimensional axisymmetric flow} \end{cases}$$

The equation (3.33) is transformed from physical space to computational space by applying the generalized coordinate transformation. The transformed equation

$$\frac{\partial \bar{Q}_c}{\partial t_c} + \frac{\partial \bar{E}_c}{\partial \xi} + \frac{\partial \bar{F}_c}{\partial \eta} + \alpha \bar{H}_c + \bar{W} = 0 \tag{3.34}$$

For a time independent grid system (i.e., $\xi_t = 0$ and $\eta_t = 0$); thus,

$$\bar{Q}_c = \frac{Q_c}{J}$$

$$\bar{E}_c = \frac{1}{J}\left[\xi_x E_c + \xi_y F_c\right]$$

$$\bar{F}_c = \frac{1}{J}\left[\eta_x E_c + \eta_y F_c\right]$$

$$\bar{H}_c = \frac{H_c}{J}$$

$$\bar{W}_c = \frac{W}{J}$$

where J is defined by equation (2.41).

An implicit finite difference formulation applied to equation (3.34) yields:

$$\frac{\bar{Q}_c^{n+1} - \bar{Q}_c^n}{\Delta tc} + \left(\frac{\partial \bar{E}_c}{\partial \xi}\right)^{n+1} + \left(\frac{\partial \bar{F}_c}{\partial \eta}\right)^{n+1} + \alpha \bar{H}_c^{n+1} + \bar{W}^{n+1} = 0 \qquad (3.35)$$

Utilizing the same linearization procedures described in Section 2.5 and defining $\frac{\partial \bar{E}_c}{\partial \bar{Q}_c} = A_c$, $\frac{\partial \bar{F}_c}{\partial \bar{Q}_c} = B_c$, $\frac{\partial \bar{H}_c}{\partial \bar{Q}_c} = C_c$ and $\frac{\partial \bar{W}}{\partial \bar{Q}_c} = D$, equation (3.35) can be linearized as

$$\left\{I + \Delta t_c \left[\frac{\partial A_c^n}{\partial \xi} + \frac{\partial B_c^n}{\partial \eta} + \alpha C_c^n + D^n\right]\right\} \Delta \bar{Q} = -\Delta t_c \left\{\frac{\partial \bar{E}_c^n}{\partial \xi} + \frac{\partial \bar{F}_c}{\partial \eta} + \alpha \bar{H}_c^n + \bar{W}^n\right\} \qquad (3.36)$$

where

$$A_c = (u\xi_x + v\xi_y) \cdot I \qquad (3.37)$$

$$B_c = (u\eta_x + v\eta_y) \cdot I \qquad (3.38)$$

$$C_c = \left(\frac{v}{y}\right) \cdot I \qquad (3.39)$$

D is described in Appendix E, and I is the five by five identity matrix. Before applying the flux-splitting method to the spatial derivatives of equation (3.36), the eigenvalues of A_c and B_c must be determined. Due to the simple form

of equations (3.37) and (3.38), the eigenvalues can be easily determined by inspection. For matrix A_c, the eigenvalues are multiple roots of $u\xi_x + v\xi_y$; and for matrix B_c, they are multiple roots of $u\eta_x + v\eta_y$. The results are summarized as:

$$\text{For matrix } A_c, \begin{cases} \text{if } u\xi_x + v\xi_y \geq 0 \quad \text{then} & \begin{array}{l} A_c^+ = A_c \ , \ A_c^- = 0 \\ \bar{E}_c^+ = \bar{E}_c, \ \bar{E}_c^- = 0 \end{array} \\ \text{if } u\xi_x + v\xi_y < 0 \quad \text{then} & \begin{array}{l} A_c^+ = 0, \ A_c^- = A_c \\ \bar{E}_c^+ = 0, \ \bar{E}_c^- = \bar{E}_c \end{array} \end{cases}$$

$$\text{For matrix } B_c, \begin{cases} \text{if } u\eta_x + v\eta_y \geq 0 \quad \text{then} & \begin{array}{l} B_c^+ = B_c \ , \ B_c^- = 0 \\ \bar{F}_c^+ = \bar{F}_c, \ \bar{F}_c^- = 0 \end{array} \\ \text{if } u\eta_x + v\eta_y < 0 \quad \text{then} & \begin{array}{l} B_c^+ = 0, \ B_c^- = B_c \\ \bar{F}_c^+ = 0, \ \bar{F}_c^- = \bar{F}_c \end{array} \end{cases}$$

Now the flux split form of equation (3.36) is

$$\begin{aligned} &\left[I + \frac{\Delta t_c}{\Delta\xi}(A_c^+ - A_c^-) + \frac{\Delta t_c}{\Delta\eta}(B_c^+ - B_c^-) + \Delta t_c(\alpha C_c + D)\right]_{(i,j)} \Delta\bar{Q}_{c(i,j)} \\ &+ \left[\frac{\Delta t_c}{\Delta\xi} A^-_{c(i+1,j)}\right] \Delta\bar{Q}_{i+1,j} - \left[\frac{\Delta t_c}{\Delta\xi} A^+_{c(i-1,j)}\right] \Delta\bar{Q}_{c(i-1,j)} \\ &+ \left[\frac{\Delta t_c}{\Delta\eta} B^-_{c(i,j+1)}\right] \Delta\bar{Q}_{c(i,j+1)} \\ &- \left[\frac{\Delta t_c}{\Delta\eta} B^+_{c(i,j-1)}\right] \Delta\bar{Q}_{c(i,j-1)} = RHS_{i,j} \end{aligned} \tag{3.40}$$

where

$$\begin{aligned} RHS_{i,j} = \Delta t_c \Bigg\{ &\frac{1}{\Delta\xi}\left(\bar{E}^+_{c(i-1,j)} - \bar{E}^+_{c(i,j)} + \bar{E}^-_{c(i,j)} - \bar{E}^-_{c(i+1,j)}\right) \\ &+ \frac{1}{\Delta\eta}\left(\bar{F}^-_{c(i,j)} + \bar{F}^+_{c(i,j-1)} - \bar{F}^+_{c(i,j)} - \bar{F}^-_{c(i,j+1)}\right) \\ &- \alpha\bar{H}_{c(i,j)} - \bar{W}_{i,j} \Bigg\} \end{aligned} \tag{3.41}$$

Equation (3.40) can be factorized to provide two equations such that the original block pentadiagonal matrix system can be changed to two block tridiagonal matrix systems. These factorized equations are

$$CBM_{i,j}\Delta\bar{Q}^{*}_{c(i,j-1)} + CB_{i,j}\Delta\bar{Q}^{*}_{c(i,j)} + CBP_{i,j}\Delta\bar{Q}^{*}_{c(i,j+1)} = RHS_{i,j} \qquad (3.42)$$

and

$$CAM_{i,j}\Delta\bar{Q}_{c(i-1,j)} + CAi,j\Delta\bar{Q}_{c(i,j)} + CAP_{i,j}\Delta\bar{Q}_{c(i+1,j)} = \Delta\bar{Q}^{*}_{c(i,j)} \qquad (3.43)$$

where

$$CBM_{i,j} = \frac{-\Delta t_c}{\Delta\eta}B^{+}_{c(i,j-1)}$$

$$CB_{i,j} = I + \frac{\Delta t_c}{\Delta\eta}\left(B^{+}_{c(i,j)} - B^{-}_{c(i,j)}\right) + \Delta t_c\left(\alpha C_{c(i,j)} + D_{i,j}\right)$$

$$CBP_{i,j} = \frac{\Delta t_c}{\Delta\eta}B^{-}_{c(i,j+1)}$$

$$CAM_{i,j} = \frac{-\Delta t_c}{\Delta\xi}A^{+}_{c(i-1,j)}$$

$$CA_{i,j} = I + \frac{\Delta t_c}{\Delta\xi}\left(A^{+}_{c(i,j)} - A^{-}_{c(i,j)}\right)$$

$$CAP_{i,j} = \frac{\Delta t_c}{\Delta\xi}A^{-}_{c(i+1,j)}$$

3.6 Boundary Conditions

When equation (3.42) is written at each ξ for all j from $j = 2$ to $j = JMM1$, a block tridiagonal system is obtained with the same form as equation (2.77). However, $\Delta\bar{Q}^{*}_{c(i,1)}$ is set to equal $\Delta\bar{Q}^{*}_{c(i,2)}$ and $\Delta\bar{Q}^{*}_{c(i,JM)} = 0$ by the application of free stream condition. Therefore, the final form of the

matrix is expressed as

$$\begin{bmatrix} [\overline{CB}]_{i,2} & [CBP]_{i,2} & & & & \\ [CBM]_{i,3} & [CB]_{i,3} & [CBP]_{i,3} & & & \\ & & & [CBM]_{i,JMM2} & [CB]_{i,JMM2} & [CBP]_{i,JMM2} \\ & & & & [CBM]_{i,JMM1} & [CB]_{i,JMM1} \end{bmatrix} \text{(times)}$$

$$\begin{bmatrix} \Delta\bar{Q}^*_{c(i,2)} \\ \Delta\bar{Q}^*_{c(i,3)} \\ \\ \Delta\bar{Q}^*_{c(i,JMM2)} \\ \Delta\bar{Q}^*_{c(i,JMM1)} \end{bmatrix} = \begin{bmatrix} (RHS)_{i,2} \\ (RHS)_{i,3} \\ \\ (RHS)_{i,JMM2} \\ (RHS)_{i,JMM1} \end{bmatrix} \tag{3.44}$$

where $[\overline{CB}]_{i,2} = [CB]_{i,2} + [CBM]_{i,2}$. Equation (3.44) is solved from $i = 2$ to $i = IMM1$. Once all the $\Delta\bar{Q}^*_c$ are computed from equation (3.44) and the RHS of equation (3.43) is known, then equation (3.43) is applied for all i from $i = 2$ to $i = IMM1$. The resulting block tridiagonal system has the same form as equation (2.78) and can be solved from $j = 2$ to $j = JMM1$. Due to an imposed boundary condition at the surface, $\Delta\bar{Q}_{c(1,j)} = \Delta\bar{Q}_{c(2,j)}$ for the chemistry species equations. Therefore, $[\overline{CA}]_{2,j}$ in equation (2.79) is redefined as

$$[\overline{CA}]_{2,j} = [CA]_{2,j} + [CAM]_{2,j}$$

When the governing equation (3.34) is applied on the body surface, (Figure A.1), the flux-splitting method is still valid for the ξ derivatives. However, for the η derivatives, one-sided differences must be utilized. Therefore, by employing a second-order one-sided differences for the η derivatives, the finite difference equation can be expressed as:

$$\frac{\Delta\bar{Q}_{c(i,1)}}{\Delta t_c} + \frac{1}{\Delta\xi}\left[\bar{E}^+_{c(i,1)} - \bar{E}^+_{c(i-1,1)} + \bar{E}^-_{c(i+1,1)} - \bar{E}^-_{c(i,1)}\right]^{n+1}$$

$$+\frac{1}{2\Delta\eta}\left[-3\bar{F}_{c(i,1)}+4\bar{F}_{c(i,2)}-\bar{F}_{c(i,3)}\right]^{n+1}$$
$$+\alpha\bar{H}^{n+1}_{c(i,1)}+\bar{W}^{n+1}_{i,1}=0 \qquad (3.45)$$

Note that $\bar{F}_{c(i,1)}=0$, since $u\eta_x+v\eta_y=0$ on the body surface; also, $\bar{F}^{n+1}_{c(i,2)}$ and $\bar{F}^{n+1}_{c(i,3)}$ are known values. Thus, equation (3.45) can be expressed as

$$CDM_{i,1}\Delta\bar{Q}_{c(i-1,1)}+CD_{i,1}\Delta\bar{Q}_{c(i,1)}+CDP_{i,1}\Delta\bar{Q}_{c(i+1,1)}=CR_{i,1} \qquad (3.46)$$

where

$$\begin{aligned}
CDM_{i,1} &= -\frac{\Delta t_c}{\Delta\xi}A^{+}_{c(i-1,1)}\\
CD_{i,1} &= I+\frac{\Delta t_c}{\Delta\xi}\left(A^{+}_{c(i,1)}-A^{-}_{c(i,1)}\right)+\Delta t_c\left(\alpha C_{c(i,1)}+D_{i,1}\right)\\
CDP_{i,1} &= \frac{\Delta t_c}{\Delta\xi}A^{-}_{c(i+1,1)}\\
CR_{i,1} &= \Delta t_c\left[\frac{1}{\Delta\xi}\left(\bar{E}^{+}_{c(i-1,1)}-\bar{E}^{+}_{c(i,1)}+\bar{E}^{-}_{c(i,1)}-\bar{E}^{-}_{c(i+1,1)}\right)^{n}\right.\\
&\qquad \left.\frac{1}{2\Delta\eta}\left(\bar{F}_{c(i,3)}-4\bar{F}_{c(i,2)}\right)^{n+1}-\alpha\bar{H}^{n}_{c(i,1)}-\bar{W}^{n}_{c(i,1)}\right]
\end{aligned}$$

Equation (3.46) is written from $i=2$ to $i=IMM1$ to provide a matrix system expressed as

$$\begin{bmatrix}
\overline{CD}_{2,1} & CDP_{2,1} & & & & \\
CDM_{3,1} & CD_{3,1} & CDP_{3,1} & & & \\
 & & & & & \\
 & & CDM_{IMM2,1} & CD_{IMM2,1} & CDP_{IMM2,1} & \\
 & & & CDM_{IMM1,1} & \overline{CD}_{IMM1,1} &
\end{bmatrix} \text{(times)}$$

$$\begin{bmatrix} \Delta\bar{Q}_{c(2,1)} \\ \Delta\bar{Q}_{c(3,1)} \\ | \\ \Delta\bar{Q}_{c(IMM2,1)} \\ \Delta\bar{Q}_{c(IMM1,1)} \end{bmatrix} = \begin{bmatrix} CR_{2,1} \\ CR_{3,1} \\ | \\ CR_{IMM2,1} \\ CR_{IMM1,1} \end{bmatrix} \tag{3.47}$$

where $\overline{CD}_{2,1} = CD_{2,1} + CDM_{2,1}$, since $\Delta\bar{Q}_{c(1,1)} = \Delta\bar{Q}_{c(2,1)}$, $\overline{CD}_{IMM,1} = CD_{IMM1,1} + CDP_{IMM1,1}$, for $\Delta\bar{Q}_{c(IM,1)} = \Delta\bar{Q}_{c(IMM1,1)}$.

3.7 Coupling of the Gas Dynamic and Chemistry Equations

The Euler equations (described in Chapter 2) and the species continuity equations are communicated by using a loosely coupled approach. In this approach, a thermodynamic property γ is defined to perform the role of the communicator [31], [34], [35]. In this research, γ is defined as

$$\gamma = \frac{h}{e} \quad \text{or} \quad \gamma = \left(\frac{P}{\rho e}\right) + 1 \tag{3.48}$$

Note that γ is a variable that depends on species mass fractions and temperature. The loosely coupled scheme is described step by step as follows:

(1) Euler equations are solved for the unknowns, i.e., ΔQs by scheme described in Chapter 2. This solution will be designated by "*" to distinguish it from the solution obtained after the chemistry adjustment. Note that at this step the time marching is with respect to $\Delta\tau$ ($\Delta\tau$ is the non-dimensional time). Therefore, the Euler solution (re-dimensionalized variables) yields:

$$\rho^* = \rho^n + \Delta\rho$$

$$
\begin{aligned}
(\rho u)^* &= (\rho u)^n + \Delta(\rho u) \\
(\rho v)^* &= (\rho v)^n + \Delta(\rho v) \\
e_t^* &= e_t^n + \Delta e_t
\end{aligned}
$$

Auxiliary variables such as pressure (p^*), temperature (T^*), ...etc. can be calculated using the four primary variables.

Note that mass fractions (C_s^n), γ^n, and the gas constant of mixture (R^n) are held constant in this step, i.e., at their previous values.

(2) Evaluate $\dot{w}_s$ (see equation (3.27)) by using T^*, C_s^n, and ρ^*. Then unknowns $\Delta(\rho C_s)$ in the chemistry equations can be evaluated by utilizing C_s^n, ρ^*, $(\rho u)^*$, $(\rho v)^*$, and $\dot{w}_s$. Now intermediate partial densities are evaluated by

$$(\rho C_s)^* = \rho^* C_s^n + \Delta(\rho C_s) \tag{3.49}$$

Then the species mass fraction is updated by

$$C_s^{n+1} = \frac{(\rho C_s)^*}{\sum_{s=1}^{5}(\rho C_s)^*} \tag{3.50}$$

and the mixture gas constant is updated by

$$R^{n+1} = \sum_{s=1}^{5} \frac{C_s^{n+1} Ru}{M_s} \tag{3.51}$$

(3) Update the temperature by assuming that pressure (p^*), fluxes $\Big((\rho u)^*$, $(\rho v)^*\Big)$, and total enthalpy (h_t^*) are invariant variables during the chemistry step (2). Therefore,

$$p^* = p^{n+1} ,$$

$$\begin{aligned} h_t^* &= h_t^{n+1}\,, \\ (\rho u)^* &= (\rho u)^{n+1} \\ (\rho v)^* &= (\rho v)^{n+1} \end{aligned}$$

Recall that

$$h_t^{n+1} = e^{n+1} + \frac{1}{2}\left[(u^{n+1})^2 + (v^{n+1})^2\right] + R^{n+1}T^{n+1} \tag{3.52}$$

and

$$e^{n+1} = \sum_{s=1}^{5} C_s^{n+1} \cdot \epsilon_s \tag{3.53}$$

$$\begin{aligned} u^{n+1} &= \frac{(\rho u)^{n+1}}{\rho^{n+1}} = \frac{(\rho u)^*}{p^{n+1}/(R^{n+1}T^{n+1})} \\ &= \frac{(\rho u)^* R^{n+1}T^{n+1}}{p^*} \end{aligned} \tag{3.54}$$

In a similar fashion

$$v^{n+1} = \frac{(\rho v)^* R^{n+1}T^{n+1}}{p^*} \tag{3.55}$$

Note that ϵ_s is a function of T^{n+1} only and is defined by equation (3.11) (for atoms) and by equation (3.12) (for molecules). Substitution of equations (3.53) through (3.55) into equation (3.52), yields:

$$\begin{aligned} h_t^{n+1} = &\sum_{s=1}^{5} C_s^{n+1}\epsilon_s + \frac{1}{2}\left\{\left[\frac{(\rho u)^*}{p^*}\right]^2 + \left[\frac{(\rho v)^*}{p^*}\right]^2\right\}(R^{n+1})^2(T^{n+1})^2 \\ &+ R^{n+1}T^{n+1} = h_t^* \end{aligned} \tag{3.56}$$

The unknown in equation (3.56) is the temperature T^{n+1} which is determined by using the Newton-Raphson method.

(4) Once temperature is updated, then all the properties can be recomputed as:

$$\begin{aligned}
\rho^{n+1} &= \frac{P^*}{R^{n+1}T^{n+1}} \\
u^{n+1} &= \frac{(\rho u)^*}{\rho^{n+1}} \quad , \quad v^{n+1} = \frac{(\rho v)^*}{\rho^{n+1}} \\
e_t^{n+1} &= h_t^* - \frac{p^*}{\rho^{n+1}} \\
e^{n+1} &= e_t^{n+1} - \frac{1}{2}\left[(u^{n+1})^2 + (v^{n+1})^2\right] \quad , \text{ and} \\
\gamma^{n+1} &= \frac{p^*}{\rho^{n+1}e^{n+1}} + 1
\end{aligned}$$

(5) Return to step (1) and replace all the values superscripted n with the updated values superscripted $n+1$.

These steps are repeated until a convergence criterion is satisfied. Usually, the criterion is expressed as

$$\sum_{i=1,j=1}^{N} \frac{|r_{i,j}^{n+1} - r_{i,j}^{n}|}{r_{i,j}^{n}} < \epsilon$$

where r is a property, such as temperature or species mass fractions, and ϵ is a prescribed value.

Chapter 4

Stability Analysis of Nonequilibrium Chemistry Equations

4.1 Introductory Remarks

The nonequilibrium phenomena introduce an important stability criterion in the marching time step Δt_c. For many problems, the chemistry time step Δt_c will be much smaller than the gas dynamics time step Δt_g due to the stiff nature of the rate equations. (Note that $\Delta t_g = \Delta t$ in equation (2.6) and $\Delta t_g = \Delta \tau * \frac{L}{U_\infty}$ since the $\Delta \tau$ in equation (2.42) is a nondimensional form.) Several methods are available to evaluate the required Δt_c. These include,

(i) $\Delta t_c \leq 0.1/|\dot{w}_s|$ [48]

(ii) $\Delta t_c \leq (0.1)\left(\min\left|\frac{\rho C_s}{\dot{w}_s}\right|\right)$ [49]

(iii) $\Delta t_c \leq B\Gamma$ [8, 49, 50]

where $\Gamma = \rho\left(\frac{\partial \dot{w}_s}{\partial C_s}\right)^{-1}$ and B is determined such that $0 < B < 1$ by numerical experimentation. However, no mathematical arguments are provided to establish these criteria and their relations to the stability of the solution.

In this chapter, the stability is investigated by applying the von Neumann stability analysis on the linearized coupled species equations. The scheme predicts the chemical time step which assures a convergent solution.

4.2 Von Neumann Analysis for Quasi One-Dimensional Chemistry Equations

Recall equation (3.26) for the quasi one-dimensional species continuity equations:

$$\frac{\partial SQ_c}{\partial tc} + \frac{\partial E_c}{\partial x} + SW = 0 \tag{4.1}$$

Equation (4.1) is changed to a quasi-linear system by the following substitutions:

$$\frac{\partial E_c}{\partial x} = [A_c] \frac{\partial (Q_c S)}{\partial x} \tag{4.2}$$

and

$$W = [M] Q_c \tag{4.3}$$

where

$$[A_c] = u[I] \tag{4.4}$$

and $[I]$ represents the 5×5 identity matrix and $[M]$ is given in Appendix F. Substitute equation (4.2) through (4.4) into equation (4.1) and replace $[M]$ by $[M][I]$; then the linearized equations are expressed as

$$\frac{\partial (SQ_c)}{\partial t_c} + u[I] \frac{\partial (SQ_c)}{\partial x} + [M][I](SQ_c) = 0 \tag{4.5}$$

The eigenvalues of M are denoted by $[d_1, d_2, d_3, d_4, d_5]^T$ and the corresponding eigenvector matrix by $[Z]$, i.e.,

$$[Z]\,[M]\,[Z]^{-1} = \begin{bmatrix} d_1 & & & 0 & \\ & d_2 & & & \\ & & d_3 & & \\ & 0 & & d_4 & \\ & & & & d_5 \end{bmatrix} \tag{4.6}$$

Equation (4.5) is multiplied by $[Z]^{-1}$ to provide

$$[Z]^{-1}\frac{\partial(SQ_c)}{\partial t_c}+u\,[Z]^{-1}\,[Z]\;[Z]^{-1}\frac{\partial(SQ_c)}{\partial x}+[Z]^{-1}\,M\,[Z]\;[Z]^{-1}\,(SQ_c)=0 \quad (4.7)$$

Note that $[I]$ is replaced by $[Z]\;[Z]^{-1}$ in the operation above. Since $[M]$, $[Z]$ and $[Z]^{-1}$ are assumed "frozen", equation (4.7) can be rewritten as

$$\frac{\partial([Z]^{-1}SQ_c)}{\partial t_c}+u\,[Z]^{-1}\;[Z]\,\frac{\partial([Z]^{-1}SQ_c)}{\partial x}+[Z]^{-1}\,M\,[Z]\,([Z]^{-1}\,SQ_c)=0 \quad (4.8)$$

Substitution of equation (4.6) into equation (4.8) yields

$$\frac{\partial[R]}{\partial t_c}+u\,[I]\,\frac{\partial[R]}{\partial x}+\begin{bmatrix} d_1 & & & 0 & \\ & d_2 & & & \\ & & d_3 & & \\ & 0 & & d_4 & \\ & & & & d_5 \end{bmatrix}[R]=0 \quad (4.9)$$

where $[R] = [Z]^{-1}SQ_c = [R_1,\ R_2,\ R_3,\ R_4,\ R_5]^T$. Note that equation (4.9) represents five decoupled scalar equations, where the "s"th equation may be expressed as

$$\frac{\partial R_s}{\partial t_c}+u\frac{\partial R_s}{\partial x}+d_sR_s=0 \quad (4.10)$$

where $s = 1, \ldots 5$. Equation (4.10) is discretized explicitly to provide

$$\frac{R^{n+1}_{s(i)}-R^n_{s(i)}}{\Delta t_c}+u_i\frac{R^n_{s(i)}-R^n_{s(i-1)}}{\Delta x}+d_{s(i)}R^n_s=0 \quad (4.11)$$

Note that the backward difference approximation of the convective term is used, because u is positive for a quasi one-dimensional flow. The numerical solution of R_s may be written as

$$R_s = D+\epsilon \quad (4.12)$$

where D is the exact solution and ϵ is the error. Since the exact solution must satisfy the difference equation (4.11); therefore, substituting equation (4.12)

into (4.11) yields

$$\frac{\epsilon_i^{n+1} - \epsilon_i^n}{\Delta t_c} + u_i \frac{(\epsilon_i^n - \epsilon_{i-1}^n)}{\Delta x} + d_{s_{(i)}} \epsilon_i^n = 0 \tag{4.13}$$

The error (ϵ) is assumed to be

$$\epsilon_i = e^{at} e^{Ik(i\Delta x)} \tag{4.14}$$

where

$$\begin{aligned} I &= \sqrt{-1} \\ k &= \frac{i\pi}{L} \end{aligned} \tag{4.15}$$

L is the total length of the computational domain. Substitution of equation (4.14) into equation (4.13) yields

$$e^{at} e^{Ik(i\Delta x)} \left[\frac{e^{a\Delta t_c} - 1}{\Delta t_c} + u_i \frac{(1 - e^{-Ik\Delta x})}{\Delta x} + d_{s_{(i)}} \right] = 0 \tag{4.16}$$

Therefore,

$$\frac{e^{a\Delta t_c}}{\Delta t_c} = \frac{1}{\Delta t_c} - d_{s_{(i)}} - u_i \frac{(1 - \cos\theta + I \sin\theta)}{\Delta x} \tag{4.17}$$

where

$$\theta = k\Delta x \tag{4.18}$$

Multiplying equation (4.17) by Δt_c yields

$$e^{a\Delta t_c} = 1 - \lambda s_i \Delta t_c \tag{4.19}$$

where λs_i is defined as

$$\lambda s_i = \frac{u_i}{\Delta x}(1 - \cos\theta) + Re[d_{s_{(i)}}] + I \left(\frac{u_i}{\Delta x} \sin\theta + Im[d_{s_{(i)}}] \right) \tag{4.20}$$

and Re represents the real part of a complex variable. Im represents the imaginary part of a complex variable. The amplification factor G_{ex} can be written as

$$G_{ex} = \left| e^{a\Delta t_c} \right| = \sqrt{(1 - Re[\lambda_s]\Delta t_c)^2 + (Im[\lambda_s]\Delta t_c)^2} \tag{4.21}$$

Note that the subscript i used in equation (4.20) is dropped. If the amplification factor G_{ex} given by (4.21) is bounded ,i.e., $|G| \leq 1$, the error will not grow and the numerical solution is stable. From equation (4.21), it can be concluded that the G_{ex} will be greater than one as long as $Re[\lambda_s] < 0$. That is, the solution will become unstable if $\frac{u}{\Delta x}(1 - \cos\theta) + Re[d_s] < 0$. However, careful examination of equation (4.21) suggests that G_{ex} may be greater than one even for $Re[\lambda_s] > 0$. Imposing the stability requirement of $G_{ex} \leq 1$, results in

$$\Delta t_c \leq \frac{2Re[\lambda_s]}{Re[\lambda_s]^2 + Im[\lambda_s]^2} = \Delta t_e \tag{4.22}$$

which is valid for positive $Re[\lambda_s]$. Note that the previous stability analysis was based on the application of the explicit formulation on the difference equation (4.11). Therefore, a larger time step Δt_c (greater than Δt_e in equation (4.22)) can be employed if an implicit formulation is used. This point is discussed in Chapter 5.

Equation (4.22) is employed as a guideline for the determination of Δt_c. To stabilize the system of equation (4.1), the following approach is established.

(i) Evaluate all Δt_e for which $Re[\lambda_s] > 0$ within the computational domain for each of the five species (i.e., for $s = 1, \ldots 5$).

(ii) Determine the minimum Δt_e among the different species at each node, i.e., $(\Delta t_e)_{\min}$

(iii) If $Re[\lambda_s] > 0$ for all the node points, then Δt_c should be selected smaller than $(\Delta t_e)_{\min}$ for explicit formulated finite difference equations. Otherwise, if an implicit formulation is employed, Δt_c can be greater than $(\Delta t_e)_{\min}$.

(iv) For node points at which $Re[\lambda_s] < 0$, select $\Delta t_c = \epsilon(\Delta t_e)_{\min}$, where $0 < \epsilon < 1$. The value of ϵ depends on the free stream conditions, including pressure and Mach number.

(v) If the computed Δt_c is greater than Δt_g (the time step used for gas dynamic equations), then Δt_c can be set to Δt_g.

4.3 Von Neumann Analysis for Two-Dimensional Chemistry Equations

In this section, the multi-dimensional chemistry equations are examined. To simplify the mathematical manipulation, two-dimensional governing equations in Cartesian coordinates are employed, and the results are then generalized to other multi-dimensional coordinates.

Recall that equation (3.33) for the two-dimensional species continuity equation (i.e., $\alpha = 0$) is

$$\frac{\partial Q_c}{\partial t_c} + \frac{\partial E_c}{\partial x} + \frac{\partial F_c}{\partial y} + W = 0 \tag{4.23}$$

The five decoupled species scalar equations may be expressed as:

$$\frac{\partial R_s}{\partial t_c} + u\frac{\partial R_s}{\partial x} + v\frac{\partial R_s}{\partial y} + d_s R_s = 0 \tag{4.24}$$

Equation (4.24) is then discretized explicitly using a forward difference approximation in time. In addition, parameters σ_x and σ_y are defined such that

$$\text{If} \quad u > 0\ , \quad \text{then} \quad \sigma_x = 1 \qquad \text{otherwise} \quad \sigma_x = 0$$

$$\text{If} \quad v > 0\ , \quad \text{then} \quad \sigma_y = 1 \qquad \text{otherwise} \quad \sigma_y = 0$$

Therefore, equation (4.24) is expressed in a finite difference form as:

$$\frac{R^{n+1}_{s(i,j)} - R^n_{s(i,j)}}{\Delta t_c} + u_{(i,j)} \left[\sigma_x \frac{R^n_{s(i,j)} - R^n_{s(i-1,j)}}{\Delta x} + (1 - \sigma_x) \frac{R^n_{s(i+1,j)} - R^n_{s(i,j)}}{\Delta x} \right]$$
$$+ v_{(i,j)} \left[\sigma_y \frac{R^n_{s(i,j)} - R^n_{s(i,j-1)}}{\Delta y} + (1 - \sigma_y) \frac{R^n_{s(i,j+1)} - R^n_{s(i,j)}}{\Delta y} \right]$$
$$+ d_{s(i,j)} R^n_{s(i,j)} = 0 \tag{4.25}$$

Again, all the R_s terms in equation (4.25) are replaced by the error ϵ in the von Neumann stability analysis as described in Section 4.2. However, for a two-dimensional problem, ϵ is expressed as

$$\epsilon_{(i,j)} = e^{at} e^{I(k_x i \Delta x + k_y j \Delta y)} \tag{4.26}$$

where

$$k_x = \frac{i\pi}{L_x} \tag{4.27}$$

$$k_y = \frac{j\pi}{L_y} \tag{4.28}$$

and L_x, L_y are dimensions of the computation domain in the x and y directions, respectively. Following the same procedures described in Section 4.2, the amplification factor is

$$G_{ex} = \left| e^{a\Delta t_c} \right| = \sqrt{(1 - Re[\lambda_s]\Delta t_c)^2 + (Im[\lambda_s] \cdot \Delta t_c)^2} \tag{4.29}$$

where

$$\begin{aligned}\lambda_s &= \frac{u}{\Delta x}\left[\sigma_x(1-e^{-I\theta_x})+(1-\sigma_x)(e^{I\theta_x}-1)\right]+\frac{v}{\Delta y}\left[\sigma_y(1-e^{-I\theta_y})\right.\\ &\quad \left.+(1-\sigma_y)(e^{I\theta_y}-1)\right]+d_s\\ &= \frac{u}{\Delta x}\left[(1-2\sigma_x)\cos\theta_x+I\sin\theta_x+(2\sigma_x-1)\right]+\\ &\quad \frac{v}{\Delta y}\left[(1-2\sigma_y)\cos\theta_y+I\sin\theta_y+(2\sigma_y-1)\right]+d_s \qquad (4.30)\end{aligned}$$

and

$$\begin{aligned}\theta_x &= k_x\Delta x\\ \theta_y &= k_y\Delta y\end{aligned}$$

Note that equation (4.29) has exactly the same form as equation (4.21). Therefore, the conclusion from the two-dimensional stability analysis is similar to that of the one-dimensional case described previously in Section 4.2. However, for the two-dimensional problems, the factorization scheme is used (as described in Chapters 2 and 3). Therefore, some basic assumptions must be satisfied in utilization of equation (4.29). These assumptions include:

$$d_s^2\Delta t_c^2 \ll 1$$

$$\left|\frac{uv}{\Delta x\Delta y}\right|\Delta t_c^2 \ll 1$$

$$\left|\frac{ud_s}{2\Delta x}\right|\Delta t_c^2 \ll 1$$

and

$$\left|\frac{vd_s}{2\Delta y}\right|\Delta t_c^2 \ll 1$$

These equations require that higher order terms $[O(\Delta t_c)^2]$ be small and hence they are neglected.

The governing equations are transformed into generalized coordinates as

$$\frac{\partial \bar{Q}_c}{\partial t_c} + \frac{\partial \bar{E}_c}{\partial \xi} + \frac{\partial \bar{F}_c}{\partial \eta} + \bar{W} = 0 \tag{4.31}$$

where

$$\begin{aligned} \bar{Q}_c &= Q_c/J \\ \bar{E}_c &= (E_c\xi_x + F_c\xi_y)/J \\ \bar{F}_c &= (E_c\eta_x + F_c\eta_y)/J \\ \bar{W} &= W/J \end{aligned}$$

The stability requirements of equation (4.31) will have the same form as equation (4.21) and equation (4.29), but with λ_s redefined as

$$\begin{aligned} \lambda_s = & \frac{U}{\Delta\xi}\left[(1-2\sigma_\xi)\cos\theta_\xi + I\sin\theta_\xi + (2\sigma_\xi - 1)\right] \\ & + \frac{V}{\Delta\eta}\left[(1-2\sigma_\eta)\cos\theta_\eta + I\sin\theta_\eta + (2\sigma_\eta - 1)\right] + d_s \end{aligned}$$

where

$$\begin{aligned} U &= u\xi_x + v\xi_y \\ V &= u\eta_x + v\eta_y \\ \theta_\xi &= k_\xi \Delta\xi \\ \theta_\eta &= k_\eta \Delta\eta \end{aligned}$$

and

$$
\begin{aligned}
k_\xi &= \frac{i\pi}{(IMM1)\Delta\xi} \\
k_\eta &= \frac{j\pi}{(JMM1)\Delta\eta} \\
\sigma_\xi &= 1 \quad \text{if} \quad U > 0\,, \ \text{otherwise,} \quad \sigma_\xi = 0 \\
\sigma_\xi &= 1 \quad \text{if} \quad V > 0\,, \ \text{otherwise,} \quad \sigma_\xi = 0
\end{aligned}
$$

Since the stability requirements of the two-dimensional problems are similar to those of the one-dimensional problems, the procedure described previously to determine Δt_c is extended to the two-dimensional problems.

Chapter 5

Numerical Results and Discussions

5.1 Introductory Remarks

In this chapter, the stability criterion for the time step Δt_c is investigated for the quasi one-dimensional nozzle flow as well as for the axisymmetric blunt body problem. Various free stream conditions (Mach number, pressure, temperature) are used to provide a detailed description on the finite rate chemistry effects. The results are compared with the solution obtained by the equilibrium chemistry model and the ideal gas model.

5.2 Quasi One-Dimensional Nozzle Flows

A diverging nozzle with cross-sectional area defined by

$$S(x) = 1.398 + 0.347 \tanh(0.8x - 4)$$

is used to specify the physical domain. For this investigation the nozzle entrance is located at $x = 1.2$ cm and the nozzle exit is at $x = 8.0$ cm. Twenty-one grid points are distributed uniformly along the nozzle as shown in Figure 5.1. The ratio of exit area to inlet area is 1.65.

To investigate the effects of high temperature chemistry, a normal shock is forced to be positioned at about $x = 4.0$ cm. Three different inlet Mach numbers (10, 15, and 20) along with the pressure and temperature are

used to specify the inlet flow at the nozzle entrance. Various values of pressures which correspond to eight altitudes (from 10 km to 80 km above the Earth's surface) are employed to cover the regions where chemistry effects are considered essential.

To investigate the effect of variation in pressure (or density), the temperature is set to a value of 230.44 K. Since the flow behind the normal shock will be subsonic, one physical boundary condition is required at the nozzle exit, as described in Chapter 2. For comparison of the post shock properties, the shock position in the nozzle is preferred to be at the same location for different air models (ideal gas, finite rate, equilibrium). Note that pressure is the only property that can be used for this purpose. The other properties (temperature, density, velocity) will have different values for different air models and it is difficult to predict their values in advance. The pressure ratios ($P_{\text{back}}/P_{\infty}$) used for the three Mach numbers are given in Table 5.1. The CFL number used for the gas dynamics time step (Δt_g) is based on a value of 2 for all cases. The solution obtained by the ideal gas model is employed as the initial solution for the finite-rate chemistry calculation. The chemistry time step (Δt_c) is determined from the initial solution by applying the method developed in Chapter 4. Tables 5.2, 5.3 and 5.4 show the minimum eigenvalues within the initial domain for conditions corresponding to altitudes of 10 to 80 Km at Mach numbers of 10, 15, and 20, respectively.

Note that for a Mach number of 10, all of the $Re[\lambda_s]_{\text{min}}$ are positive. As a result Δt_e, given by equation (4.22), can be used as Δt_c to provide a converged solution. However, at higher altitudes $\Delta t_e > \Delta t_g$; therefore, Δt_c is set to Δt_g. Furthermore, it is emphasized that Δt_e, given by equation (4.22) is

based on a more restrictive requirement of explicit treatment of $\dot{w}$ and convective terms. Therefore, a Δt_c which is larger than Δt_e (altitude $10 \sim 50$ Km) can indeed be used. Table 5.2 illustrates this statement.

At a higher Mach number of 15 and altitude range of $10 \sim 50$ Km, $Re[\lambda_s]_{\min} < 0$, suggesting a very stiff system. Thus, the procedure introduced in Chapter 4 is invoked to provide a converged solution. Typical values of ϵ are also included in Table 5.3. Note that at higher altitudes ($60 \sim 80$ Km), $Re[\lambda_s]_{\min} > 0$; and since $\Delta t_e > \Delta t_g$, Δt_c is set equal to Δt_g. At higher Mach numbers, the stiffness of system is magnified; and, at a Mach number of 20, $Re[\lambda_s]_{\min} < 0$ for altitudes of $10 \sim 60$ Km.

From Tables 5.2, 5.3, and 5.4 it may be concluded that, for a fixed Mach number, $Re[\lambda_s]_{\min} > 0$ will increase as pressure decreases (or, altitude increases). This in turn allows increasing the chemical time step Δt_c. Note that for a fixed pressure, lowering of Mach number has the same effect. These phenomena can be easily explained by physical considerations. A high free stream Mach number and pressure result in high values of pressure, temperature, and density behind the shock, which in turn provide a very large mass production rate, $\dot{w}$, when compared to the convective term. As a result, the equations become stiff, preventing the use of a large chemistry time step.

Figure 5-2 illustrates the comparison of temperature ratios of a normal shock obtained by the finite rate chemistry model to that of chemical equilibrium [45]. It is clear that for high pressures (low altitudes) where flow is in chemical equilibrium (since the chemical reaction rate is large), both models provide similar solutions. However, for lower pressures (high altitudes) where

flow is in chemical nonequilibrium (since the chemical reaction rate is low), use of an equilibrium chemistry model yields inaccurate solutions. From a physical point of view, note that as pressure decreases, it enhances the nonequilibrium effects.

Figure 5-3 represents the distribution of species mass-fraction along the nozzle corresponding to the inlet Mach number of 20 at an altitude of 30 Km. The solution obtained from the equilibrium model [51] is also provided. Note that the mass-fraction of nitrogen-oxide (NO) overshoots its equilibrium value immediately behind the shock. In the same position of the NO peak, the temperature curve also behaves in a similar manner (Figure 5-4a). This phenomenon is common to NO formation behind a shock [45] and can be explained as follows: The heat of formation of NO is smaller (by order of one) than that of nitrogen and oxygen; as a result, NO is the most sensitive of species to the temperature. Thus, when temperature overshoots (this phenomenon is characteristic of the nonequilibrium effect and is described in next figure), NO responds immediately.

Figure 5-4a illustrates the temperature distribution at Mach 20 for various altitudes. A temperature distribution computed based on an ideal gas model is also shown for comparison purposes. It is worth noting that the temperature at the exit plane (i.e., $x = 8$ cm) is decreasing with increasing altitude. This is a typical characteristic of chemically-reacting flows in the equilibrium regions [45] and a detailed discussion with mathematical verification is given in Appendix G.

Figure 5-4b represents the temperature distribution at Mach 20 at

higher altitudes (decreasing pressure). Note that the exit temperature is increasing as altitude is increasing (corresponding to pressure decreases). This is an expected phenomenon for nonequilibrium flows.

Also note that (from Figures 5-4a and 5-4b) for altitudes of higher than 30 Km, there is always a temperature peak just downstream of the shock. This indicates that nonequilibrium conditions exist in these regions, and, in fact, chemical equilibrium has not set in. Furthermore, the peak's wave length increases as a function of increase in altitude, indicating larger regions of nonequilibrium at higher altitudes.

Figures 5-5a and 5-5b show the temperature distributions at Mach 10 for various altitudes. Similar phenomena, as shown in the Mach 20 case (Figures 5-4a and 5-4b), are observed. In Figure 5-5a, however, the exit temperature starts to increase at 20 Km compared with 50 Km for the Mach 20 case. Based on the previous discussion related to Figure 5-4b, this indicates that the nonequilibrium behavior starts at a lower altitude for a "low" Mach number flow. In other words, at the same altitude, low Mach number flow is more chemically nonequilibrium than high Mach number flow. This behavior may be argued as follows: The Mach 20 flow has a higher chemical reaction rate (from higher temperature) but takes less time for reaction (since there is a higher velocity); however, the temperature effect is much more prominent than the velocity effect. Therefore, Mach 20 flow is more likely to attain a chemically equilibrium state than the Mach 10 flow.

Another interesting behavior observed in Figure 5-5b is the exit temperature, i.e., it does not change substantially between altitudes of 50 Km and

80 Km. This is also because the Mach 10 flow has a very low chemical reaction rate. Therefore, once the density value falls below a certain value, very little air dissociates. In fact, the flow is almost frozen (no dissociation) above 50 Km, so the temperature does not change with altitude at all.

Figures 5-6a and 5-6b represent the density ratio (ρ/ρ_∞) distributions at Mach 20 for different altitudes. Note that in the equilibrium region (from altitude 10 Km to 50 Km), the density ratio (exit value) increases with the increasing altitude; but in the nonequilibrium region (above 50 Km), it decreases with the increasing altitude. This behavior is in contrast to that of the temperature (recall Figures 5-4a and 5-4b). The reason for this is that the pressure distribution is somewhat unrelated to the chemistry effects; therefore, the density and temperature must behave in the opposite direction.

Figures 5-7a and 5-7b show the mass-fraction distributions of NO at Mach 20. Very similar behavior is observed in the temperature distributions (Figure 5-4a). However, note that in the nonequilibrium altitudes, the maximum of the NO curve shifts rapidly to the right as the altitude increases.

Figures 5-8 and 5-9 represent the mass-fraction distributions of O and N_2 at Mach 20, respectively. Both the equilibrium-altitude solutions of O (Figure 5-8a) and N_2 (Figure 5-9a) confirm the arguments described in Appendix G; the higher density (lower altitude), the less dissociation. As shown in Figures 5-8b and 5-9b, the equilibrium state is not attained at the nozzle exit, revealing the very strong nonequilibrium phenomenon for the high altitude flows.

Figures (5-10) and (5-11) represent the evolution history of $Re[\lambda_s]_{\min}$ for the Mach 10 and Mach 20 cases. The y axis is defined as $sgn(Re[\lambda_s]_{\min}) \cdot$

$\log_{10}(Re[\lambda_s]_{\min})$ to indicate both the sign and magnitude of $Re[\lambda]_{\min}$. Note that

$$sgn(Re[\lambda_s]_{\min}) = \frac{|Re[\lambda_s]_{\min}|}{Re[\lambda_s]_{\min}}$$

i.e., the sign of $Re[\lambda_s]_{\min}$.

The post-shock temperature evaluated by the ideal gas model is relatively low (about 4700 K) for the Mach 10 cases (Figure 5-10). Therefore, the chemical reaction rates are low and the species equations are not very stiff. As expected, computed values of $Re[\lambda_s]_{\min}$ are positive for both altitudes (20 Km and 70 Km).

For the Mach 20 flow (Figure 5-11), at an altitude of 20 Km, the high density and initial temperature (about 18000 K) generate a very large value of $\dot{w}$. Species equations become very stiff and $Re[\lambda_s]_{\min}$ retains negative values until the temperature is relaxed to a lower value. Initially very small Δt_c must be selected according to the procedures introduced in Chapter 4. As $Re[\lambda_s]_{\min}$ becomes positive, a larger Δt_c is then permitted to accelerate the convergence. At the altitude of 70 Km, the density is low. As a result, the species equations are not as stiff as at 20 Km. $Re[\lambda_s]_{\min}$ remains positive through all the iterations.

Figure 5-12 represents a typical convergence history for the sum of density, gas constant, and temperature for different chemical time steps used. The free stream Mach number was 20 and the pressure was set to correspond to 70 Km altitude.

5.3 Axisymmetric Blunt Body Problems

5.3.1 Investigation of the Euler Equations

The algorithm developed in Chapter 2 for the Euler equations is investigated initially by considering two applications. Subsequently, the effect of chemically reacting flows is considered.

The surface pressure distribution for a sphere/cone configuration is compared with experimental data [52] at the free stream Mach number of 10.6. Three different grid systems shown in Figure 5.13 with $42(\xi) \times 22(\eta)$ grid points are used to investigate the grid-sensitive nature of the Euler equations. Note that the grid points are clustered near the stagnation region, where the flow is expected to be subsonic, so as to satisfy the Courant number restriction [53]. Results obtained are virtually identical for all three grid systems. A typical pressure contour is shown in Figure 5.14. Good agreement of the surface pressure distribution between the numerical solution and experimental data is observed in Figure 5.15.

In the second example, as shown in Figures 5-16, 5-17, and 5-18, three different configurations represent the possible sequential ablated nosetip geometries of a hypervelocity projectile at low altitude [11]. Euler equations are solved with a $71(\xi) \times 55(\eta)$ grid system provided by an elliptic grid generator. The free stream Mach number was 18 for all configurations.

The pressure contour for configuration 3 is shown in Figure 5-19. Complex shock-shock interactions are revealed in the flare region. Since the drag acting on an axisymmetric body is represented by $D = \int P(2\pi y)dy$, the area under the curve in Figure 5-20 represents the (wave) drag force experi-

enced by that configuration. Pressure distributions evaluated based on modified Newtonian theory are also shown in Figure 5-20.

Note that the two different approaches give similar results in the nose-tip region; however, the modified Newtonian theory fails in the shock-shock interaction region and underpredicts pressure (drag) for configurations 2 and 3.

5.3.2 Nonequilibrium Chemistry Solutions of Axisymmetric Blunt Body Flow

In this section, an ellipsoid with major axis of 4.5 cm and minor axis of 3 cm is used at two altitudes (30 Km and 80 Km) and two free stream Mach numbers (12 and 18). Note that the solution of Euler equations with the ideal gas model is independent of the physical dimensions of the problem. This is due to the non-dimensionalization of equations; therefore, the solution depends on the free stream Mach number only. However, once the chemistry effects are incorporated, the solution becomes dimensional dependent.

Since the finite rate chemistry model is a very computer time-consuming method, a proper grid system (i.e., with suitable computation domain and number of grid points) is essential for the efficiency consideration. For a simple geometry such as an ellipsoid, a reasonable resolution of the shock layer takes about 10 to 20 grid points in the η direction.

To determine the computational domain, the following is observed. For a chemically reacting flow, the density ratio across a shock is always higher than the ideal gas flow. Thus, the shock stand-off distance of the former cannot

be larger than that of the latter. Therefore, the shock location obtained from the ideal gas model will provide a reasonable computational domain to be used for the finite rate chemistry calculation.

The Euler equations are solved for a 34 × 23 grid system (as shown in Figure 5-21) to determine the position of the ideal gas shock. Pressure, temperature, and Mach contours at a free stream Mach number of 18 are shown in Figures 5-22 through 5-24, respectively.

The position and shock structure at free stream Mach number 12 is basically the same as that of the Mach 18 case (from the high Mach number effect of ideal gas flow); therefore, only the solutions of the Mach 18 case are shown.

As described previously, the ideal gas shock is used to define a computational domain for the chemistry calculation. Figure 5-25 shows a 34 × 21 grid system generated for that purpose. Since it is not necessary to compute the whole domain of the body for the stability investigation, only a portion of the nose-tip is considered, i.e., only 26 × 21 grid points are used in the chemistry calculation. At least one-fourth of the computer time can be saved by doing this "computation domain economization". The reason is that the solution of the downstream region always converges much more slowly than that of the stagnation region. A detailed description of this phenomenon is left to Figures 5-34 through 5-36.

In the axisymmetric blunt body problems, the cold-start scheme described in Chapter 1 is employed for the initial solution. Ideal gas calculation is performed for a few iterations until a transient shock wave is formed before

the blunt body. The chemistry stability analysis described in Chapter 4 is then introduced to determine a suitable chemical time step Δt_c and the finite rate species equations are brought into the calculation by the loosely coupled scheme.

Table 5-5 shows the (initial) minimum eigenvalues and the corresponding gas dynamics and chemical time steps used at various free stream conditions. At 30 Km, the $Re[\lambda_s]_{\min}$ are negative for both Mach 12 and Mach 18 cases; thus, Δt_c is selected smaller than Δt_e. At 80 Km, the $Re[\lambda_s]_{\min}$ is negative for Mach 18, but its absolute value is small (order of 4) compared with that of the 30 Km case (order of 7). Therefore, the stiffness at 80 Km is much less than that at 30 Km. The chemical time steps (Δt_c) used in the 80 Km cases are greater than the gas dynamic time steps (Δt_g) for a faster convergence.

A rule of thumb in determination of Δt_c can be concluded from the results of quasi one-dimensional nozzle problems (Tables 5-2, 5-3, and 5-4) and axisymmetric blunt body problems (Table 5-5) as:

(I) For a system with positive eigenvalues ($Re[\lambda_s]_{\min} > 0$):

(i) $\Delta t_c \geq \Delta t_e$ for altitudes lower than 50 Km

(ii) $\Delta t_e > \Delta t_c \geq \Delta t_g$ for altitudes higher than 50 Km

(II) For a system with negative eigenvalues ($Re[\lambda_s]_{\min}) < 0$)

$$\Delta t_c = \epsilon \Delta t_e \quad ,$$

where

(i) $\epsilon \cong$ order of 10^{-1} for $\quad M_\infty \leq 15$

(ii) $\epsilon \cong$ order of 10^{-2} for $\quad M_\infty > 15$

Figure 5-26 shows the evolution of $Re[\lambda_s]_{\min}$ for the various free stream conditions. Similar behavior as that of the one-dimensional case (Figures 5-10 and 5-11) is observed.

Figure 5-27 illustrates the convergence history of temperature for the various free stream conditions. Obviously, the solution converges fastest for Mach 12 at an altitude of 80 Km, since the largest Δt_c is used. On the other hand, the solution for Mach 18 at an altitude of 30 Km converges slowest for the smallest Δt_c used. The y-axis is represented by

$$\frac{\sum_N \left| T^{n+1}_{(i,j)} - T^n_{(i,j)} \right|}{N}$$

where N is the number of grid points.

In the next few figures, a streamline coordinate is used to illustrate some results and comparisons. The stagnation point is defined as $S = 0$. Grid points on the stagnation streamline will have a negative value of S and $S > 0$ represents the grid point on the body surface as shown in Figure 5-28.

Figure 5-29 shows the effective $\gamma (= h/e)$ distributions along the stagnation line at different free stream conditions. Note that the flow with higher Mach numbers and lower altitudes will have the lower value of γ and smaller shock stand-off distance. A lower value of γ represents more dissociation of air and a higher density ratio (recall that $\gamma = h/e = (e + P/\rho)/e$ and pressure is usually not impacted by chemistry effects). For axisymmetric body flow, the

shock stand-off distance δ can be approximately evaluated by [10]

$$\delta = \frac{R \cdot (\rho_1/\rho_2)}{1 + \sqrt{2(\rho_1/\rho_2)}}$$

where R is the body radius, ρ_1 is the free stream density, and ρ_2 is the post-shock density. Therefore, a high density ratio (ρ_2/ρ_1) means small value of δ.

Figures 5-30 through 5-32 represent the temperature, density and pressure distributions along the stagnation streamline at Mach 18, and 30 Km altitude. Ideal gas solutions along with the equilibrium chemistry solutions [54] (behind a normal shock) are also included for comparison. Good agreement of the different solutions from the two chemistry models is observed.

A temperature nonequilibrium region (peak behind shock wave) is also observed in Figure 5-30. From Figure 5-32, it can be concluded that the variation in pressure at the stagnation point is about 4% between the ideal gas solution and the finite rate chemistry solution.

Figure 5-33 illustrates the species mass-fraction distributions along the stagnation streamline at Mach 18, 30 Km. Equilibrium solutions are also shown for comparison [51]. Similar phenomena were observed in the nozzle problem (Figure 5-3), i.e., the equilibrium model underpredicts the mass-fraction of the nitrogen atom, and an overshoot region of the nitro-oxide behind the shock.

Figures 5-34 through 5-36 show the transient and converged solutions of temperature, N (nitrogen) and NO distributions along streamline S at Mach 18, 30 Km. These figures indicate that the solution always converges

first in the stagnation region rather than the downstream region. The reason is that there are more grid points positioned in the stagnation region; hence, higher accuracy and faster convergence is achieved in this region. Figure 5-35 shows that most dissociation of N_2 occurs at the stagnation region because the temperature is highest in this region. However, it is interesting to note that there are two intense regions of NO distributions shown in Figure 5-36. The first one, located at the stagnation region, represents the nonequilibrium effect as described previously. The second region, also predicted by the equilibrium solution [49], is located in the downstream region.

Figure 5-37 represents a typical convergence history of the species mass-fraction. The y-axis is defined by

$$\log_{10}\left(\frac{\sum_{N}\sum_{S=1}^{5}\left|C^{n+1}_{s_{(i,j)}}-C^{n}_{s_{(i,j)}}\right|}{N}\right)$$

where N is the number of grid points. As shown in this figure, the convergence is extremely slow as the iteration number is increased to 2000.

Figure 5-38 illustrates the temperature distributions along the stagnation streamline at Mach 12, 30 Km. A visible difference between the solution of the finite rate model and the equilibrium model is shown at the stagnation point. Compared with Figure 5-30, it is clear that the equilibrium model is more applicable for "high" Mach number flows than for "low" Mach number flows. Because the "low" Mach number flow is more likely to be "frozen" than the "high" Mach number flow, the finite rate chemistry formulation is more suitable for it. Figure 5-39 shows the corresponding species mass-fraction distributions along the stagnation streamline. Note that all the different species

change their values gradually toward the stagnation point. This phenomenon indicates a strong finite rate (nonequilibrium) behavior. Also, note that at the stagnation point NO has a much higher value than that of the Mach 18 case (Figure 5-33).

Figures 5-40 and 5-41 represent the temperature distributions along the stagnation streamline for Mach 18 and 12 at 80 Km. The corresponding species mass-fraction distributions are shown in Figures 5-42 and 5-43. Obviously, the equilibrium chemistry model gives unacceptable temperature values, with the error even greater than that of the ideal gas solution. Very little dissociation occurs in the Mach 18 case (Figure 5-42) and no visible dissociation is observed in the Mach 12 case (Figure 5-43). Therefore, it is clear that fluid behaves as a "frozen flow" at this high altitude. As a result, the equilibrium model cannot be employed to achieve a reasonable solution.

Because all of the different free stream conditions, pressure, and density contours were similar to each other, only the solutions at Mach 18, 30 Km are presented in Figure 5-44 (pressure contours) and Figure 5-45 (density contours). Figures 5-46 through 5-49 are the temperature contours corresponding to various free stream conditions. Note that the spike-like contours just behind the shock wave shown in Figure 5-46 (Mach 18, 30 Km), represent the local nonequilibrium regions (recall the peak shown in Figure 5-30) within the shock layer. The same phenomenon is also observed in the Mach 12 case (Figure 5-47), but is not as prominent as in Figure 5-46. As the altitude is increased to 80 Km, the flow behaves more like a frozen flow (recall Figures 5-42 and 5-43); therefore, the temperature contours shown in Figures 5-48 and 5-49 are similar to that of the ideal gas solution (Figure 5-23).

Figure 5-50 shows the mass-fraction contours of N at 30 Km for Mach 18. Note that no (or very little) N appears in the downstream region. However, this does not mean that no N_2 dissociates. The dissociated N_2 goes to the formation of NO, as shown in Figure 5-51.

Figures 5-52 through 5-54 are the mass-fraction contours of O at various free stream conditions. For the Mach 18, 30 Km case, most oxygen molecules are dissociated within a short region behind the shock wave, as shown in Figure 5-52. Note that in the other cases (Figures 5-53 and 5-54), contours of O show a parallel layer-like structure. This indicates that O_2 dissociates gradually as the fluid is moving through the shock layer. However, further dissociation does not occur as it expands toward the downstream region. In other words, fluid behaves strongly as a nonequilibrium flow (almost frozen), as shown in Figures 5-53 and 5-54.

Finally, a comparison of numerical solution (both ideal gas model and finite rate chemistry) and experimental data [55] of the shock detachment distance for a sphere is shown in Figure 5-55. The diameter of the sphere is 1/2 inch and the free stream conditions are specified as $M_\infty = 15.3$, $P_\infty = 664$ Pa and $T_\infty = 293$ K. A 31 $\times$ 21 grid system shown in Figure 5-56 is used for the computation. The temperature contours (chemistry solution) are shown in Figure 5-57. From Figure 5-55, it is obvious that the finite rate chemistry model predicts the shock wave structure accurately.

Chapter 6

Summary and Conclusions

In the present investigation, the stability of the nonequilibrium chemistry equations is investigated by using the von Neumann stability analysis. A scheme that predicts the marching time step for a converging solution is developed. This scheme is validated by numerical simulation of both the quasi one-dimensional nozzle problem and the 2D/axisymmetric blunt body problem. Various free stream conditions are employed for a detailed investigation. Euler equations, as well as the chemistry species equations, are discretized by an implicit, flux-splitting finite difference formulation. The loosely coupled scheme is adopted for communication between the gas dynamic equations and chemistry equations.

The algorithm developed for the Euler equation was validated by comparison of the 2D/axisymmetric (ideal gas) solution with experimental data and modified Newtonian solution. Solution of the nonequilibrium chemistry model was compared with the solution of the ideal gas model as well as the equilibrium chemistry model. From the results of this investigation, the following are concluded:

(1) The stiffness of the chemistry equation is induced from the highly nonlinear mass production rate terms. The eigenvalues (λ_s) of the chemistry

equation indicate the degree of this stiffness. For low altitude (high density) problems, the (absolute) value of λ_s is very large, dictating the specification of smaller marching time step.

The cause of this high value of λ_s is the high eigenvalue d_s of the mass production rate matrix. Therefore, the stability is dominated by the chemistry term rather than the convective term. In contrast to the low altitude problem, at high altitude (low density), the stability is more likely to be dominated by the convective term, and a large marching time step can be employed for the chemistry equations. Usually, at low altitude, the chemistry marching time step (Δt_c) used for a converged solution is smaller than the marching time step (Δt_g) of gas dynamic equations. At high altitude, the situation is reversed.

(2) If the eigenvalue $(\lambda_s)_{\min}$ of the system is positive, an explicitly formulated time step Δt_e can be used as a guideline for selection of Δt_c. A value of Δt_c larger than Δt_e is possible for an implicit-formulated difference equation. On the other hand, if $(\lambda_s)_{\min}$ has a negative value, then Δt_c should be selected smaller than Δt_e for a converging solution. From the numerical experiments, a rule of thumb is to set Δt_c as $\epsilon \Delta t_e$, where

   (i) ϵ is in the order of 10^{-1} for free stream Mach number less than 15.

   (ii) ϵ is in the order of 10^{-2} for free stream Mach number greater than 15.

(3) In the equilibrium region, high pressure has an effect of prohibition of air dissociation; therefore, temperature in the shock layer decreases as the

altitude increases (pressure decreases). In the nonequilibrium region, the situation is reversed. As the altitude increases, fluid behaves more as a "frozen flow" instead of an "equilibrium flow". However, the transition altitude (from "equilibrium region" to "nonequilibrium region") depends on the free stream Mach number. For Mach 20 flow, it is at about 50 Km, but for Mach 10 flow, it is at about 20 Km. Therefore, for "low" Mach number flows, the finite-rate chemistry model should be used even at low altitude problems.

(4) Even in equilibrium regions, sometimes the nonequilibrium behavior is indicated in a small region behind the shock wave. If the characteristic length of the hypervelocity vehicle is relatively small, then the nonequilibrium effect will be important and the finite-rate model must be employed to include this phenomenon.

(5) Inclusion of the chemistry effects for hypersonic flow field calculation results in higher density ratio, lower temperature, and smaller shock standoff distance (compared with ideal gas model). However, its effect on the surface pressure, as might be expected, is minimum.

Tables

	INFLOW		OUTFLOW	
	Subsonic	Supersonic	Subsonic	Supersonic
Number of B.C. to be specified (Analytical B.C.)	2	3	1	0
Number of B.C. by extra-polation (Numerical B.C.)	1	0	2	3
	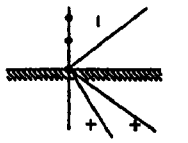	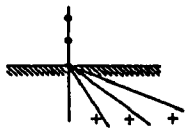	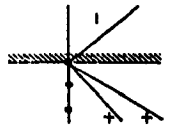	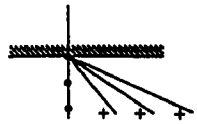

Table 2-1. Inflow and Outflow Boundary Conditions.

Gas	T_c (K)	P_c (atm)
H_e	5.3	2.26
H_2	33.3	12.8
N_2	126.1	33.5
O_2	154.4	49.7

Table 3-1: Critical Temperature and Critical Pressure for Different Gases

s subscript	1	2	3	4	5	(units)
reactant	O_2	N_2	NO	O	N	
M_s	32	28	30	16	14	g/mole
$h_{o,s}$	0	0	2.995E10	1.544E11	3.364E11	erg/g
θ_s	2275.2	3394.4	2740.7			K

$R_u = 8.3143E7$ erg/(g·mole·K)

Table 3-2: Molecular Weight, Heat of Formation and Characteristic Temperature for the 5 Species Model Used.

Inlet Mach Number	10	15	20
Pressure Ratio (P_b/P_∞)	98.38	225.13	429.46

Table 5-1: Pressure Ratios Used for the Nozzle Problem

$M_\infty = 10$					
Δt_g = 0.22368E-5 (CFL = 2)					
Alt(Km)	p_∞ (Dyne/cm^2)	$Re(d)_{\min}$	$Re(\lambda)_{\min}$	Δt_e	(Δt_c)
10	2.65 E5	−.273E5	.2 E6	.257E-8	.447E-7
20	5.529E4	−.562E4	.218E6	.123E-7	0.223E-6
30	1.197E4	−.123E4	.222E6	.539E-7	.112E-5
40	2.87 E3	−.289E3	.223E6	.237E-6	.224E-5*
50	7.98 E2	−.811E2	.223E6	.854E-6	.224E-5*
60	2.25 E2	−.228E2	.223E6	.303E-5	.224E-5*
70	5.52 E1	−.561E1	.223E6	.123E-5	.224E-5*
80	1.04 E1	−.113E1	.223E6	.610E-4	.224E-5*

* Δt_g is used.

Table 5-2: Minimum Eigenvalues and the Corresponding Gas Dynamics and Chemical Time Steps for $M = 10$

$M_\infty = 15$						
Δt_g = 0.149E-5 (CFL = 2)						
Alt(Km)	p_∞ (Dyne/cm^2)	$Re(d)_{\min}$	$Re(\lambda)_{\min}$	Δt_e	(Δt_c)	ϵ
10	2.65 E5	−0.209E9	−0.209E9	0.425E-8	0.746E-9	0.18
20	5.529E4	−0.441E8	−0.437E8	0.204E-7	0.149E-8	0.073
30	1.197E4	−0.948E7	−0.915E7	0.943E-7	0.149E-7	0.16
40	2.87 E3	−0.226E7	−0.193E7	0.392E-6	0.745E-7	0.19
50	7.98 E2	−0.632E6	−0.300E6	0.141E-5	0.373E-6	0.26
60	2.25 E2	−0.177E6	0.154E6	0.501E-5	0.149E-5*	—
70	5.52 E1	−0.434E5	0.279E6	0.204E-4	0.149E-5*	—
80	1.04 E1	−0.876E4	0.228E6	0.102E-3	0.149E-5*	—

* Δt_g is used.

Table 5-3: Minimum Eigenvalues and the Corresponding Gas Dynamics and Chemical Time Steps for $M = 15$

$M_\infty = 20$						
Δt_g = 0.112E-5 (CFL = 2)						
Alt(Km)	p_∞ (Dyne/cm^2)	$Re(d)_{min}$	$Re(\lambda)_{min}$	Δt_e	(Δt_c)	ϵ
10	2.65 E5	−0.896E9	−0.895E9	0.124E-8	0.279E-10	0.0225
20	5.529E4	−0.186E9	−0.185E9	0.600E-8	0.112E- 9	0.0186
30	1.197E4	−0.404E8	−0.400E8	0.276E-7	0.558E- 9	0.0202
40	2.87 E3	−0.964E7	−0.923E7	0.116E-6	0.279E- 8	0.024
50	7.98 E2	−0.270E7	−0.229E7	0.413E-6	0.279E- 7	0.068
60	2.25 E2	−0.760E6	−0.350E6	0.147E-5	0.279E- 6	0.189
70	5.52 E1	−0.186E6	0.215E6	0.598E-5	0.112E- 5*	—
80	1.04 E1	−0.349E5	0.356E6	0.319E-4	0.112E- 5*	—

* Δt_g is used.

Table 5-4: Minimum Eigenvalues and the Corresponding Gas Dynamics and Chemical Time Steps for $M = 20$

Alt(Km)	p_∞ (Dyne/cm^2)	$T_\infty(K)$	Mach	CFL	Δt_g	$Re(d_s)_{\min}$	$Re(\lambda_s)_{\min}$	Δt_e	Δt_c	ϵ
30	1.197E4	226.5	12	0.5	1.58E-6	−1.11E6	−1.03E6	6.87E-6	7.89E-7	0.115
			18	0.4	8.64E-7	−1.53E7	−1.51E7	6.79E-6	5.4 E-8	0.008
80	1.04E1	180.6	12	1.0	3.48E-6	−1.14	6.76E4	6.49E-3	3.48E-5	—
			18	0.5	1.24E-6	−1.70E4	−1.35E4	4.74E-3	2.48E-6	—

Table 5-5: Minimum Eigenvalues and the Corresponding Gas Dynamics and Chemical Time Steps for 2D Axisymmetric Blunt Body.

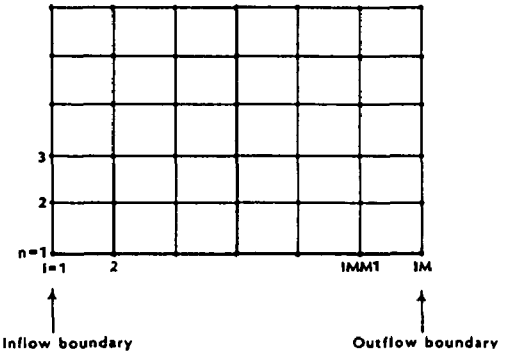

Figure 2-1. The Computational Domain Used for the Solution of Equation (2-30).

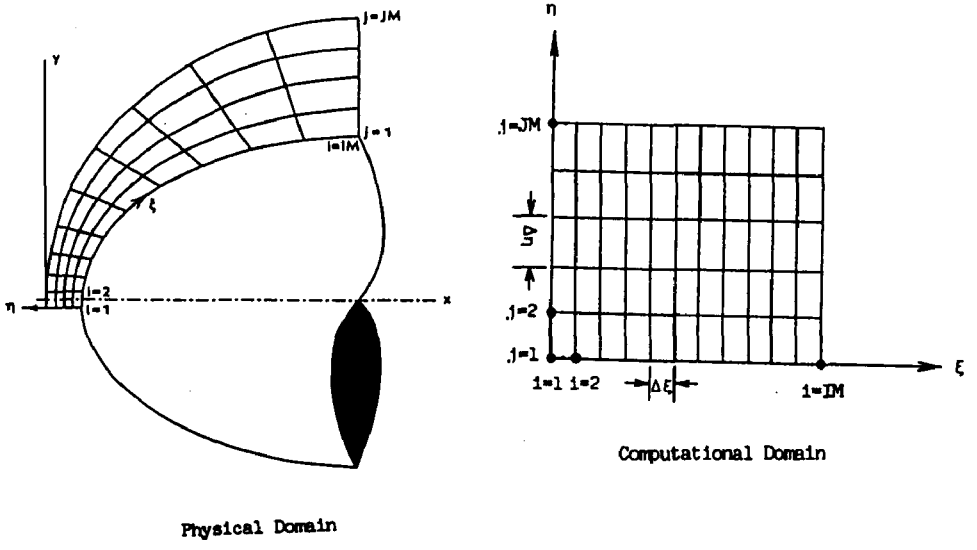

Figure 2-2. Generalized Coordinate Transformation.

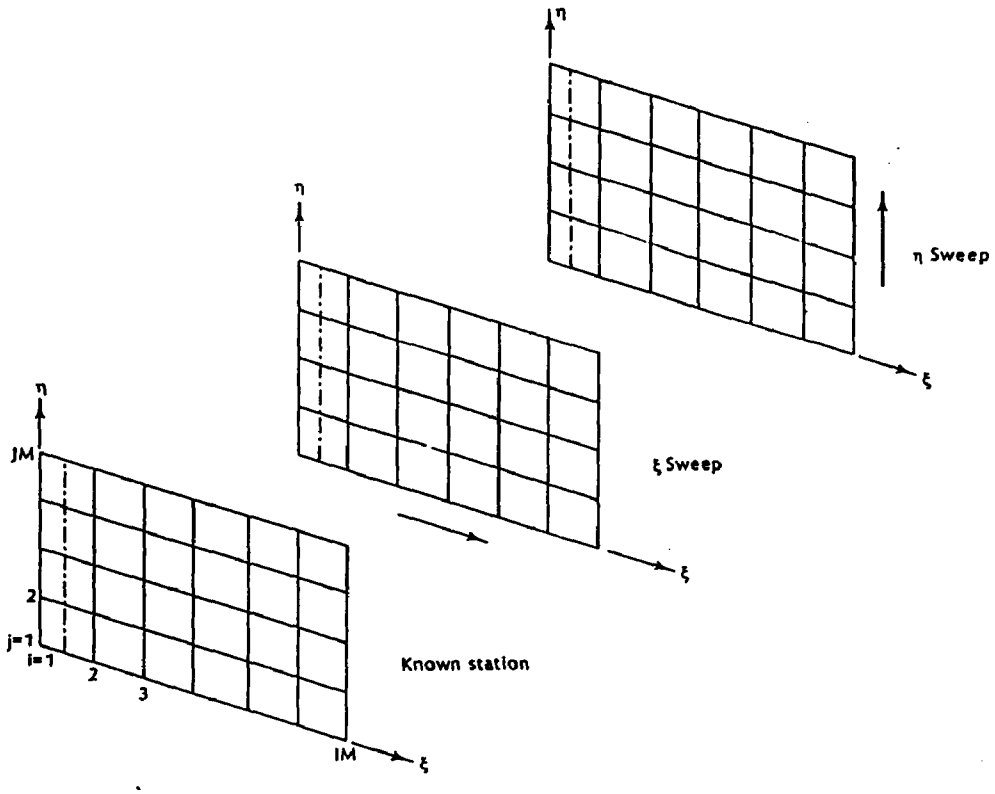

Figure 2-3. The Finite Difference Equations (2-75) and (2-76) Are Solved Sequentially by ξ and η Sweeps.

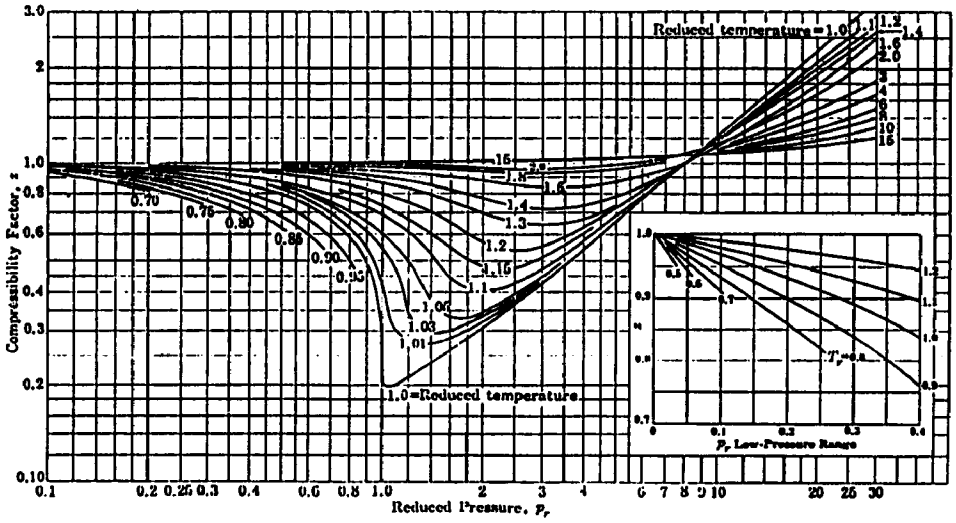

Figure 3-1. The Compressibility Factor as a Function of the Reduced Pressure and Reduced Temperature.

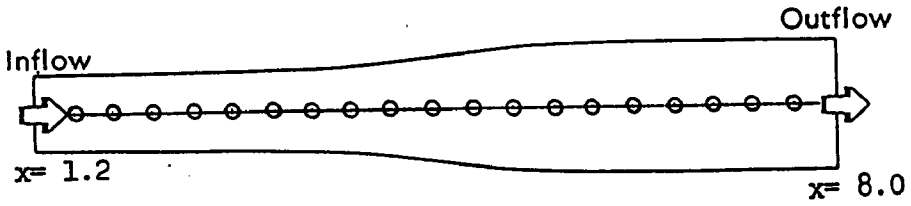

Figure 5-1. The Diverging Nozzle and Grid Points Distribution.

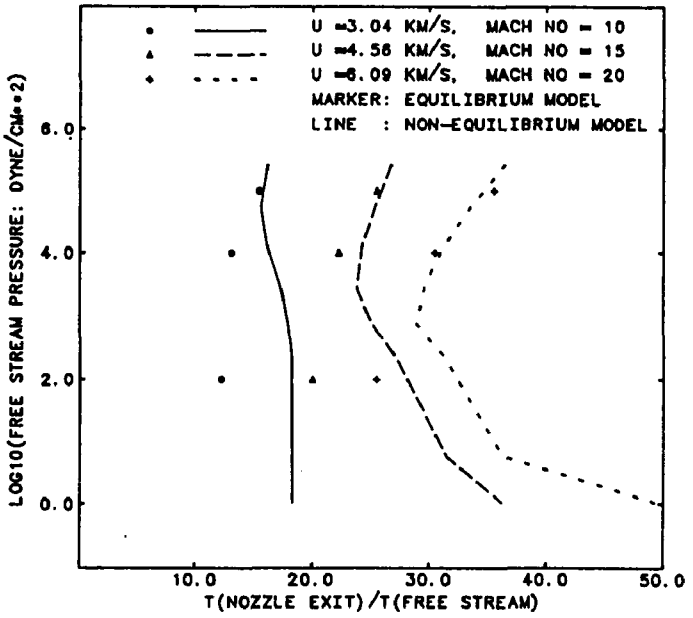

Figure 5-2. Comparison of the Temperature Ratios for a Normal Shock by Different Chemistry Models.

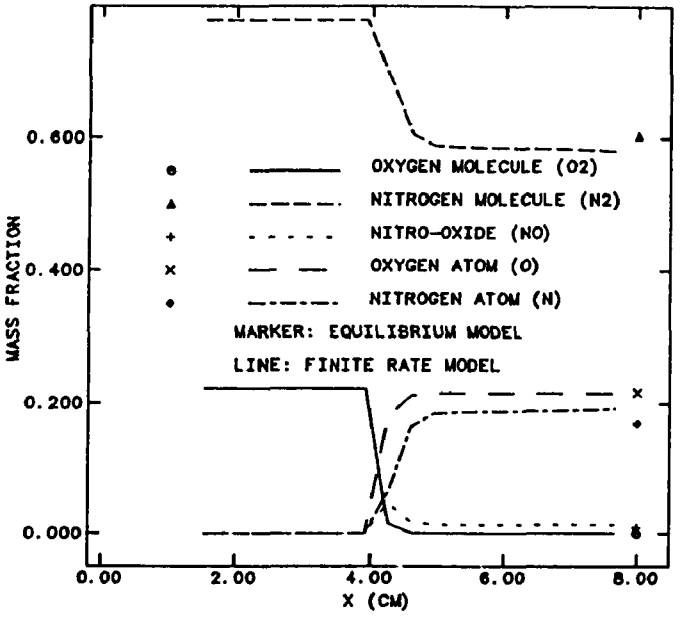

Figure 5-3. Species Mass-Fraction Distributions Along the Nozzle at Mach 20, 30 km.

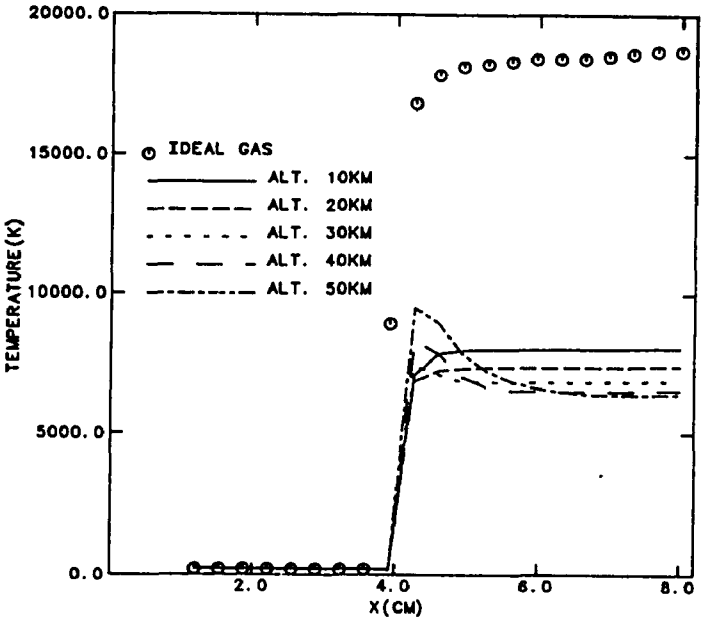

Figure 5-4a. Comparison of the Temperature Distributions for Mach 20 Flow at Various Altitudes.

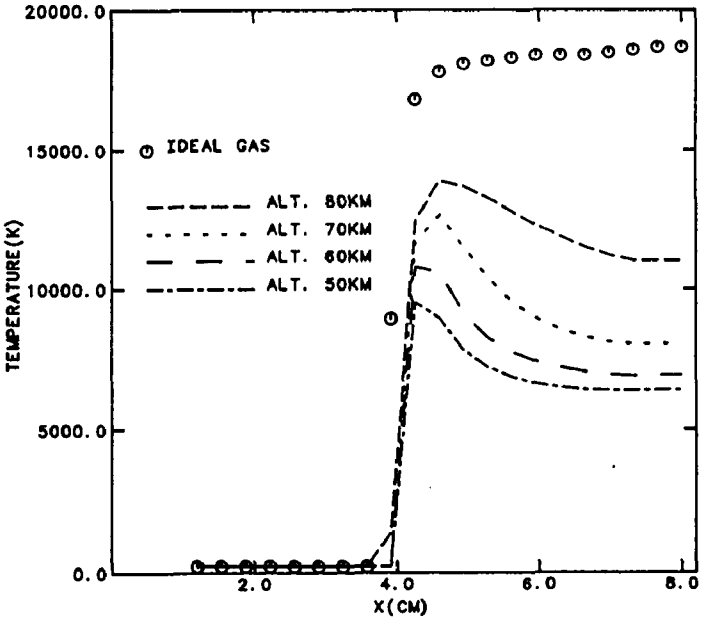

Figure 5-4b. Comparison of the Temperature Distributions for Mach 20 Flow at Various Altitudes.

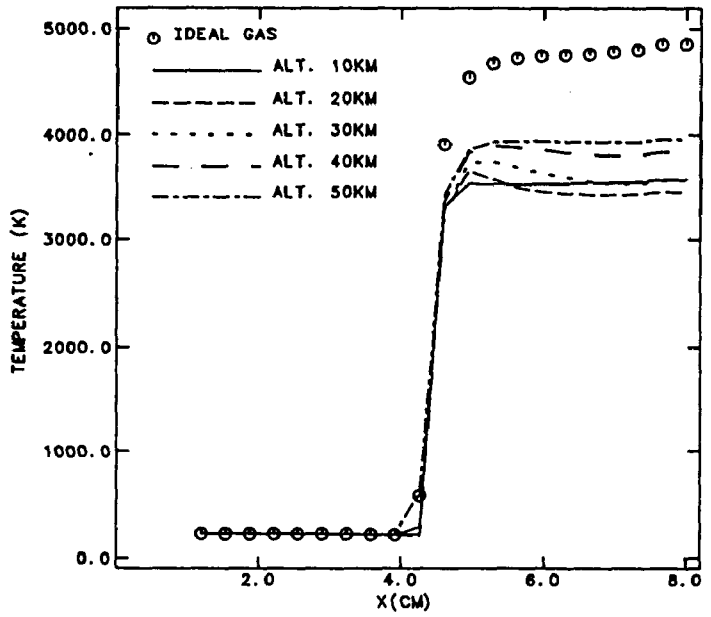

Figure 5-5a. Comparison of the Temperature Distributions for Mach 10 Flow at Various Altitudes.

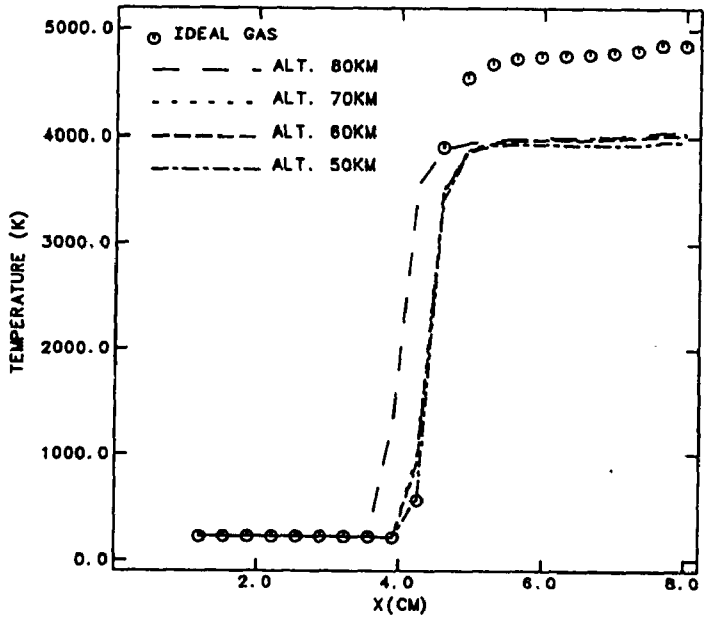

Figure 5-5b. Comparison of the Temperature Distributions for Mach 10 Flow at Various Altitudes.

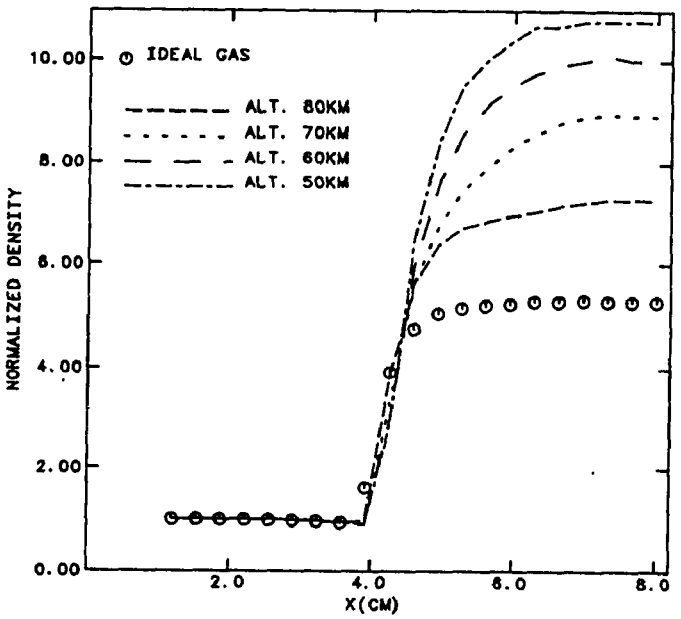

Figure 5-6a. Comparison of the Density Distributions for Mach 20 Flow at Various Altitudes.

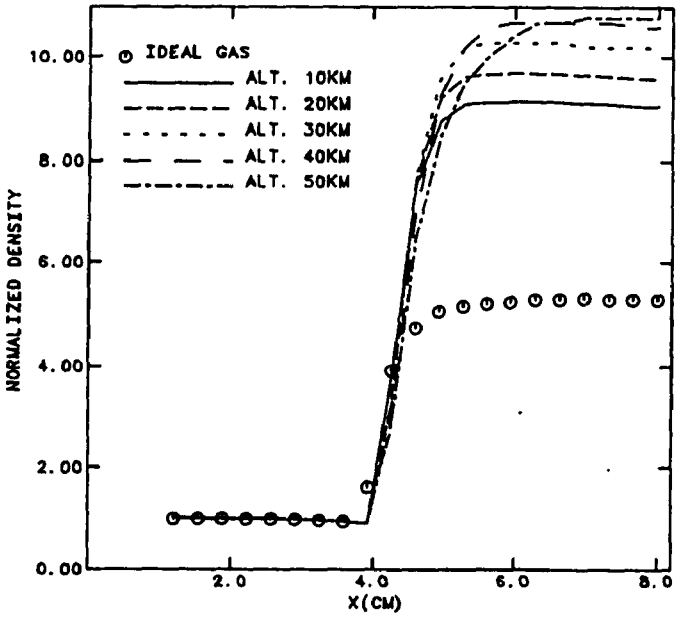

Figure 5-6b. Comparison of the Density Distributions for Mach 20 Flow at Various Altitudes.

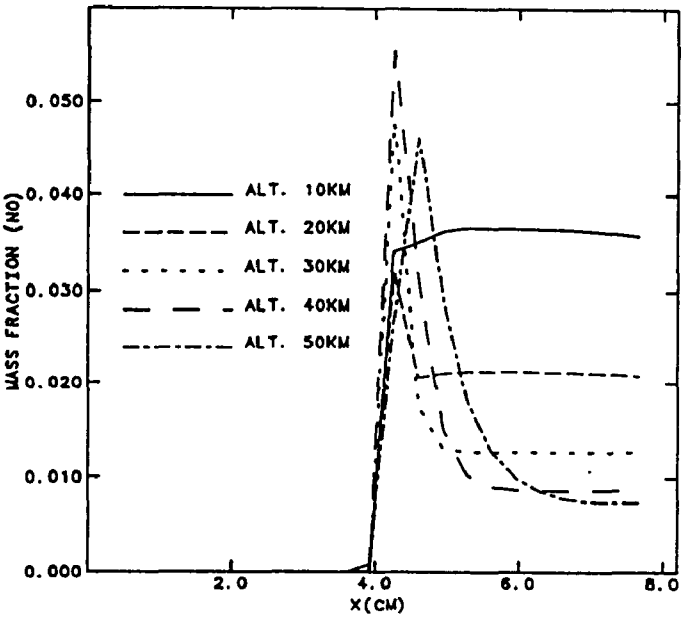

Figure 5-7a. Comparison of the Mass-Fraction of *NO* Distributions for Mach 20 Flow at Various Altitudes.

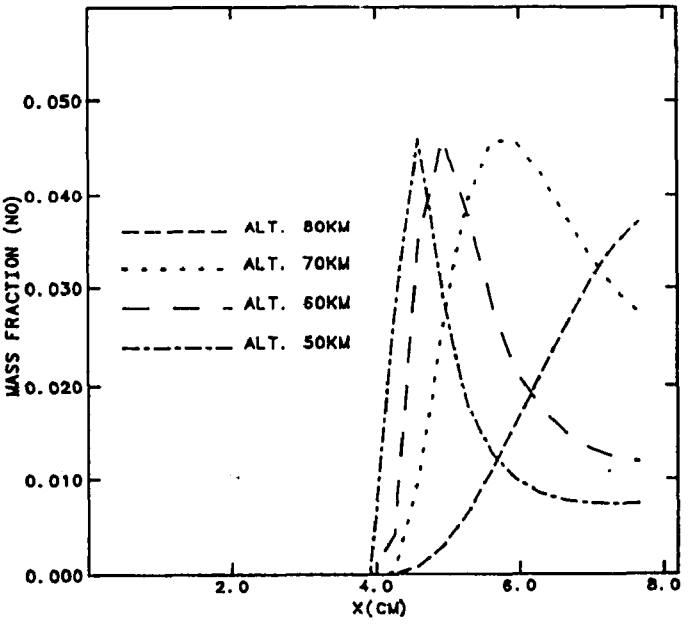

Figure 5-7b. Comparison of the Mass-Fraction of *NO* Distributions for Mach 20 Flow at Various Altitudes.

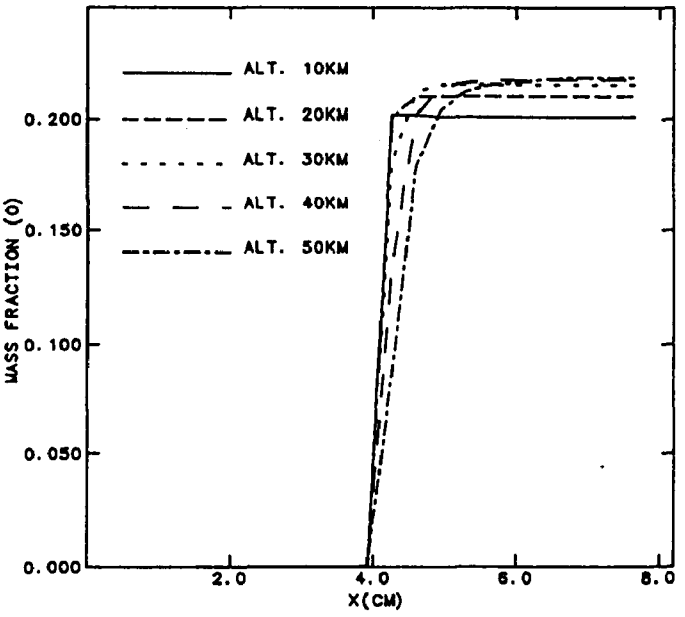

Figure 5-8a. Comparison of the Mass-Fraction of O Distributions for Mach 20 Flow at Various Altitudes.

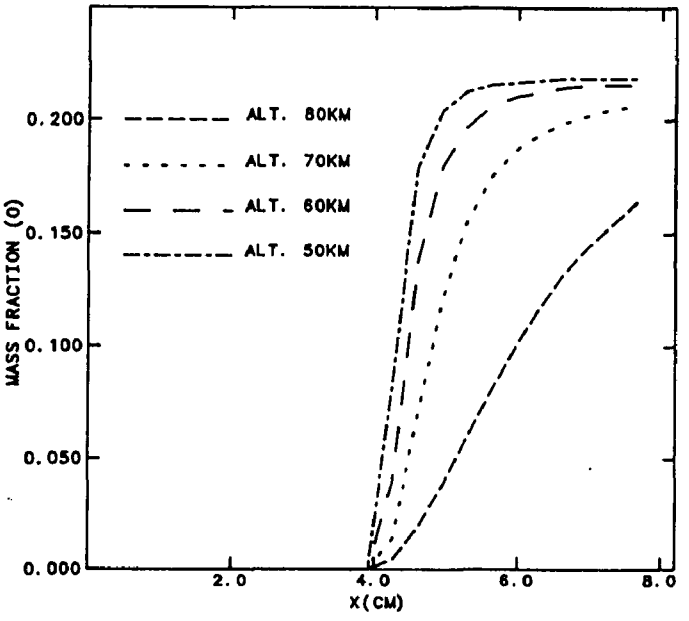

Figure 5-8b. Comparison of the Mass-Fraction of O Distributions for Mach 20 Flow at Various Altitudes.

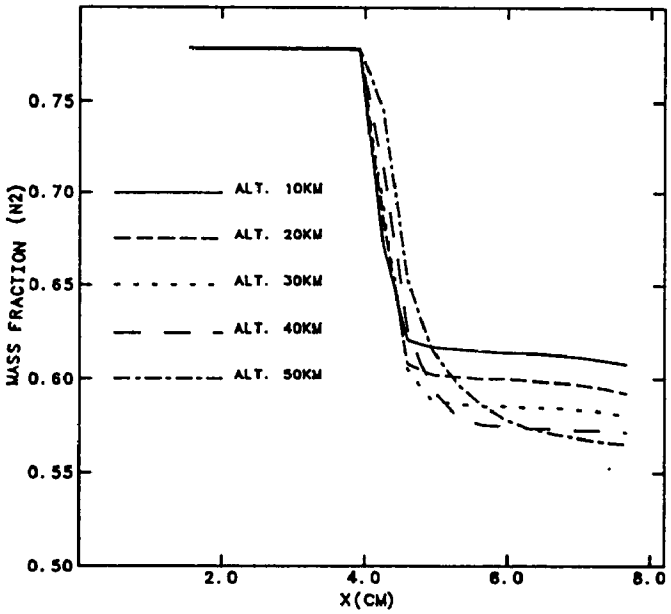

Figure 5-9a. Comparison of the Mass-Fraction of N_2 Distributions for Mach 20 Flow at Various Altitudes.

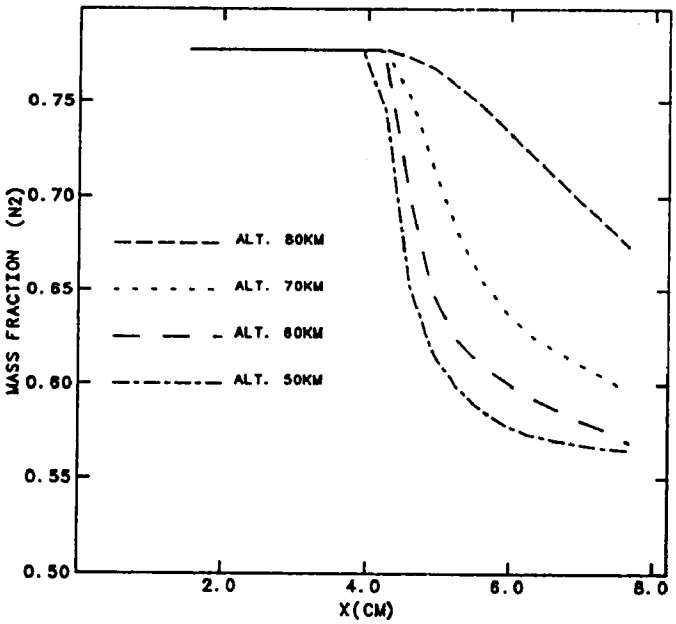

Figure 5-9b. Comparison of the Mass-Fraction of N_2 Distributions for Mach 20 Flow at Various Altitudes.

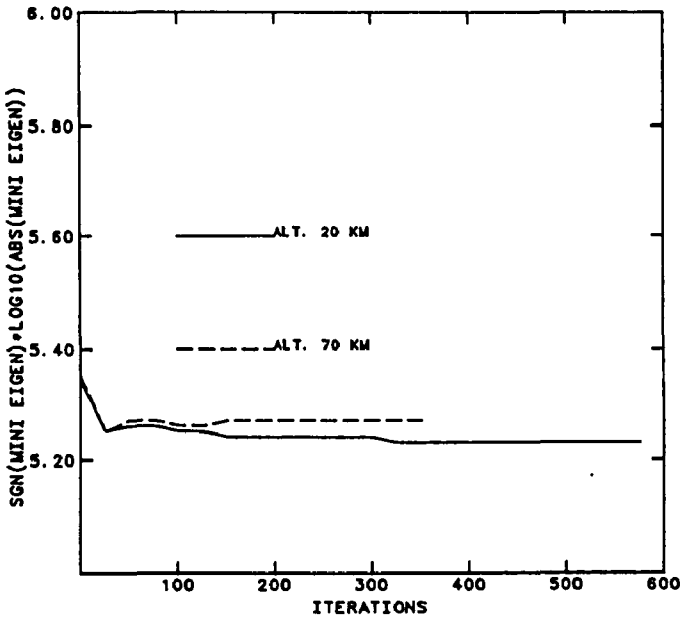

Figure 5-10. Evolution of $Re[\lambda s]$ min for Nozzle Flow Problem at Mach 10.

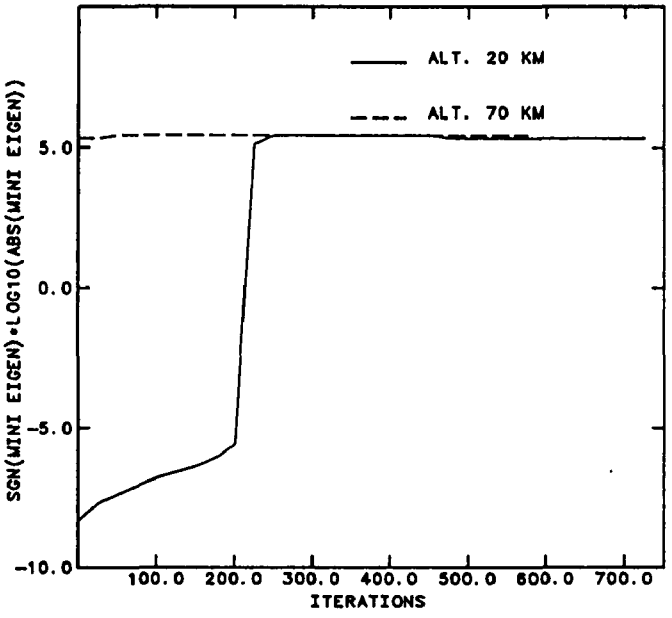

Figure 5-11. Evolution of $Re[\lambda s]$ min for Nozzle Flow Problem at Mach 20.

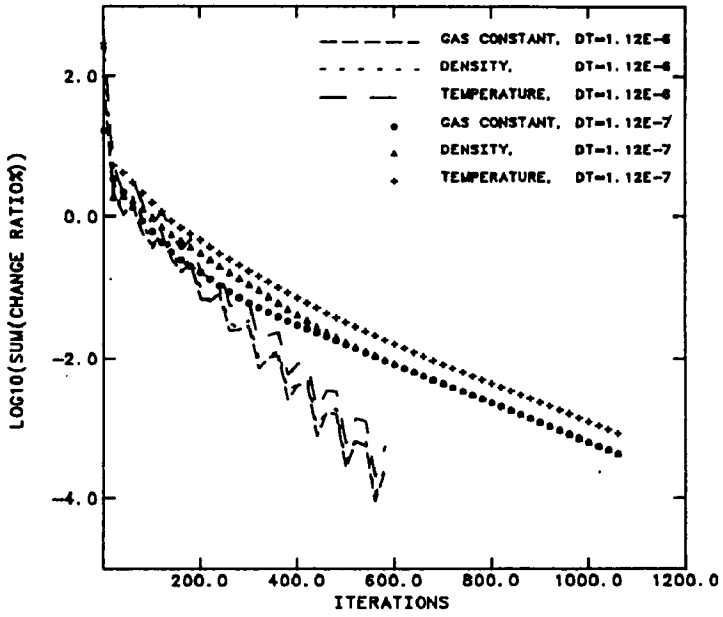

Figure 5-12. Convergence History for Mach 20 Flow at Altitude of 70 km.

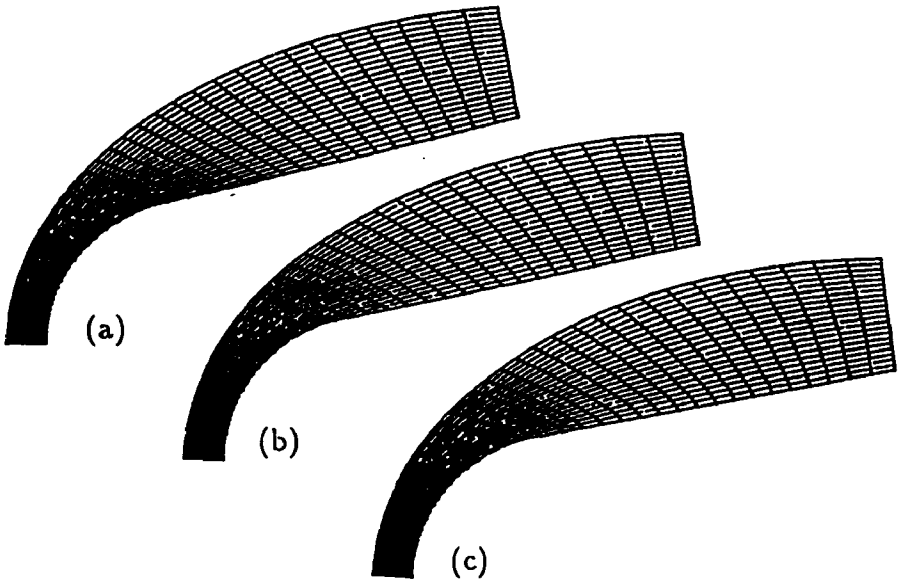

Figure 5-13. Sphere/Cone Configuration with (a) Algebraic Grid, (b) Elliptic Grid, and (c) Surface Normal.

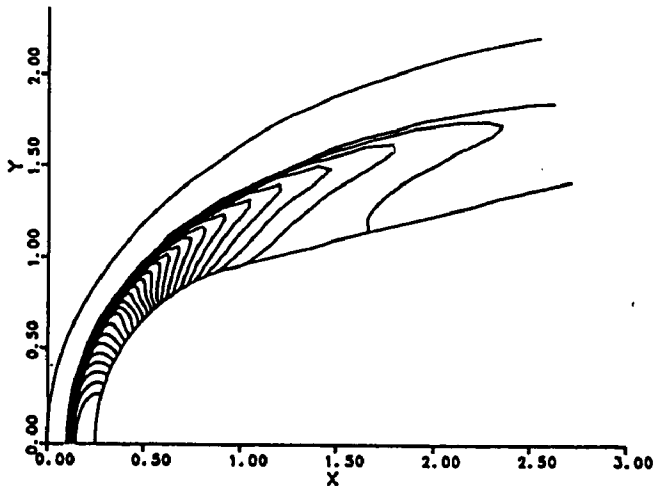

Figure 5-14. Pressure Contours for the Sphere/Cone Configuration.

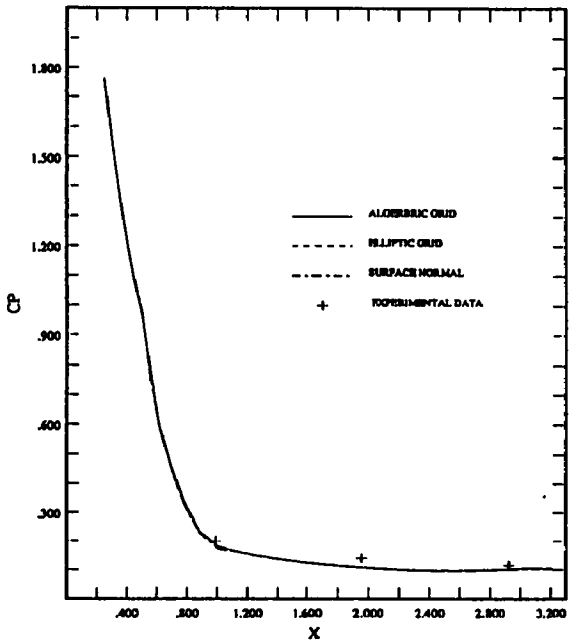

Figure 5-15. Comparison of Surface Pressure Distributions for the Sphere/Cone Configuration at Mach Number 10.6.

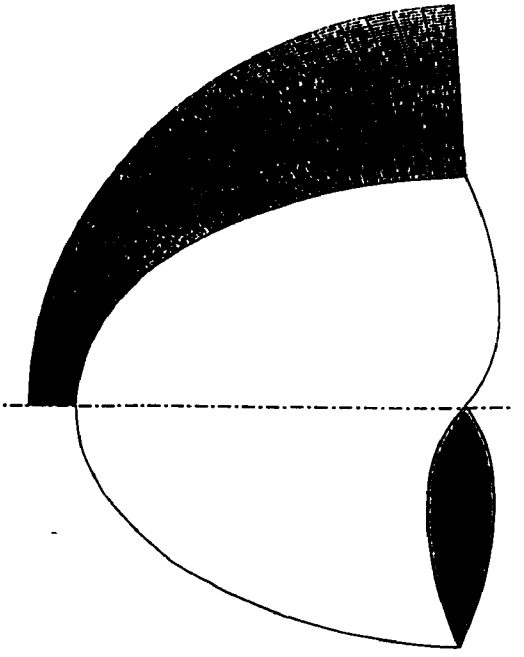

Figure 5-16. The Grid System for Configuration 1.

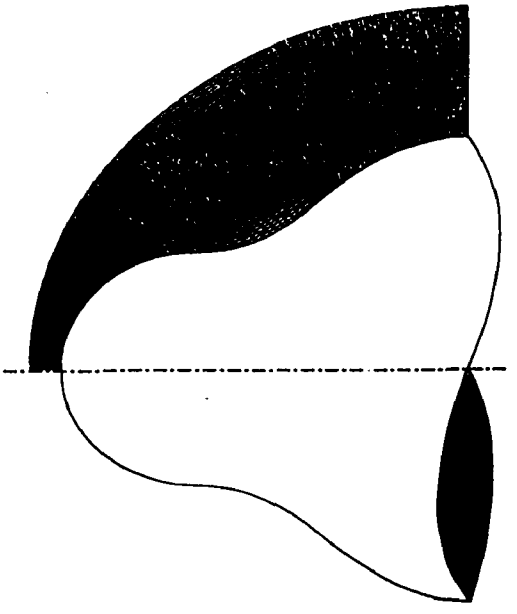

Figure 5-17. The Grid System for Configuration 2.

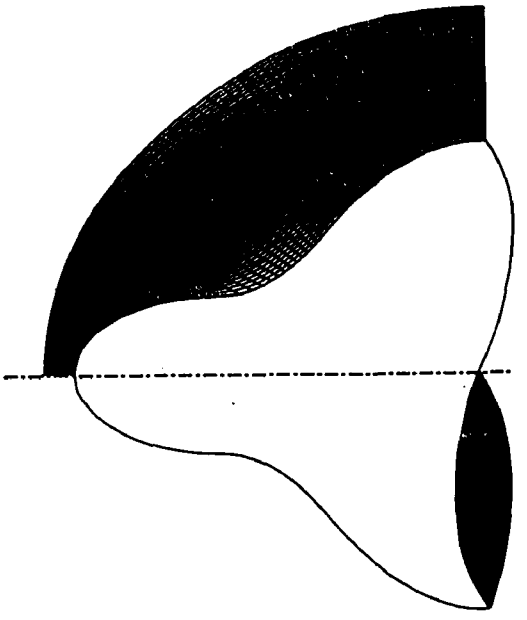

Figure 5-18. The Grid System for Configuration 3.

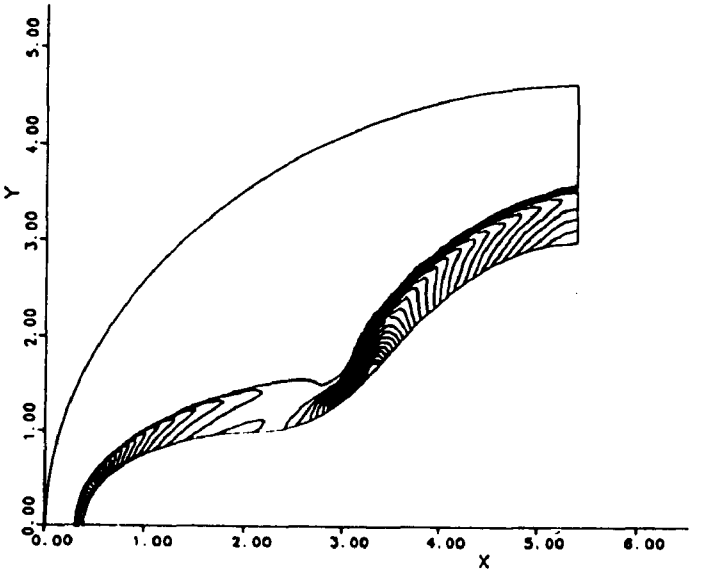

Figure 5-19. Isobars for Configuration 3 at Free-Stream Mach Number of 18.

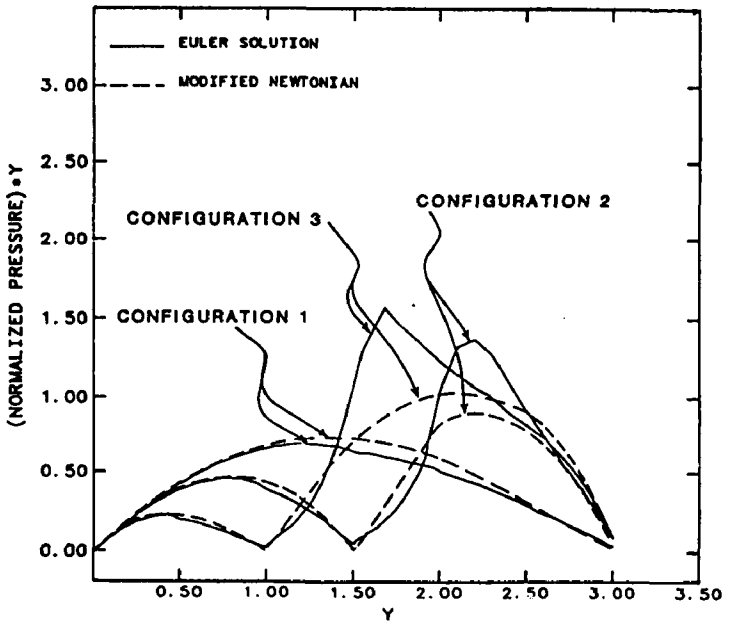

Figure 5-20. Comparison of Surface Pressures Along Radial Coordinate for Configurations 1, 2, and 3 at Free-Stream Mach Number of 18.

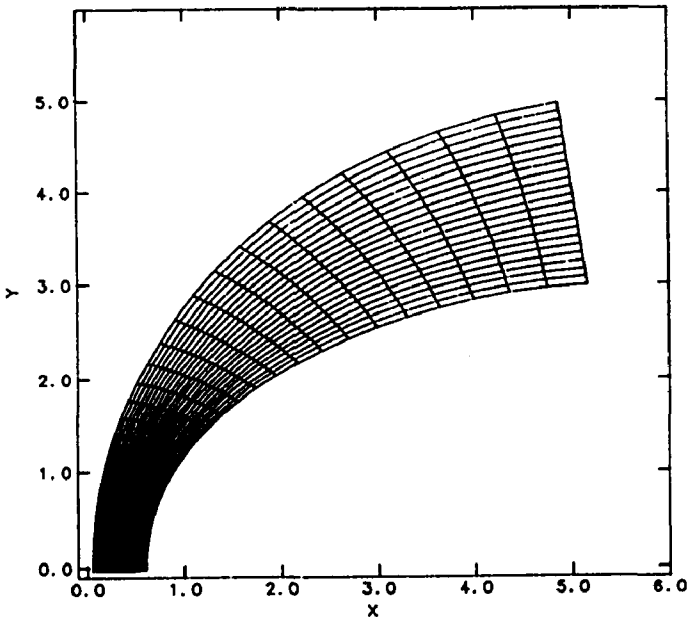

Figure 5-21. Grid System for Ideal Gas Model.

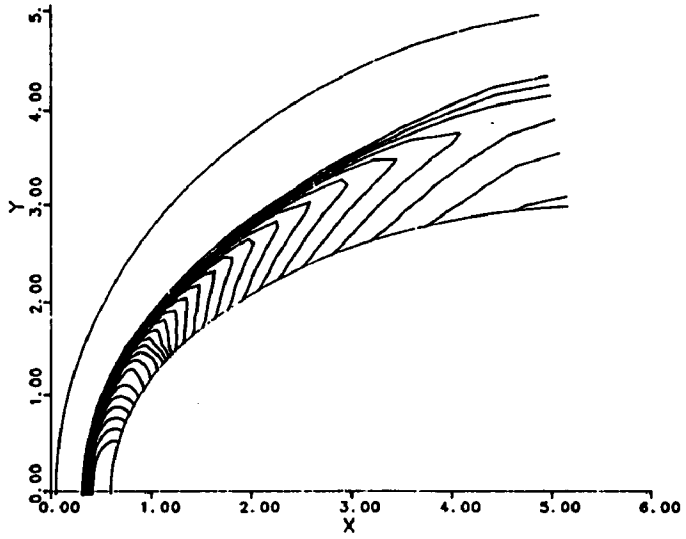

Figure 5-22. Pressure Contour of Ideal Gas Model at Mach 18.

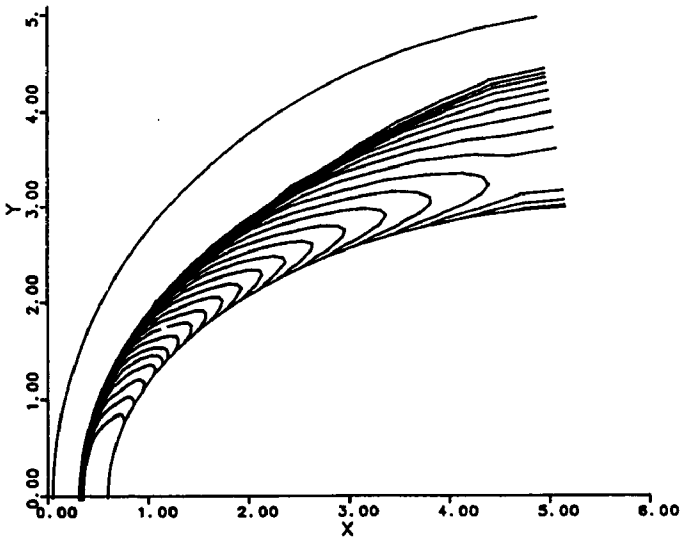

Figure 5-23. Temperature Contours of Ideal Gas Model at Mach 18.

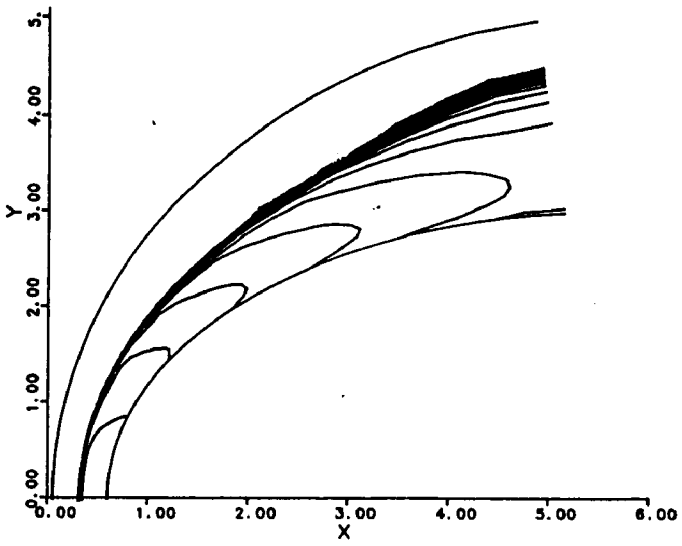

Figure 5-24. Mach Contours of Ideal Gas Model at Mach 18.

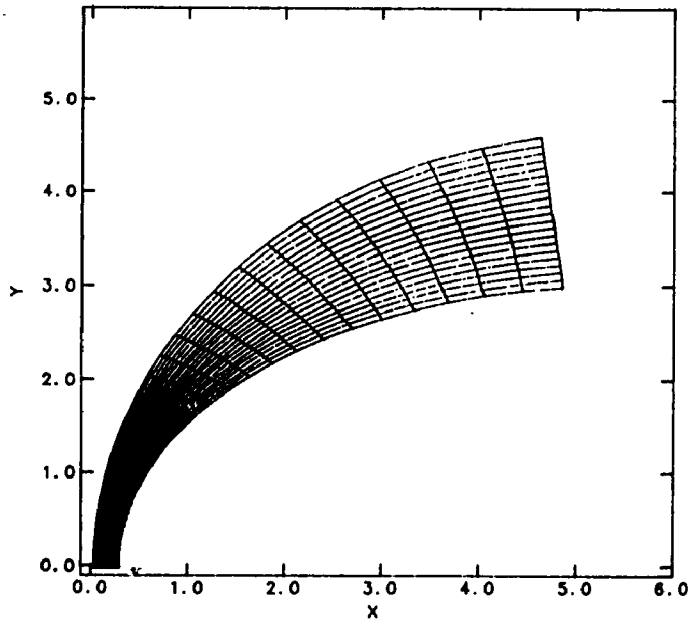

Figure 5-25. Grid System for Finite-Rate Chemistry Model.

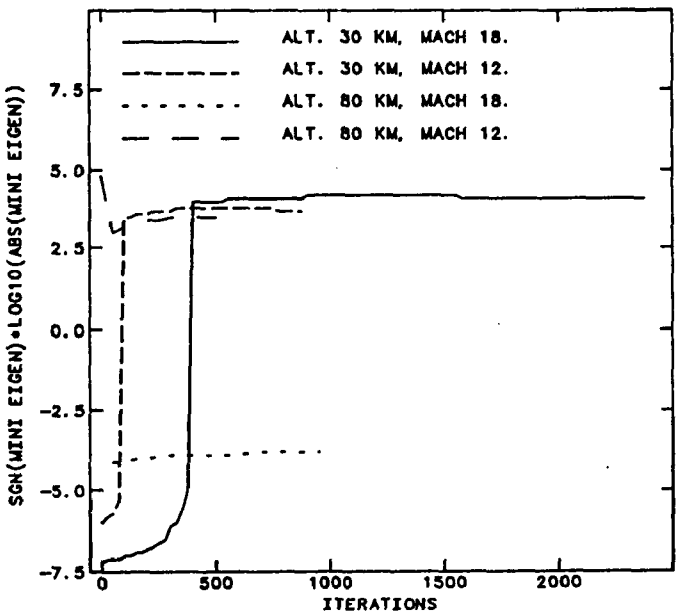

Figure 5-26. Evolution of $Re[\lambda s]$ min for Blunt Body Problem at Various Free-Stream Conditions.

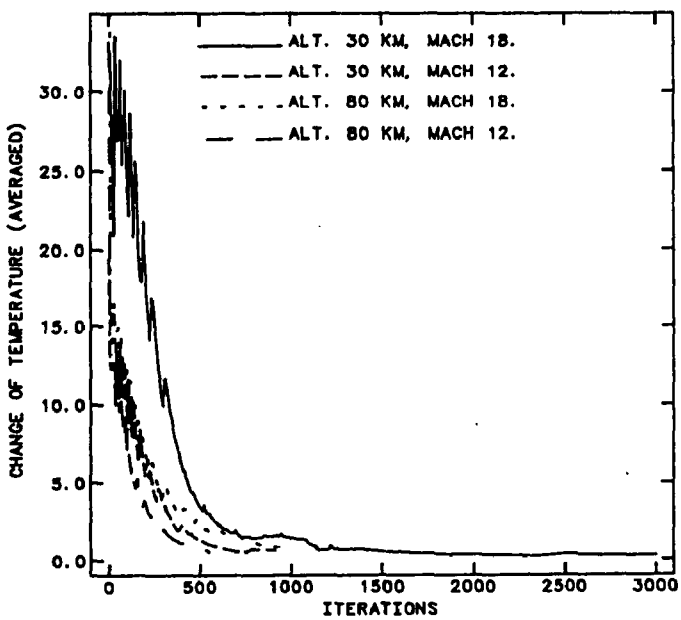

Figure 5-27. Convergence History of the Temperature for Blunt Body Problem at Various Free-Stream Conditions.

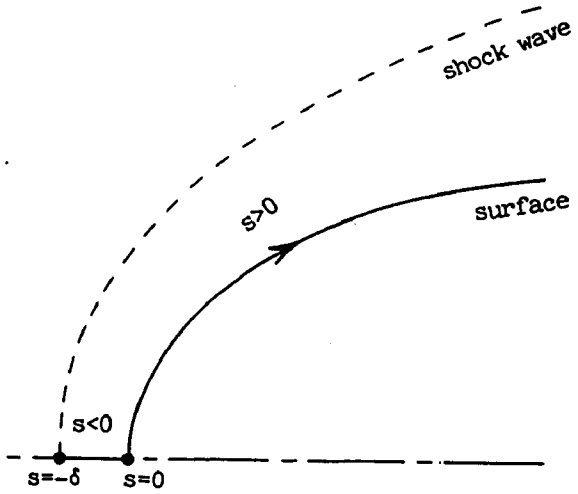

Figure 5-28. Stagnation Streamline Coordinate.

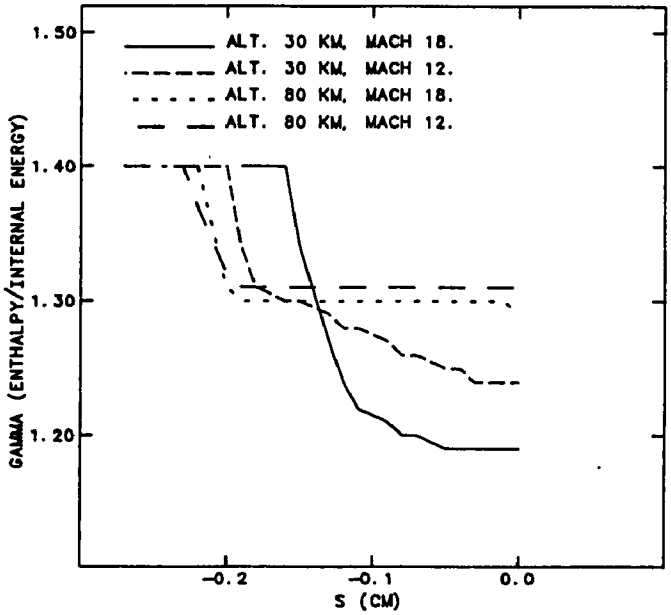

Figure 5-29. Effective γ Distributions Along the Stagnation Streamline at Various Free-Stream Conditions.

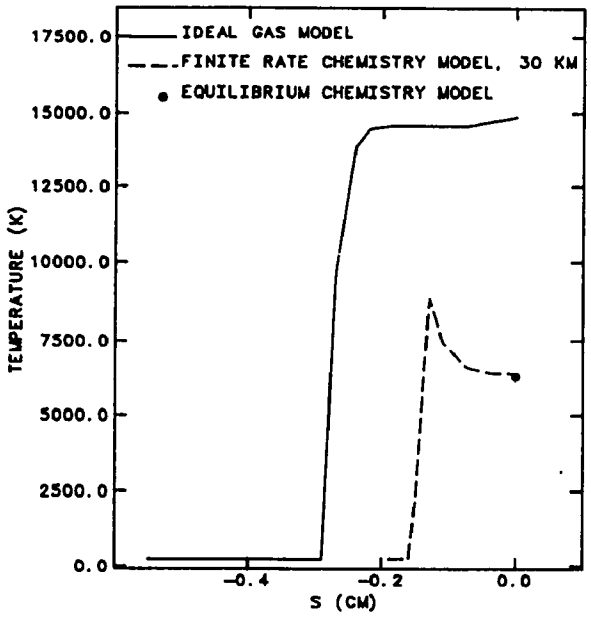

Figure 5-30. Temperature Distributions Along the Stagnation Streamline at Mach Number 18, Altitude 30 km.

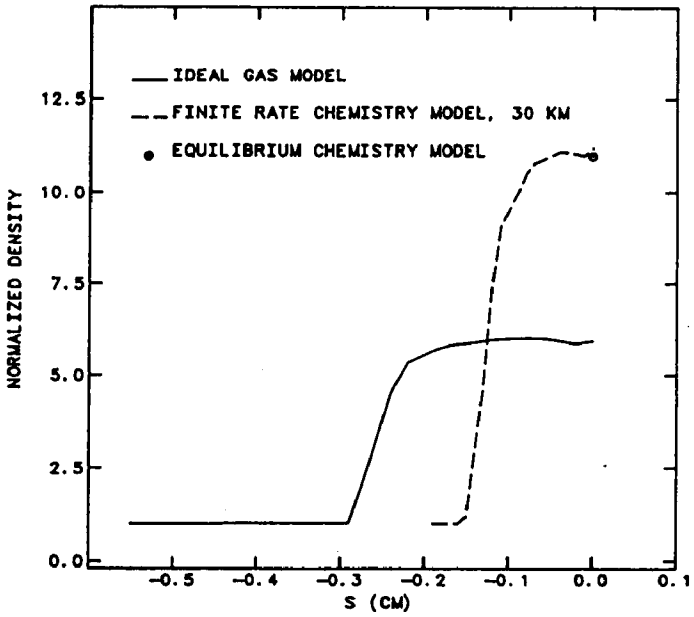

Figure 5-31. Density Distributions Along the Stagnation Streamline at Mach Number 18, Altitude 30 km.

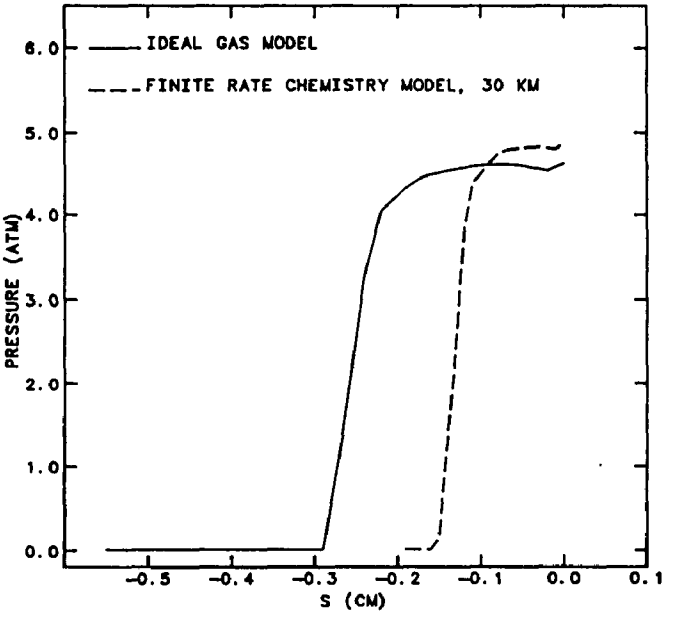

Figure 5-32. Pressure Distributions Along the Stagnation Streamline at Mach Number 18, Altitude 30 km.

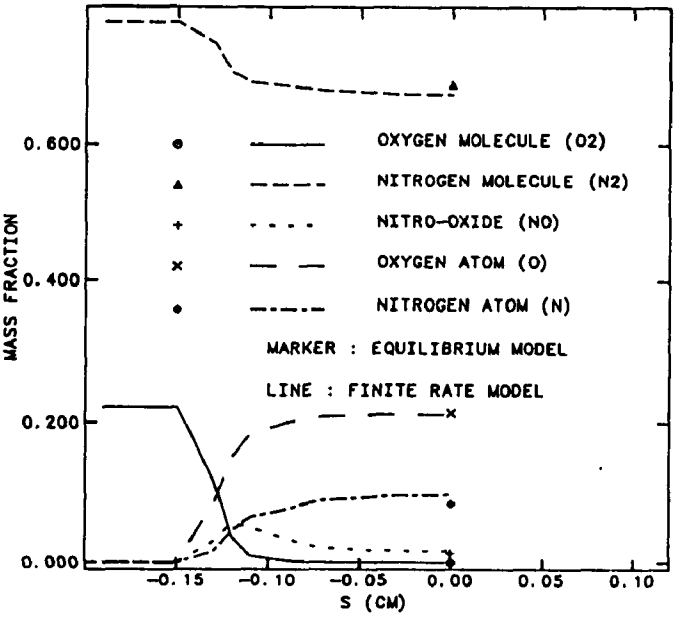

Figure 5-33. Species Mass-Fraction Distributions Along the Stagnation Streamline at Mach Number 18, Altitude 30 km.

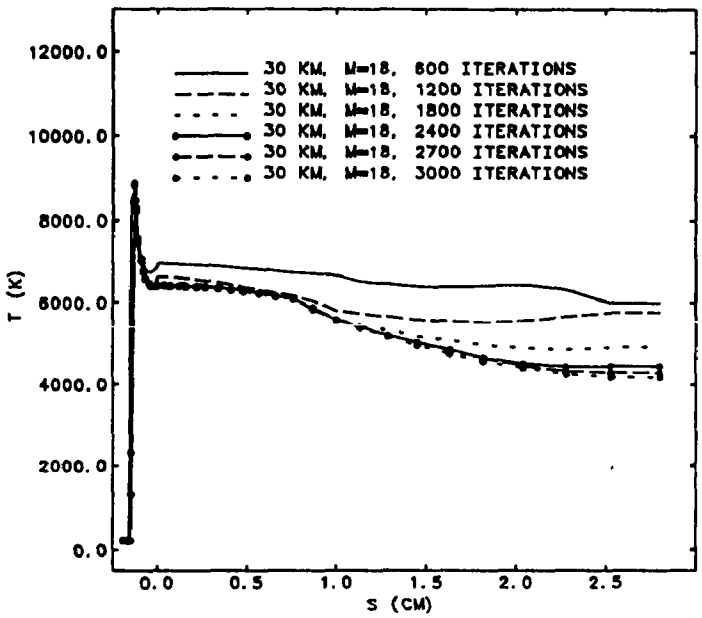

Figure 5-34. Transient and Final Steady-State Temperature Distributions Along the Stagnation Streamline at Mach Number 18, Altitude 30 km.

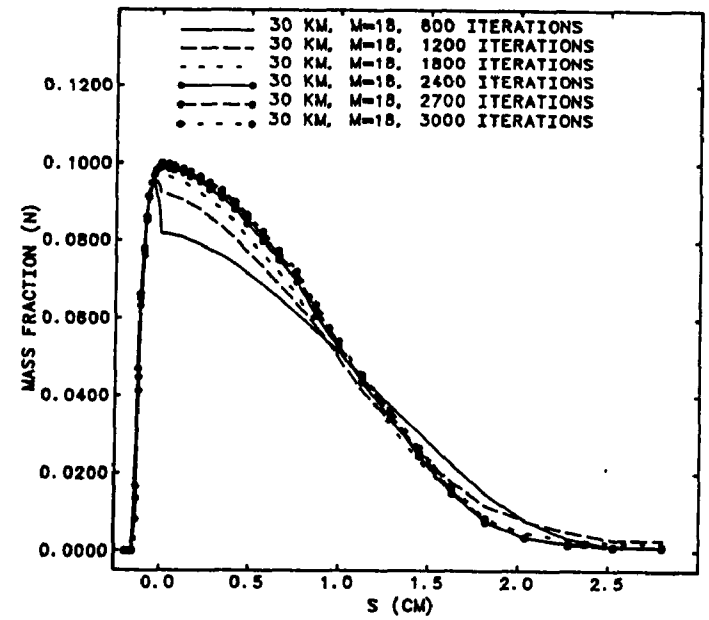

Figure 5-35. Transient and Final Steady-State N Mass-Fraction Distributions Along the Stagnation Streamline at Mach Number 18, Altitude 30 km.

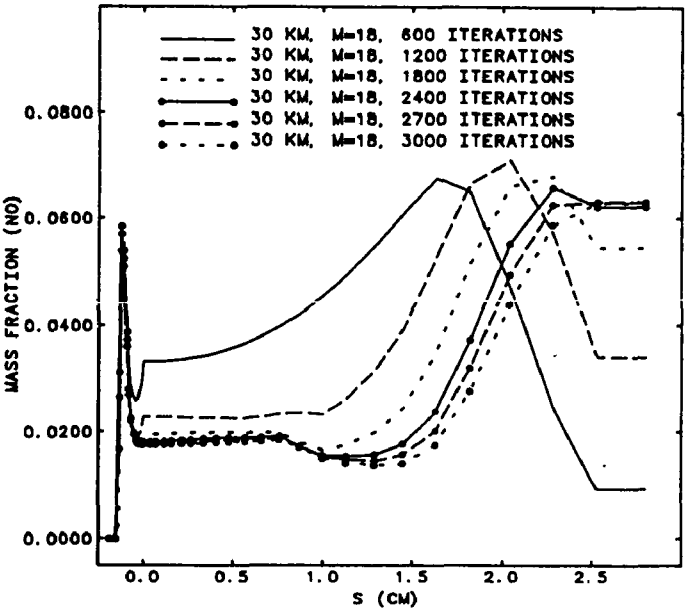

Figure 5-36. Transient and Final Steady-State *NO* Mass-Fraction Distributions Along the Stagnation Streamline at Mach Number 18, Altitude 30 km.

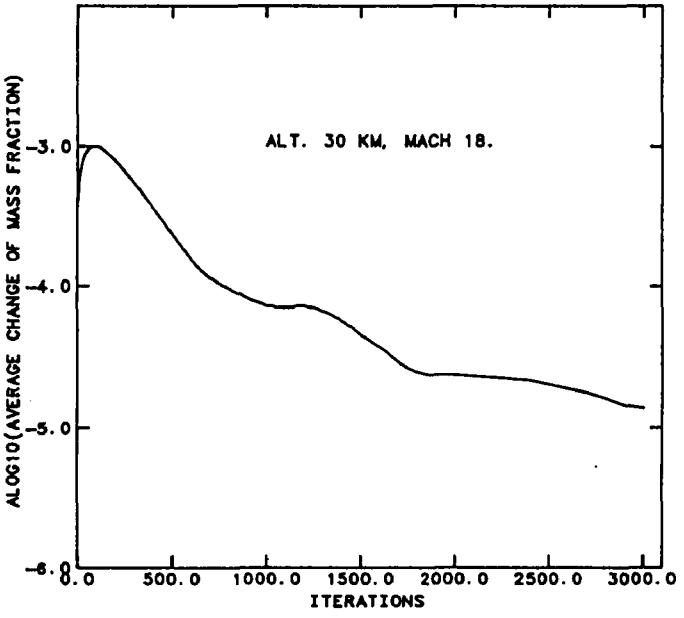

Figure 5-37. Convergence History of the Species Mass-Fraction at Mach Number 18, Altitude 30 km.

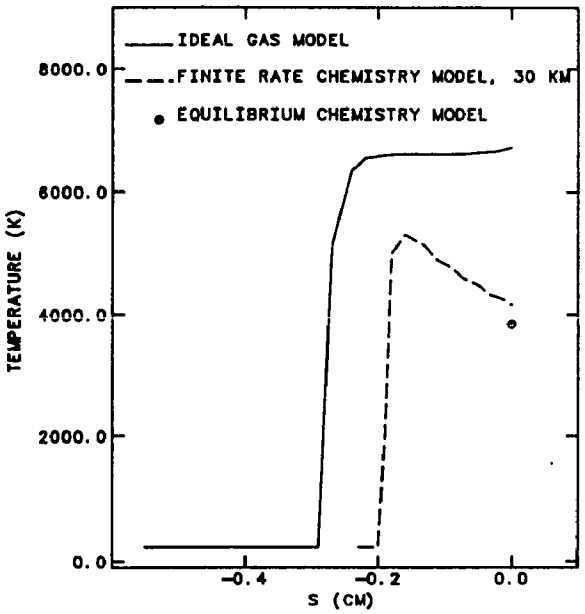

Figure 5-38. Temperature Distributions Along the Stagnation Streamline at Mach Number 12, Altitude 30 km.

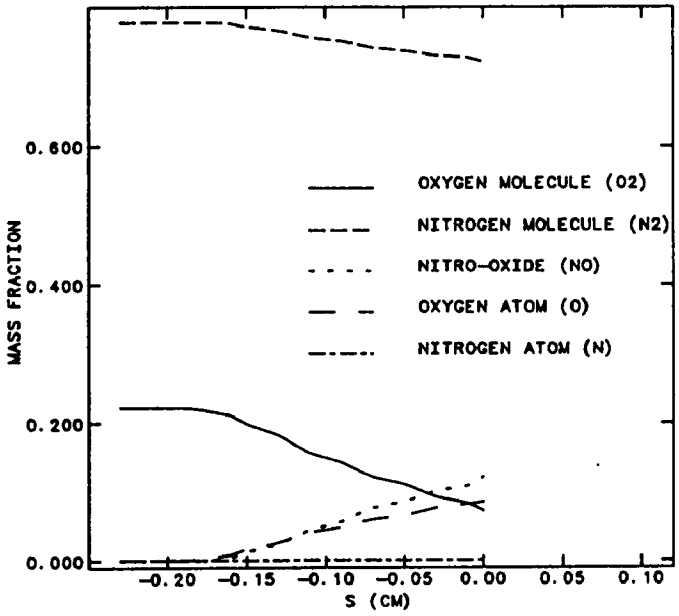

Figure 5-39. Species Mass-Fraction Distributions Along the Stagnation Streamline at Mach Number 12, Altitude 30 km.

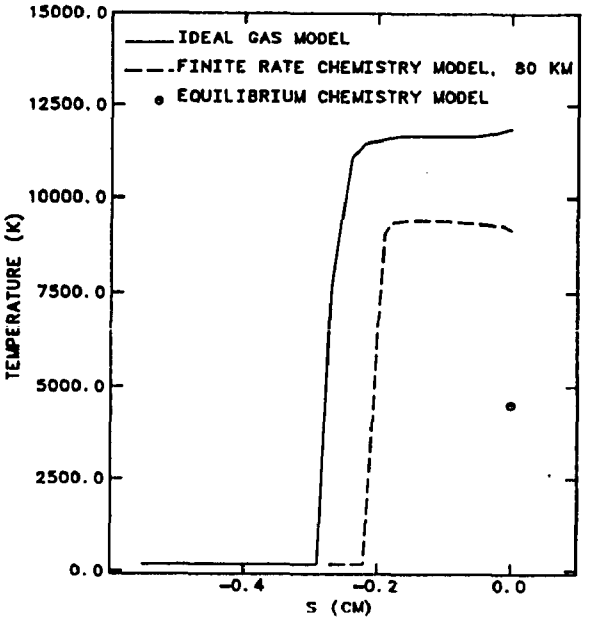

Figure 5-40. Temperature Distributions Along the Stagnation Streamline at Mach Number 18, Altitude 80 km.

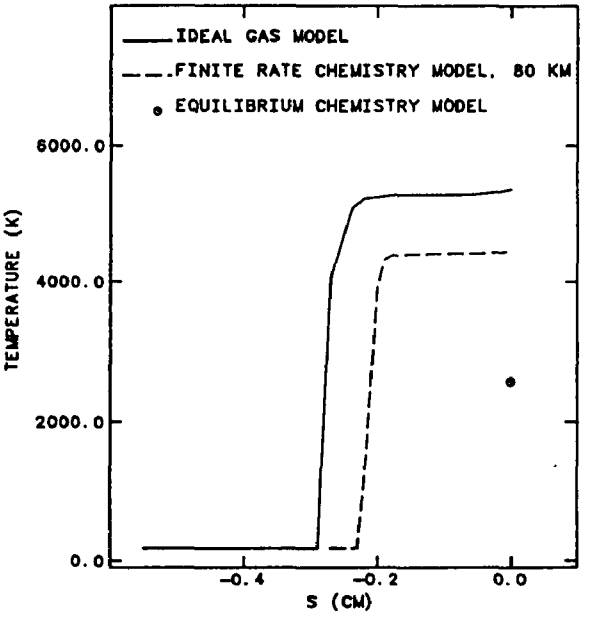

Figure 5-41. Temperature Distributions Along the Stagnation Streamline at Mach Number 12, Altitude 80 km.

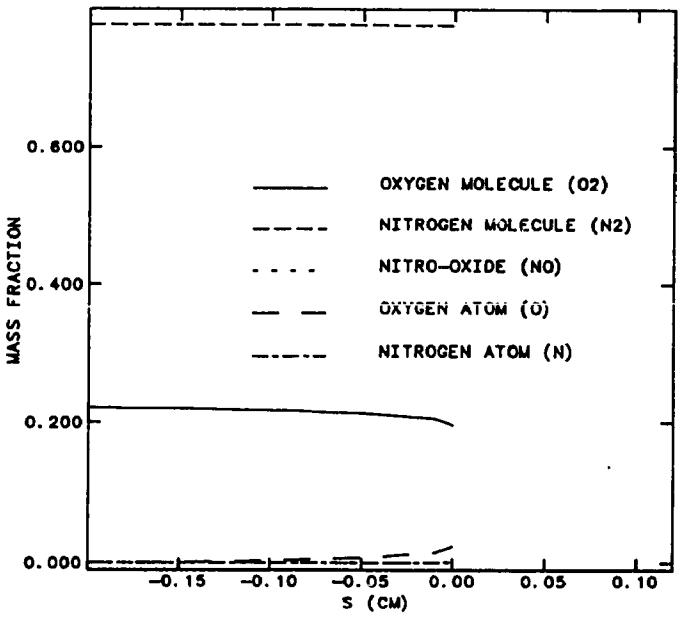

Figure 5-42. Species Mass-Fraction Distributions Along the Stagnation Streamline at Mach Number 18, Altitude 80 km.

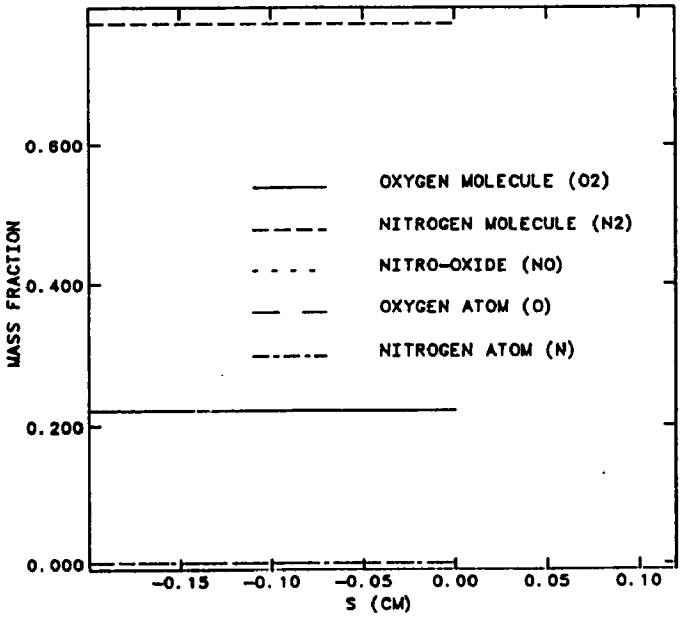

Figure 5-43. Species Mass-Fraction Distributions Along the Stagnation Streamline at Mach Number 12, Altitude 80 km.

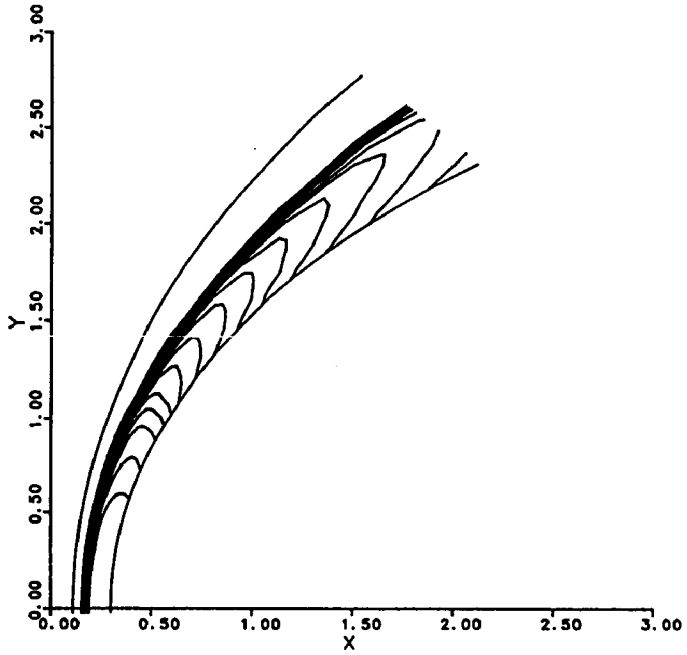

Figure 5-44. Pressure Contours for Mach 18 Flow at Altitude of 30 km.

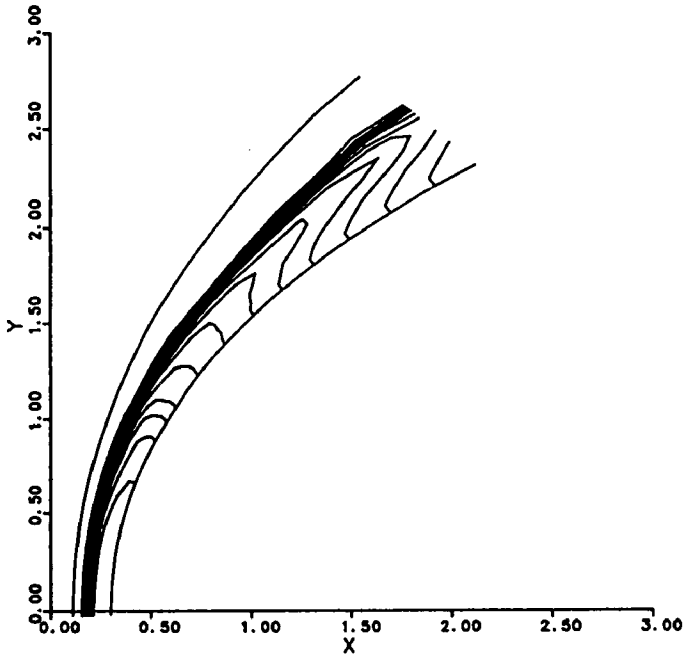

Figure 5-45. Density Contours for Mach 18 Flow at Altitude of 30 km.

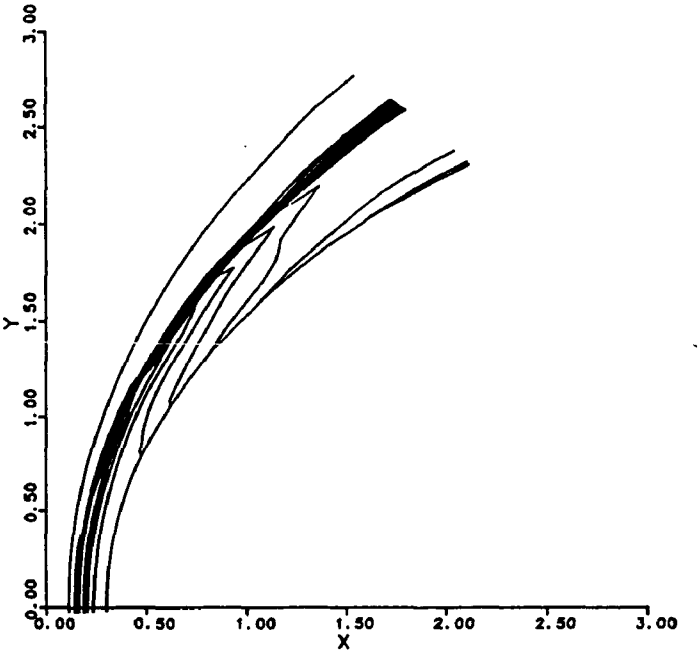

Figure 5-46. Temperature Contours for Mach 18 Flow at Altitude of 30 km.

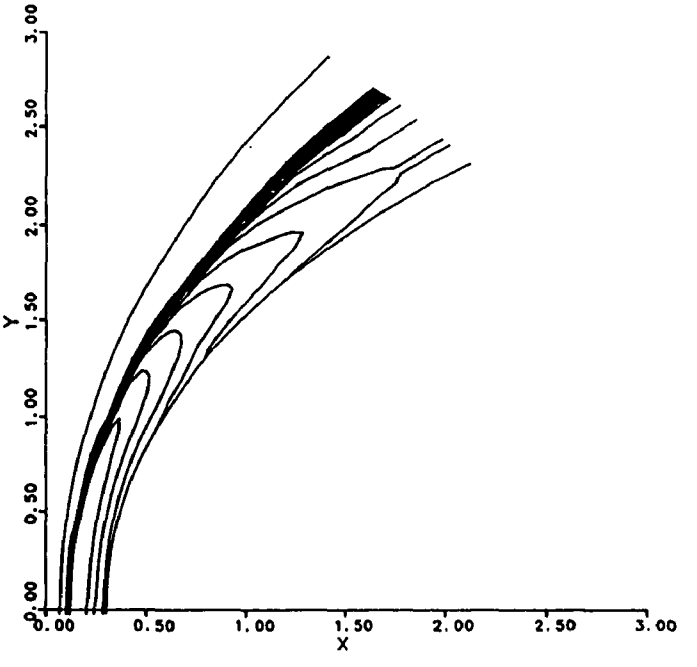

Figure 5-47. Temperature Contours for Mach 12 Flow at Altitude of 30 km.

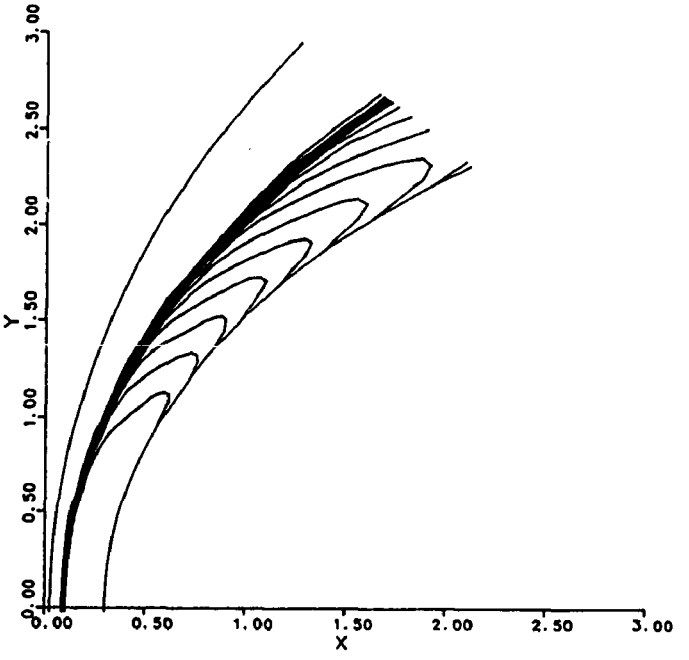

Figure 5-48. Temperature Contours for Mach 18 Flow at Altitude of 80 km.

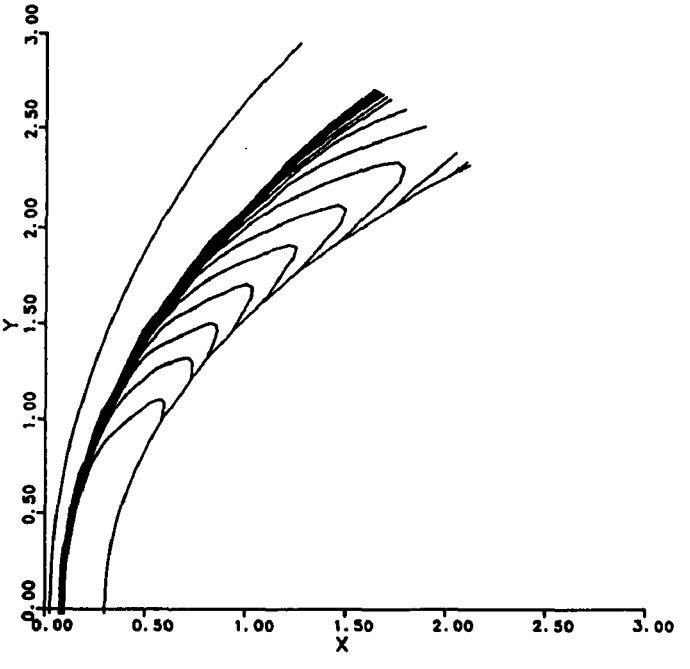

Figure 5-49. Temperature Contours for Mach 12 Flow at Altitude of 80 km.

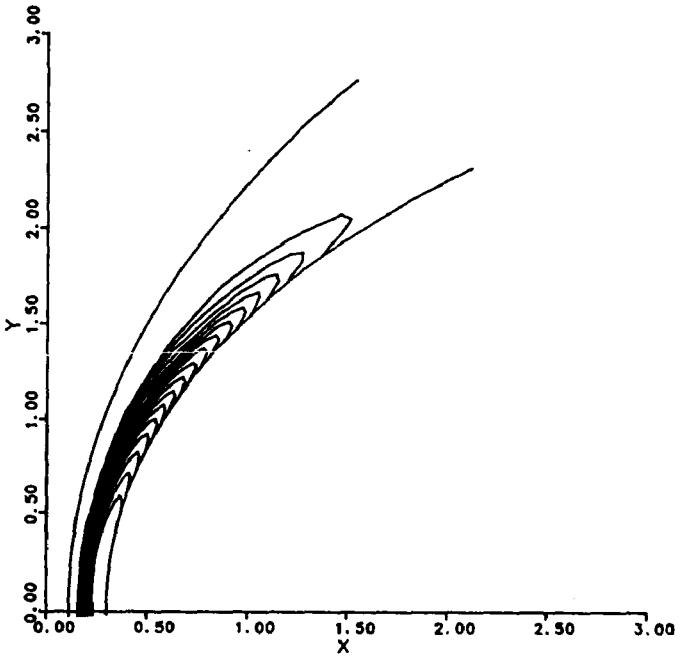

Figure 5-50. Mass-Fraction Contours of N for Mach 18 Flow at Altitude of 30 km.

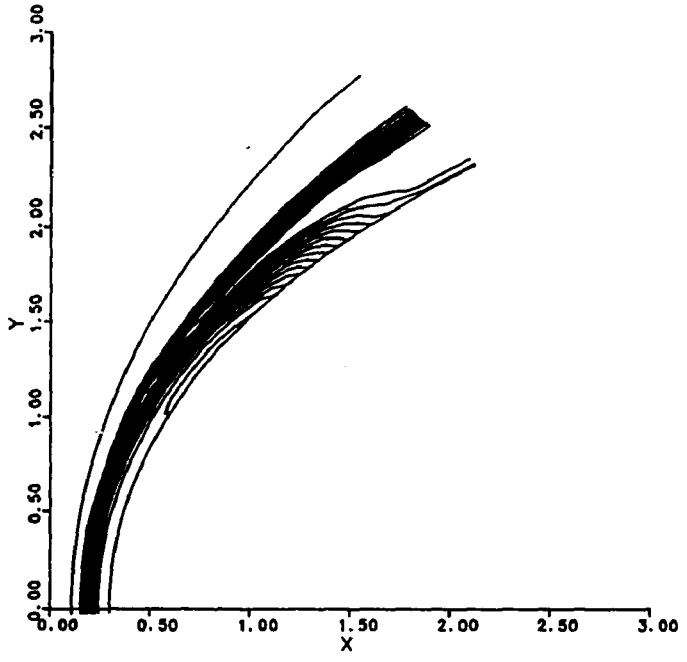

Figure 5-51. Mass-Fraction Contours of NO for Mach 18 Flow at Altitude of 30 km.

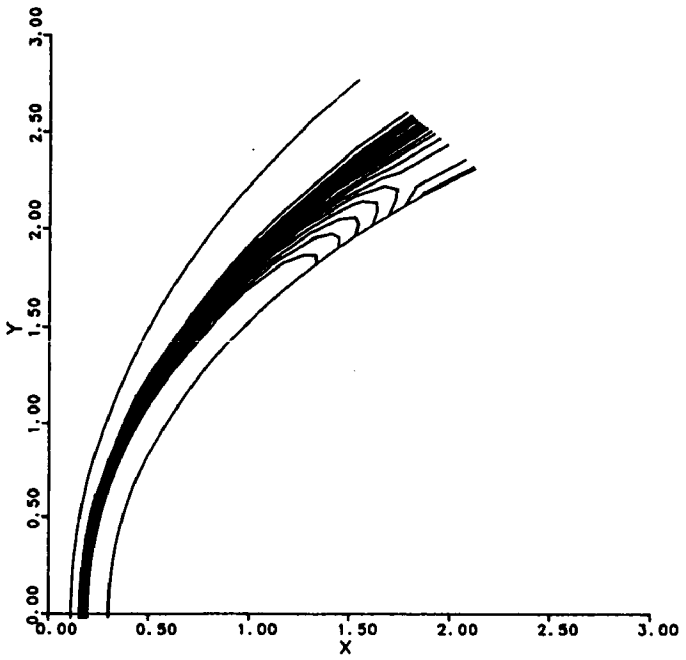

Figure 5-52. Mass-Fraction Contours of O for Mach 18 Flow at Altitude of 30 km.

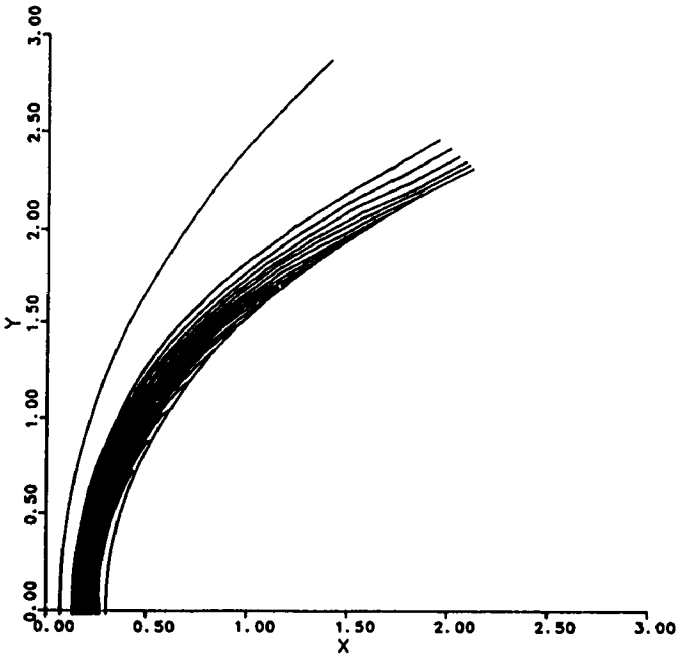

Figure 5-53. Mass-Fraction Contours of O for Mach 12 Flow at Altitude of 30 km.

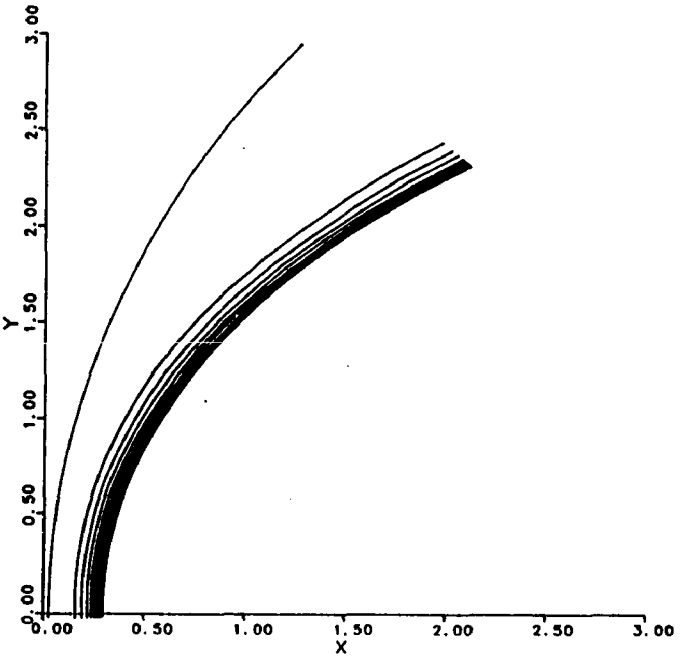

Figure 5-54. Mass-Fraction Contours of O for Mach 18 Flow at Altitude of 80 km.

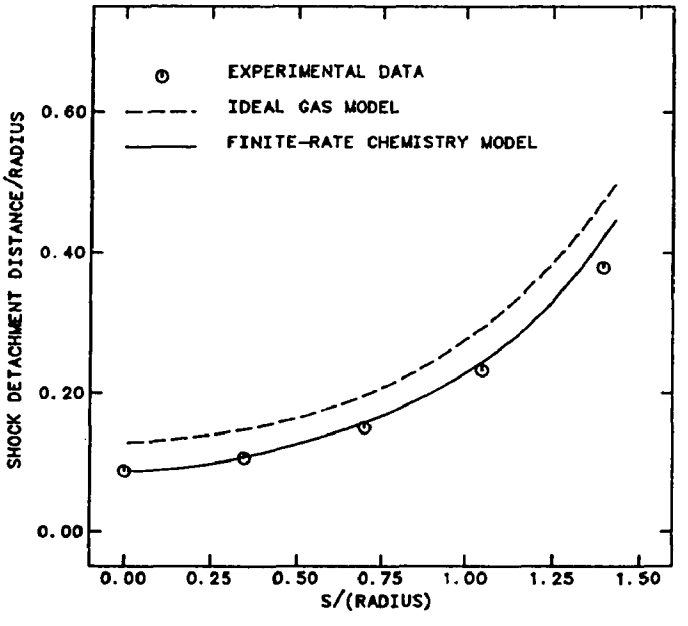

Figure 5-55. Shock Detachment on 1/2 Inch Diameter Sphere.

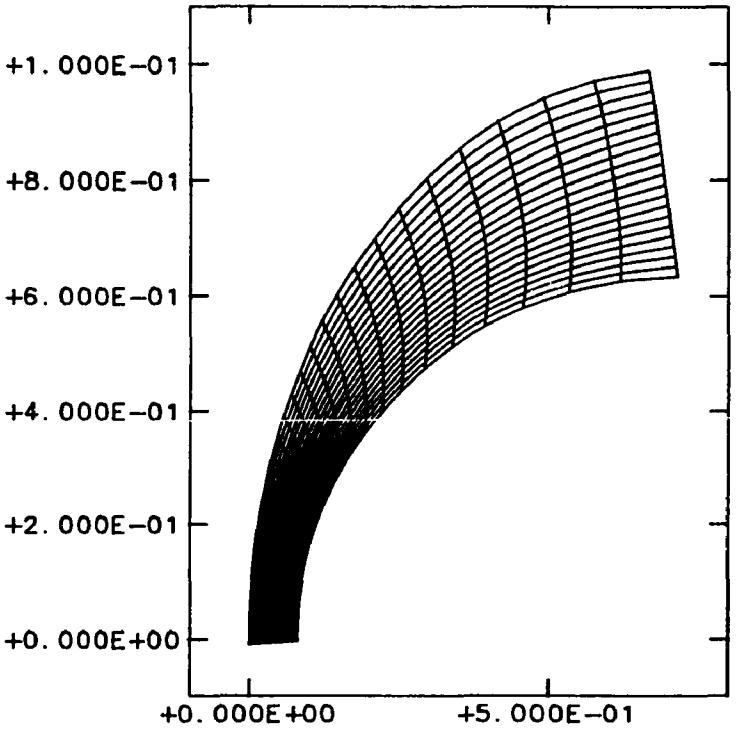

Figure 5-56. Grid System for Sphere.

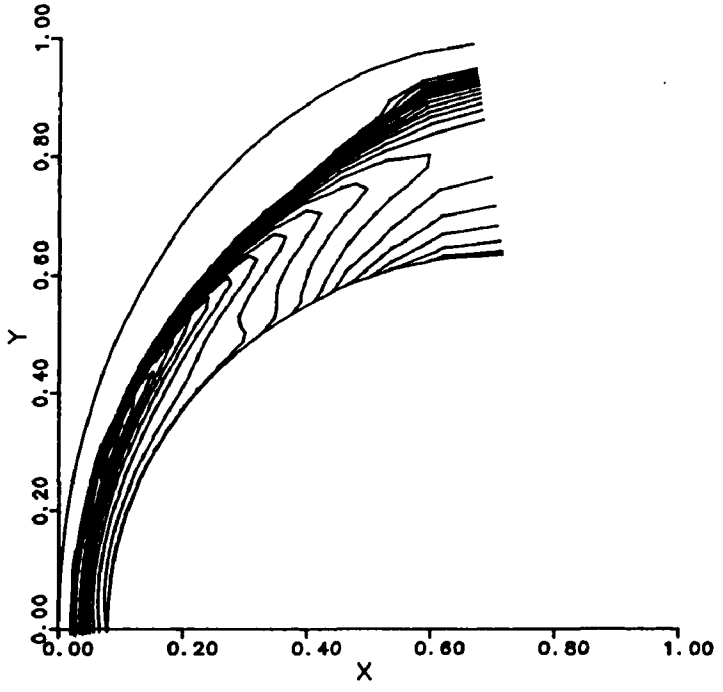

Figure 5-57. Temperature Contours for Mach 15.3 Flow Over a Sphere.

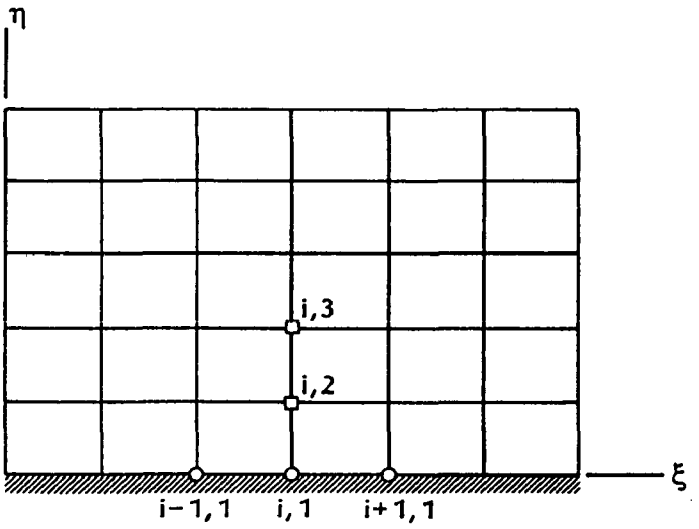

Figure A-1. Illustration of the Grid Points Used in the FDE (A-11).

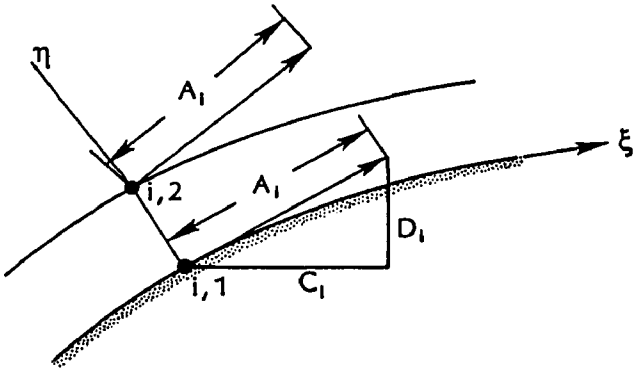

Figure B-1. Approximation of the Velocity at the Surface.

Appendix A

Computation of Pressure at the Body Surface

The components of the momentum equation for an axisymmetric flow may be expressed as:

$$\frac{\partial}{\partial t}(\rho u) + \frac{\partial}{\partial x}(\rho u^2 + P) + \frac{\partial}{\partial y}(\rho uv) + \frac{1}{y}\alpha(\rho uv) = 0 \qquad \text{(A.1)}$$

$$\frac{\partial}{\partial t}(\rho v) + \frac{\partial}{\partial x}(\rho uv) + \frac{\partial}{\partial y}(\rho v^2 + P) + \frac{1}{y}\alpha(\rho v^2) = 0 \qquad \text{(A.2)}$$

By definition

$$\dot{m} = \rho \vec{V} \cdot \hat{n} \qquad \text{(A.3)}$$

and is equal to zero at the surface for a nonporous surface. Now recall that

$$\hat{n} = \frac{\nabla\eta}{|\nabla\eta|}$$

$$\vec{V} = (u\hat{\imath} + v\hat{\jmath})$$

and

$$\nabla\eta = \eta_x\hat{\imath} + \eta_y\hat{\jmath} = J(-y_\xi\hat{\imath} + x_\xi\hat{\jmath})$$

Substitution of these relations into equation (A.3) yields:

$$\rho v x_\xi - \rho u y_\xi = 0 \qquad \text{(A.4)}$$

A time derivative of (A.4) provides

$$x_\xi \frac{\partial}{\partial t}(\rho v) - y_\xi \frac{\partial}{\partial t}(\rho u) = 0 \qquad \text{(A.5)}$$

Note that the grid system has been assumed to be independent of time. Now the following mathematical manipulation is performed. Equation (A.1) is multiplied by y_ξ and subtracted from the product of x_ξ times equation (A.2). The result is

$$y_\xi \frac{\partial}{\partial x}(\rho u^2 + P) + y_\xi \frac{\partial}{\partial y}(\rho uv) - x_\xi \frac{\partial}{\partial x}(\rho uv) - x_\xi \frac{\partial}{\partial y}(\rho v^2 + P) = 0 \qquad \text{(A.6)}$$

This equation may be rearranged as (with the help of equation (A.4))

$$y_\xi \left(\rho u \frac{\partial u}{\partial x} + \rho v \frac{\partial u}{\partial y} + \frac{\partial P}{\partial x}\right) - x_\xi \left(\rho u \frac{\partial v}{\partial x} + \rho v \frac{\partial v}{\partial y} + \frac{\partial P}{\partial y}\right) = 0 \qquad \text{(A.7)}$$

This equation can be expressed as

$$y_\xi \left(\rho u \frac{\partial u}{\partial x} + \rho v \frac{\partial u}{\partial y}\right) - x_\xi \left(\rho u \frac{\partial v}{\partial x} + \rho v \frac{\partial v}{\partial y}\right) = -y_\xi \frac{\partial P}{\partial x} + x_\xi \frac{\partial P}{\partial y}$$

Replace the $\frac{\partial}{\partial x}$ with $\xi_x \frac{\partial}{\partial \xi} + \eta_x \frac{\partial}{\partial \eta}$ and $\frac{\partial}{\partial y}$ with $\xi_y \frac{\partial}{\partial \xi} + \eta_y \frac{\partial}{\partial \eta}$

$$\begin{aligned} & y_\xi \left[\rho u(\xi_x u_\xi + \eta_x u_\eta) + \rho v(\xi_y u_\xi + \eta_y u_\eta)\right] \\ & \quad - x_\xi \left[\rho u(\xi_x v_\xi + \eta_x v_\eta) + \rho v(\xi_y v_\xi + \eta_y v_\eta)\right] \; = \\ & \qquad\qquad - y_\xi(\xi_x P_\xi + \eta_x P_\eta) + x_\xi(\xi_y P_\xi + \eta_y P_\eta) \end{aligned}$$

By intoducing the relations

$$\begin{aligned} \xi_x &= J \cdot y_\eta \\ \xi_y &= J(-x_\eta) \\ \eta_x &= J(-y_\xi) \\ \eta_y &= J(x_\xi) \end{aligned}$$

and $vx_\xi - uy_\xi = 0$ from (A.4).

$$\begin{aligned} & J\rho\left[(-u_\xi y_\xi + x_\xi v_\xi)(x_\eta v - u y_\eta)\right] = \\ & \qquad (-\xi_x y_\xi + x_\xi \xi_y) P_\xi + (-y_\xi \eta_x + x_\xi \eta_y) P_\eta \end{aligned}$$

Resubstitution of relations for the metrics yields:

$$J\rho\left[-u_\xi\left(-\frac{\eta_x}{J}\right)+v_\xi\left(\frac{\eta_y}{J}\right)\right]\left[\left(-\frac{\xi_y}{J}\right)v-\left(\frac{\xi_x}{J}\right)u\right]$$
$$=\left[-\xi_x\left(-\frac{\eta_x}{J}\right)+\xi_y\left(\frac{\eta_y}{J}\right)\right]P_\xi+\left[-\left(-\frac{\eta_x}{J}\right)(\eta_x)+\left(\frac{\eta_y}{J}\right)(\eta_y)\right]P_\eta$$

which may be simplified to

$$-\frac{\rho}{J}(u\xi_x+v\xi_y)(u_\xi\eta_x+v_\xi\eta_y)=\frac{1}{J}(\xi_x\eta_x+\xi_y\eta_y)P_\xi+\frac{1}{J}(\eta_x^2+\eta_y^2)P_\eta \qquad \text{(A.8)}$$

This equation may be expressed in a conservative form by the addition of some "zero" terms. The LHS of the equation is considered first.

The lefthand side of equation (A.8), in terms of the contravariant velocity U, is (excluding the minus sign which will be included at the final result)

$$\text{LHS}=\frac{\rho U}{J}(u_\xi\eta_x+v_\xi\eta_y)$$

A zero term is added to provide

$$\text{LHS}=\frac{\rho U}{J}(u_\xi\eta_x+v_\xi\eta_y)+V\left[\left(\frac{\rho U}{J}\right)_\xi+\left(\frac{\rho V}{J}\right)_\eta\right]$$

Note that the added term is zero because V is zero at the surface. Thus,

$$\begin{aligned}\text{LHS} &= \frac{\rho U}{J}(u_\xi\eta_x+v_\xi\eta_y)+(u\eta_x+v\eta_y)\left[\left(\frac{\rho U}{J}\right)_\xi+\left(\frac{\rho V}{J}\right)_\eta\right]\\ &= u\eta_x\left[\left(\frac{\rho U}{J}\right)_\xi+\left(\frac{\rho V}{J}\right)_\eta\right]+\frac{\rho U}{J}(u_\xi\eta_x+v_\xi\eta_y)\\ &\quad +v\eta_y\left[\left(\frac{\rho U}{J}\right)_\xi+\left(\frac{\rho V}{J}\right)_\eta\right]\end{aligned}$$

Now the zero terms $\left(\frac{\rho V}{J}\right)u_\eta$ and $\left(\frac{\rho V}{J}\right)v_\eta$ are added to yield:

$$\text{LHS}=\eta_x\left[u\left(\frac{\rho U}{J}\right)_\xi+u_\xi\left(\frac{\rho U}{J}\right)\right]+\eta_y\left[v\left(\frac{\rho U}{J}\right)_\xi+v_\xi\left(\frac{\rho U}{J}\right)\right]$$

$$+\eta_x\left[u\left(\frac{\rho V}{J}\right)_\eta + u_\eta\left(\frac{\rho V}{J}\right)\right] + \eta_y\left[v\left(\frac{\rho V}{J}\right)_\eta + v_\eta\left(\frac{\rho V}{J}\right)\right]$$
$$= \eta_x\left[\frac{\rho uU}{J}\right]_\xi + \eta_y\left[\frac{\rho vU}{J}\right]_\xi + \eta_x\left[\frac{\rho uV}{J}\right]_\eta + \eta_y\left[\frac{\rho vV}{J}\right]_\eta \quad \text{(A.9)}$$

Now, the RHS is modified. Recall that

$$\text{RHS} = \frac{1}{J}(\xi_x\eta_x + \xi_y\eta_y)P_\xi + \frac{1}{J}(\eta_x^2 + \eta_y^2)P_\eta$$

Add the following zero term

$$P\left\{\eta_x\left[\left(\frac{\xi_x}{J}\right)_\xi + \left(\frac{\eta_x}{J}\right)_\eta\right] + \eta_y\left[\left(\frac{\xi_y}{J}\right)_\xi + \left(\frac{\eta_y}{J}\right)_\eta\right]\right\} = 0$$

Note that each bracket term is zero. Hence,

$$\begin{aligned}\text{RHS} &= \eta_x\left[\left(\frac{\xi_x}{J}\right)_\xi P + \left(\frac{\xi_x}{J}\right)P_\xi\right] + \eta_x\left[\left(\frac{\eta_x}{J}\right)_\eta P + \left(\frac{\eta_x}{J}\right)P_\eta\right] \\ &\quad + \eta_y\left[\left(\frac{\xi_y}{J}\right)_\xi P + \left(\frac{\xi_y}{J}\right)P_\xi\right] + \eta_y\left[\left(\frac{\eta_y}{J}\right)_\eta P + \left(\frac{\eta_y}{J}\right)P_\eta\right] \\ &= \eta_x\left(\frac{\xi_x P}{J}\right)_\xi + \eta_x\left(\frac{\eta_x P}{J}\right)_\eta + \eta_y\left(\frac{\xi_y P}{J}\right)_\xi + \eta_y\left(\frac{\eta_y P}{J}\right)_\eta \quad \text{(A.10)}\end{aligned}$$

Therefore, the conservative form of equation (A.6) is expressed as

$$\begin{aligned}&\eta_x\left(\frac{\rho uU}{J}\right)_\xi + \eta_y\left(\frac{\rho vU}{J}\right)_\xi + \eta_x\left(\frac{\rho uV}{J}\right)_\eta + \eta_y\left(\frac{\rho vV}{J}\right)_\eta \\ &+\eta_x\left(\frac{\xi_x P}{J}\right)_\xi + \eta_x\left(\frac{\eta_x P}{J}\right)_\eta + \eta_y\left(\frac{\xi_y P}{J}\right)_\xi + \eta_y\left(\frac{\eta_y P}{J}\right)_\eta = 0 \quad \text{(A.11)}\end{aligned}$$

In order to obtain a finite difference equation for (A.11), a second-order central difference approximation for the ξ derivatives and a second-order one-sided difference approximation for the η derivatives is used. Note that the unknowns are the values of pressure at the surface, i.e., $j = 1$. The values at

the interior points have already been computed. The grid points involved are illustrated in Fig. A-1. With the second-order approximation described above, the FDE is obtained as

$$\begin{aligned}
&\frac{\eta_{x_{i,1}}}{2\Delta\xi}\left[\left(\frac{\rho uU}{J}\right)_{i+1,1}-\left(\frac{\rho uU}{J}\right)_{i-1,1}\right]+\frac{\eta_{y_{i,1}}}{2\Delta\xi}\left[\left(\frac{\rho uU}{J}\right)_{i+1,1}-\left(\frac{\rho uU}{J}\right)_{i-1,1}\right]\\
&+\frac{\eta_{x_{i,1}}}{2\Delta\eta}\left[-3\left(\frac{\rho uV}{J}\right)_{i,1}+4\left(\frac{\rho uV}{J}\right)_{i,2}-\left(\frac{\rho uV}{J}\right)_{i,3}\right]\\
&+\frac{\eta_{y_{i,1}}}{2\Delta\eta}\left[-3\left(\frac{\rho vV}{J}\right)_{i,1}+4\left(\frac{\rho vV}{J}\right)_{i,2}-\left(\frac{\rho vV}{J}\right)_{i,3}\right]\\
&+\frac{\eta_{x_{i,1}}}{2\Delta\xi}\left[\left(\frac{\xi_x P}{J}\right)_{i+1,1}-\left(\frac{\xi_x P}{J}\right)_{i-1,1}\right]+\frac{\eta_{x_{i,1}}}{2\Delta\eta}\left[-3\left(\frac{\eta_x P}{J}\right)_{i,1}\right.\\
&\left.+4\left(\frac{\eta_x P}{J}\right)_{i,2}-\left(\frac{\eta_x P}{J}\right)_{i,3}\right]+\frac{\eta_{y_{i,1}}}{2\Delta\xi}\left[\left(\frac{\xi_y P}{J}\right)_{i+1,1}-\left(\frac{\xi_y P}{J}\right)_{i-1,1}\right]\\
&+\frac{\eta_{y_{i,1}}}{2\Delta\eta}\left[-3\left(\frac{\eta_y P}{J}\right)_{i,1}+4\left(\frac{\eta_y P}{J}\right)_{i,2}-\left(\frac{\eta_y P}{J}\right)_{i,3}\right]=0 \qquad \text{(A.12)}
\end{aligned}$$

Note that V is zero at the surface where $j = 1$ and, therefore, those terms are dropped. Now this equation is regrouped so that a tridiagonal system is formed. The rearrangement is as follows:

$$a_i P_{i-1,1} + b_i P_{i,1} + c_i P_{i+1,1} = d_i \qquad \text{(A.13)}$$

where

$$\begin{aligned}
a_i &= -\frac{1}{2\Delta\xi}\left[\eta_{x_{i,1}}\left(\frac{\xi_x}{J}\right)_{i-1,1}+\eta_{y_{i,1}}\left(\frac{\xi_y}{J}\right)_{i-1,1}\right]\\
b_i &= -\frac{3}{2\Delta\eta}\left[\frac{\eta_x^2+\eta_y^2}{J}\right]_{i,1}\\
c_i &= \frac{1}{2\Delta\xi}\left[\eta_{x_{i,1}}\left(\frac{\xi_x}{J}\right)_{i+1,1}+\eta_{y_{i,1}}\left(\frac{\xi_y}{J}\right)_{i+1,1}\right]
\end{aligned}$$

$$
\begin{aligned}
d_i \;=\; & \frac{P_{i,3}}{2\Delta\eta}\left[\eta_{x_{i,1}}\left(\frac{\eta_x}{J}\right)_{i,3}+\eta_{y_{i,1}}\left(\frac{\eta_y}{J}\right)_{i,3}\right] \\
& -\frac{2P_{i,2}}{\Delta\eta}\left[\eta_{x_{i,1}}\left(\frac{\eta_x}{J}\right)_{i,2}+\eta_{y_{i,1}}\left(\frac{\eta_y}{J}\right)_{i,2}\right] \\
& -\frac{2}{\Delta\eta}\left(\frac{\rho V}{J}\right)_{i,2}\left[\eta_{x_{i,1}}u_{i,2}+\eta_{y_{i,1}}v_{i,2}\right] \\
& +\frac{1}{2\Delta\eta}\left(\frac{\rho V}{J}\right)_{i,3}\left[\eta_{x_{i,1}}u_{i,3}+\eta_{y_{i,1}}v_{i,3}\right] \\
& +\frac{1}{2\Delta\xi}\left(\frac{\rho U}{J}\right)_{i-1,1}\left[\eta_{x_{i,1}}u_{i-1,1}+\eta_{y_{i,1}}v_{i-1,1}\right] \\
& -\frac{1}{2\Delta\xi}\left(\frac{\rho U}{J}\right)_{i+1,1}\left[\eta_{x_{i,1}}u_{i+1,1}+\eta_{y_{i,1}}v_{i+1,1}\right]
\end{aligned}
$$

When equation (A-13) is applied to all i at $j = 1$, the following tridiagonal system of equations is obtained.:

$$
\begin{bmatrix}
b_2 & c_2 & & & \\
a_3 & b_3 & c_3 & & \\
 & & & & \\
 & a_{IMM2} & b_{IMM2} & c_{IMM2} & \\
 & & a_{IMM1} & b_{IMM1}
\end{bmatrix}
\begin{bmatrix} P_{2,1} \\ P_{3,1} \\ | \\ P_{IMM2,1} \\ P_{IMM1,1} \end{bmatrix}
=
\begin{bmatrix} d_2 - a_2 P_{1,1} \\ d_3 \\ | \\ d_{IMM2} \\ d_{IMM1} - c_{IMM1} P_{IM,1} \end{bmatrix}
$$

Since $P_{1,1} = P_{2,1}$ and $\frac{P_{IM,1}}{J_{IM,1}} = \frac{P_{IMM1,1}}{J_{IMM1,1}}$, therefore

$$
\begin{bmatrix}
\bar{b}_2 & c_2 & & & \\
a_3 & b_3 & c_3 & & \\
 & & & & \\
 & a_{IMM2} & b_{IMM2} & c_{IMM2} & \\
 & & a_{IMM1} & \bar{b}_{IMM1}
\end{bmatrix}
\begin{bmatrix} P_{2,1} \\ P_{3,1} \\ | \\ P_{IMM2,1} \\ P_{IMM1,1} \end{bmatrix}
=
\begin{bmatrix} d_2 \\ d_3 \\ | \\ d_{IMM2} \\ d_{IMM1} \end{bmatrix}
\qquad \text{(A.14)}
$$

where

$$\bar{b}_2 = a_2 + b_2$$

and

$$\bar{b}_{IMM1} = b_{IMM1} + c_{IMM1}\frac{J_{IM,1}}{J_{IMM1,1}}$$

Appendix B

Density and Velocity Components at the Wall

Recall that the total enthalpy at the surface is assumed constant. This statement is expressed mathematically as

$$\gamma e + \frac{1}{2}(u^2 + v^2) = (h_t)_{\text{wall}} = \text{constant}$$

or for a perfect gas

$$\gamma \left[\frac{P_{i,1}}{(\gamma - 1)\rho_{i,1}}\right] + \frac{1}{2}\frac{C_i^2 + D_i^2}{\rho_{i,1}^2} = (h_t)_{\text{wall}}$$

Note that $(h_t)_{\text{wall}}$ is known from equation (2.82). This equation is rearranged as

$$[2(h_t)_{\text{wall}}(\gamma - 1)]\,\rho_{i,1}^2 - (2\gamma)P_{i,1}\rho_{i,1} + (1 - \gamma)\,(C_i^2 + D_i^2) = 0$$

which may be solved for the density at the wall to yield:

$$\rho_{i,1} = \frac{2\gamma P_{i,1} + \sqrt{4\gamma^2 P_{i,1}^2 + 8(h_t)_{\text{wall}}(\gamma - 1)^2(C_i^2 + D_i^2)}}{4(\gamma - 1)(h_t)_{\text{wall}}}$$

Note that the positive sign is used exclusively to prevent negative density values.

The velocity at the surface may be initialized in different ways. One may extrapolate U from the interior points; or, the same value for $\rho\ \vec{V}$ is imposed at the surface with the vector rotated such that the velocity is tangent

at the surface. Thus,

$$
\begin{aligned}
A_i &= |\rho \vec{V}|_{i,2} \\
C_i &= (\rho u)_{i,1} \\
D_i &= (\rho v)_{i,1}
\end{aligned}
$$

These quantities are illustrated in Fig. B-1.

Appendix C

Constants for Rate Equations

Chemical Reaction	Equilibrium Constant					Heavy Particle M	Constants for K_f			K_f^i, K_b^i
	A_1	A_2	A_3	A_4	A_5		C	n	E/K	i
$O_2 + M \rightleftarrows 2O + M$	2.855	0.988	−6.181	−0.023	−0.001	N, O	2.90^{23}	−2.0	59750.	1
						N_2, O_2, NO	9.68^{22}			2
$N_2 + M \rightleftarrows 2N + M$	1.858	−1.325	−9.856	−0.174	0.08	N	1.60^{22}	−1.6	113200.	3
						O	4.98^{22}			4
						N_2, O_2	3.70^{21}			5
						NO	4.98^{21}			6
$NO + M \rightleftarrows N + O + M$	0.792	−0.492	−6.761	−0.091	0.004	N, O, N_2, O_2, NO	7.95^{23}	−2.0	75500.	7
$NO + O \rightleftarrows N + O_2$	−2.063	−1.48	−0.58	−0.114	0.005		8.37^{12}	0	19450.	8
$O + N_2 \rightleftarrows N + NO$	1.066	−0.833	−3.095	−0.084	0.004		6.44^{17}	−1.0	38370.	9

Appendix D

Species Concentration Change Rate

(a)

Consider the reaction given by equation (3.14), i.e.,

$$O_2 + M \rightleftarrows 2O + M \tag{D.1}$$

Therefore, $\frac{d[O_2]}{dt}$ from equation (D.1) will be

$$\begin{aligned}\frac{d[O_2]}{dt} &= [O]^2 \left\{K_b^1 ([N] + [O]) + K_b^2 ([N_2] + [O_2] + [NO])\right\} \\ &\quad - [O_2] \left\{K_f^1 ([N] + [O]) + K_f^2 ([N_2] + [O_2] + [NO])\right\} \\ &= R_1\end{aligned}$$

and $\frac{d[O]}{dt} = -2R_1$.

(b)

From reaction

$$N_2 + M \rightleftarrows 2N + M \tag{D.2}$$

$$\begin{aligned}\frac{d[N_2]}{dt} &= [N]^2 \left\{K_b^3 [N] + K_b^4 [O] + K_b^5 ([N_2] + [O_2]) + K_b^6 [NO]\right\} \\ &\quad - [N_2] \left\{K_f^3 [N] + K_f^4 [O] + K_f^5 ([N_2] + [O_2]) + K_f^6 [NO]\right\} \\ &= R_2\end{aligned}$$

and $\frac{d[N]}{dt} = -2R_2$.

(c)

From reaction $NO + M \rightleftarrows N + O + M$

$$\begin{aligned} \frac{d[NO]}{dt} &= \left(K_b^7 [N]\,[O] - K_f^7 [NO]\right)\left([N] + [O] + [O_2] + [N_2] + [NO]\right) \\ &= R_3 \end{aligned} \tag{D.3}$$

and $\frac{d[N]}{dt} = \frac{d[O]}{dt} = -R_3$.

(d)

From reaction

$$NO + O \rightleftarrows N + O_2 \tag{D.4}$$

$$\frac{d[NO]}{dt} = \frac{d[O]}{dt} = K_b^8 [N]\,[O_2] - K_f^8 [NO]\,[O] = R_4$$
$$\frac{d[N]}{dt} = \frac{d[O_2]}{dt} = -R_4$$

(e)

From reaction

$$O + N_2 \rightleftarrows N + NO \tag{D.5}$$

$$\frac{d[O]}{dt} = \frac{d[N_2]}{dt} = K_b^9 [NO]\,[N] - K_f^9 [N_2]\,[O] = R_5$$
$$\frac{d[N]}{dt} = \frac{d[NO]}{dt} = -R_5$$

Therefore, the five species total change rate of concentrations from the five reactions are:

$$\frac{d[O_2]}{dt} = R_1 - R_4 \tag{D.6}$$

$$\frac{d[N_2]}{dt} = R_2 + R_5 \tag{D.7}$$

$$\frac{d[NO]}{dt} = R_3 + R_4 - R_5 \tag{D.8}$$

$$\frac{d[O]}{dt} = -2R_1 - R_3 + R_4 + R_5 \tag{D.9}$$

$$\frac{d[N]}{dt} = -2R_2 - R_3 - R_4 - R_5 \tag{D.10}$$

Note K_b^i and K_f^i (for $i = 1, \ldots 9$) are defined in Appendix C.

Appendix E

Jacobian Matrix D

Jacobian matrix $[D]$ is defined as

$$[D] = \frac{\partial \bar{W}}{\partial \bar{Q}} = \frac{\partial W}{\partial Q} \tag{E.1}$$

define $q_s = \rho C_s$ for $s = 1, \ldots 5$, then the element $D_{i,j}$ of $[D]$ can be expressed as

$$D_{i,j} = \frac{\partial(-\dot{w}_i)}{\partial q_j} \quad \text{for} \quad i = 1 \ldots 5, \quad j = 1, \quad \ldots 5 \tag{E.2}$$

Recall equation (3.27) given by $\dot{w}_i = M_i \frac{d[X_i]}{dt}$ and substitute equations (D.6) through (D.10) into the $\frac{d[X_i]}{dt}$ term, then

$$\dot{w}_1 = M_1 \frac{d[O_2]}{dt} = 32(R_1 - R_4) \tag{E.3}$$

$$\dot{w}_2 = M_2 \frac{d[N_2]}{dt} = 28(R_2 + R_5) \tag{E.4}$$

$$\dot{w}_3 = M_3 \frac{d[NO]}{dt} = 30(R_3 + R_4 - R_5) \tag{E.5}$$

$$\dot{w}_4 = M_4 \frac{d[O]}{dt} = 16(-2R_1 - R_3 + R_4 + R_5) \tag{E.6}$$

$$\dot{w}_5 = M_5 \frac{d[N]}{dt} = 14(-2R_2 - R_3 - R_4 - R_5) \tag{E.7}$$

Note that the mass conservation law can be identified here by summing up $\dot{w}_1$ through $\dot{w}_5$ equal to 0, because there is no net mass production, even in a chemical reaction. Substitute equations (E.3) through (E.7) into equation

(E.2); the elements $D_{i,j}$ of matrix $[D]$ can be expressed as

$$D_{1,j} = -32\left(\frac{\partial R_1}{\partial q_j} - \frac{\partial R_4}{\partial q_j}\right) \tag{E.8}$$

$$D_{2,j} = -28\left(\frac{\partial R_2}{\partial q_j} + \frac{\partial R_5}{\partial q_j}\right) \tag{E.9}$$

$$D_{3,j} = -30\left(\frac{\partial R_3}{\partial q_j} + \frac{\partial R_4}{\partial q_j} - \frac{\partial R_5}{\partial q_j}\right) \tag{E.10}$$

$$D_{4,j} = -16\left(-2\frac{\partial R_1}{\partial q_j} - \frac{\partial R_3}{\partial q_j} + \frac{\partial R_4}{\partial q_j} + \frac{\partial R_5}{\partial q_j}\right) \tag{E.11}$$

$$D_{5,j} = -14\left(-2\frac{\partial R_2}{\partial q_j} - \frac{\partial R_3}{\partial q_j} - \frac{\partial R_4}{\partial q_j} - \frac{\partial R_5}{\partial q_j}\right) \tag{E.12}$$

where $j = 1, \ldots 5$, and

$$\frac{\partial R_1}{\partial q_1} = \frac{1}{32}\left\{[O]^2 K_b^2 - K_f^1([O] + [N]) - K_f^2([O_2] + [N_2] + [NO]) - [O_2] K_f^2\right\} \tag{E.13}$$

$$\frac{\partial R_1}{\partial q_2} = \frac{1}{28}\left\{[O]^2 K_b^2 - [O_2] K_f^2\right\} \tag{E.14}$$

$$\frac{\partial R_1}{\partial q_3} = \frac{1}{30}\left\{[O]^2 K_b^2 - [O_2] K_f^2\right\} \tag{E.15}$$

$$\frac{\partial R_1}{\partial q_4} = \frac{1}{16}\left\{2[O] \cdot \{ K_b^1([O] + [N]) + K_b^2([O_2] + [N_2] + [NO])\right\} + [O]^2 K_b^1 - [O_2] K_f^1\Big\} \tag{E.16}$$

$$\frac{\partial R_1}{\partial q_5} = \frac{1}{14}\left\{[O]^2 K_b^1 - [O_2] K_f^1\right\} \tag{E.17}$$

$$\frac{\partial R_2}{\partial q_1} = \frac{1}{32}\left\{[N]^2 K_b^5 - [N_2] K_f^5\right\} \tag{E.18}$$

$$\frac{\partial R_2}{\partial q_2} = \frac{1}{28}\left\{[N]^2 K_b^5 - [N] K_f^3 - [O] K_f^4 - [O_2] K_f^5 - 2[N_2] K_f^5 - [NO] K_f^6\right\} \tag{E.19}$$

$$\frac{\partial R_2}{\partial q_3} = \frac{1}{30}\left\{[N]^2 K_b^6 - [N_2] K_f^6\right\} \quad \text{(E.20)}$$

$$\frac{\partial R_2}{\partial q_4} = \frac{1}{16}\left\{[N]^2 K_b^4 - [N_2] K_f^4\right\} \quad \text{(E.21)}$$

$$\frac{\partial R_2}{\partial q_5} = \frac{1}{14}\Big\{2[N]\{[N] K_b^3 + [O] K_b^4 + ([O_2] + [N_2]) K_b^5 + [NO] K_b^6\} + [N]^2 K_b^3 - [N_2] K_f^3\Big\} \quad \text{(E.22)}$$

$$\frac{\partial R_3}{\partial q_1} = \frac{1}{32}\left\{[O]\,[N] K_b^7 - [NO] K_f^7\right\} \quad \text{(E.23)}$$

$$\frac{\partial R_3}{\partial q_2} = \frac{1}{28}\left\{[O]\,[N] K_b^7 - [NO] K_f^7\right\} \quad \text{(E.24)}$$

$$\frac{\partial R_3}{\partial q_3} = \frac{1}{30}\left\{[O]\,[N] K_b^7 - ([O_2] + [N_2] + 2[NO] + [O] + [N]) K_f^7\right\} \quad \text{(E.25)}$$

$$\frac{\partial R_3}{\partial q_4} = \frac{1}{16}\left\{[N] \cdot ([O_2] + [N_2] + [NO] + 2[O] + [N]) K_b^7 - [NO] K_f^7\right\} \quad \text{(E.26)}$$

$$\frac{\partial R_3}{\partial q_5} = \frac{1}{14}\left\{[O]([O_2] + [N_2] + [NO] + [O] + 2[N]) K_b^7 - [NO] K_f^7\right\} \quad \text{(E.27)}$$

$$\frac{\partial R_4}{\partial q_1} = \frac{1}{32}[N] K_b^8 \quad \text{(E.28)}$$

$$\frac{\partial R_4}{\partial q_2} = 0 \quad \text{(E.29)}$$

$$\frac{\partial R_4}{\partial q_3} = -\frac{1}{30}[O] K_f^8 \quad \text{(E.30)}$$

$$\frac{\partial R_4}{\partial q_4} = -\frac{1}{16}[NO] K_f^8 \quad \text{(E.31)}$$

$$\frac{\partial R_4}{\partial q_5} = \frac{1}{14}[O_2] K_b^8 \quad \text{(E.32)}$$

$$\frac{\partial R_5}{\partial q_1} = 0 \quad \text{(E.33)}$$

$$\frac{\partial R_5}{\partial q_2} = -\frac{1}{28}[O] K_f^9 \quad \text{(E.34)}$$

$$\frac{\partial R_5}{\partial q_3} = \frac{1}{30}[N]\,K_b^9 \tag{E.35}$$

$$\frac{\partial R_5}{\partial q_4} = -\frac{1}{16}[N_2]\,K_f^9 \tag{E.36}$$

$$\frac{\partial R_5}{\partial q_5} = \frac{1}{14}[NO]\,K_b^9 \tag{E.37}$$

Appendix F

Determination of Jacobian Matrix $[M]$

Recall that equation (4.3) is given by:

$$W = [M]\, Q_c \tag{F.1}$$

where $W = -[\dot{w}_1,\ \dot{w}_2,\ \dot{w}_3,\ \dot{w}_4,\ \dot{w}_5]^T$ and $Q_c = [\rho C_1,\ \rho C_2,\ \rho C_3,\ \rho C_4,\ \rho C_5]^T$. The production rate $\dot{w}_s$ is a nonlinear polynomial which is a function of species concentrations. Thus W is not a homogeneous function of Q_c. However, the $[M]$ matrix can be derived in a similar form as the matrix $D\left(=\frac{\partial W}{\partial Q_c}\right)$ described in Appendix E. To illustrate the scheme in determination of $[M]$, an example of two species is proposed as follows:

$$\text{Example:} \qquad W = -\begin{bmatrix} \dot{w}_1 \\ \dot{w}_2 \end{bmatrix} = \begin{bmatrix} K_1 q_1^2 q_2 \\ K_2 q_1^3 q_2 \end{bmatrix}$$

$$Q_c = \begin{bmatrix} q_1 \\ q_2 \end{bmatrix}$$

defines the order of $\dot{w}_i$ as O_i; therefore,

$$O_1 = 2\ (\text{from } q_1) + 1\ (\text{from } q_2) = 3$$

$$O_2 = 3\ (\text{from } q_1) + 1\ (\text{from } q_2) = 4$$

Now the elements of $[M]$ are expressed as

$$M_{i,j} = \frac{\partial\left[\frac{\dot{w}_i}{O_i}\right]}{\partial q_j} \qquad \text{where} \quad \begin{matrix} i = 1,2 \\ j = 1,2 \end{matrix}$$

Thus

$$\begin{aligned} M_{1,1} &= \frac{2}{3}K_1 q_1 q_2 \\ M_{1,2} &= \frac{1}{3}K_1 q_1^2 \\ M_{2,1} &= \frac{3}{4}K_2 q_1^2 q_2 \\ M_{2,2} &= \frac{1}{4}K_2 q_1^3 \end{aligned}$$

Then

$$[M]\,Q_c = \begin{bmatrix} M_{1,1} & M_{1,2} \\ M_{2,1} & M_{2,2} \end{bmatrix} \cdot \begin{bmatrix} q_1 \\ q_2 \end{bmatrix} = W$$

The procedure described is used to determine the $[M]$ for five species. In fact, $[M]$ will have the same form as the $[D]$ described in Appendix E. However, all the reaction rates (K_f^i and K_b^i) employed in equations (E.13) through (E.37) should be modified as:

(i) (K_f^i) used for $[M] = K_f^i/2$ for $i = 1, \ldots 9$

(ii) (K_b^i) used for $[M] = \begin{cases} K_b^i/3 & \text{for } i = 1, \ldots 7 \\ K_b^i/2 & \text{for } i = 8, 9 \end{cases}$

Appendix G

Effects of Altitude on the Equilibrium Flows

For a closed equilibrium system which includes only oxygen, the chemical reaction can be written as:

$$M + O_2 \underset{K_b}{\overset{K_f}{\rightleftarrows}} 2O + M$$

where M can be O_2 or O. For low altitude flows, the equilibrium chemistry model provides a reasonable solution. Therefore, according to the equilibrium theory,

$$\frac{d[O]}{dt} = [M]\left([O]^2 K_b - [O_2] K_f\right) = 0 \qquad \text{(G.1)}$$

$$\text{and} \qquad [O]^2 K_b = [O_2] K_f \qquad \text{(G.2)}$$

Recall that

$$[O] = \rho C_O/16 \qquad \text{(G.3)}$$

$$\text{and} \qquad [O_2] = \rho C_{O_2}/32 \qquad \text{(G.4)}$$

where C_O and C_{O_2} are the mass-fraction of oxygen atom and molecule, respectively.

Substitution of equation (G.3) and (G.4) into (G.2) yields:

$$\rho(C_O)^2 = \left[\frac{8K_f}{K_b}\right] C_{O_2} \qquad \text{(G.5)}$$

Recall that $\frac{K_f}{K_b} = K_e$ and for an equilibrium system, K_e is a constant. Also, $C_O + C_{O_2} = 1$, equation (G.5) can be rewritten as

$$\rho\,(C_O)^2 - (1 - C_O)\,(8K_e) = 0 \tag{G.6}$$

Solving equation (G.6) for C_O, the solution is

$$C_O = \frac{-8K_e + \sqrt{(8K_e)^2 + 32\rho K_e}}{2\rho} \tag{G.7}$$

Therefore, the mass-fraction of the oxygen atom (C_o) decreases as the density (ρ) increases. In other words, the higher the density, the less dissociation. For an adiabatic system, less dissociation represents more energy saved in the translational mode and, therefore, the temperature will be higher. Since the density decreases as the altitude increases, the equilibrium temperature will decrease with increase in the altitude.

BIBLIOGRAPHY

[1] Walberg, G. D., "A Review of Aero-Assisted Orbit Transfer, " AIAA Paper 82-1378, 1982.

[2] Walberg, G. D., "Aero-Assisted Orbit Transfer Window Opens on Missions," *Astronautics and Aeronautics,* Vol. 21, No. 11, Nov. 1983, pp. 36–43.

[3] Dwoyer, D. L., Kutler, P., and Provinelli, L. A., "Retooling CFD for Hypersonic Aircraft," *Aerospace America,* Oct. 1987.

[4] Marsh, A. K., "USAF Studies Transatmosphere Vehicle," *Aviation Week and Space Technology,* Vol. 119, No. 19, Nov. 7, 1983.

[5] Williams, R. M., "National Aero-Space Plane," *Aerospace America,* Nov. 1986, pp. 18–22.

[6] Jones, J. J., "The Rationale for an Aeroassist Flight Experiment," AIAA Paper 87-1508, 1987.

[7] Lordi, J. A., "Description of Nonequilibrium Effects on Simulation of Flows About Hypersonic Vehicles," AIAA Paper 88-0476, 1988.

[8] Vincenti, W. G., Kruger, C. H., *Introduction to Physical Gas Dynamics,* Robert E. Krieger Publishing Co., Inc., 1965

[9] Maus, J. R., Griffith, B. J., Szema, K. Y., and Best, J. T., "Hypersonic Mach Number and Real Gas Effects on Space Shuttle Orbiter Aerodynamics," *Journal of Spacecraft and Rockets,* Vol. 21, No. 2, 1984, pp. 136–141.

[10] Hayes, W. D., Probstein, R. F., *Hypersonic Flow Theory,* Academic Press, 1966.

[11] Hoffmann, K. A., Chiang, T. L., and Rutledge, W. H., "Effect of Dynamic Changes in Body Configuration on Shock Structure," AIAA Paper 89–0526.

[12] Moretti, G. and Abbett, M., "A Time-Dependent Computational Method for Blunt Body Flows," *AIAA Journal,* Vol. 4, No. 12, 1966, pp. 2136–2141.

[13] Gary, J., "Numerical Computation of Hydrodynamic Flows Which Contain a Shock," Courant Institute of Mathematical Sciences Report NYO 9603, 1962, New York University.

[14] Moretti, G. and Bleich, G., "Three-Dimensional Inviscid Flow About Supersonic Blunt Cones at Angle of Attack," Sandia Laboratories Report SC-RR-68-3728, 1968. Albuquerque, New Mexico.

[15] Libby, P. A. and Williams, F. A., "Turbulent Reacting Flows," *Topics in Applied Physics,* Springer-Verlag, 1980, pp. 1–43.

[16] Gnoffo, P. A. and McCandless, R. S., "Three-Dimensional AOTV Flowfields in Chemical Nonequilibrium," AIAA Paper 86-0230.

[17] Liepmann, H. W., Roshko, A., *Elements of Gasdynamics,* by John Wiley & Sons, Inc., 1957.

[18] Erickson, W. D., Creekmore, H. S., "A Study of Equilibrium Real-Gas Effects in Hypersonic Air Nozzle, Including Charts of Thermodynamic Properties for Equilibrium Air," NASA, TN D231, 1960.

[19] Palmer, G., "An Implicit Flux-Split Algorithm to Calculate Hypersonic Flowfields in Chemical Equilibrium," AIAA Paper 87-1580.

[20] '*Nonequilibrium Effects in Supersonic Nozzle Flows,* NATO Advisory Group for Aerospace Research and Development, 1967.

[21] Blottner, F. G., "Chemical Nonequilibrium Boundary Layer," *AIAA Journal,* Vol. 2, No. 2, Feb. 1964, pp. 232–240.

[22] Blottner, F. G., "Nonequilibrium Laminar Boundary Layer Flows of Ionized Air," *AIAA Journal,* Vol. 2, No. 11, Nov. 1964, pp. 1921–1927.

[23] Moss, J. N., "Reacting Viscous-Shock-Layer Solutions with Multicomponent Diffusion and Mass Injection," NASA TR-R-411, June 1974.

[24] Davis, R. T., "Numerical Solution of the Hypersonic Viscous Shock-Layer Equations," *AIAA Journal,* Vol. 8, No. 5, May 1970, pp. 843–851.

[25] Eberhardt, S., Brown, K., "A Shock Capturing Technique for Hypersonic, Chemically Relaxing Flows," AIAA Paper 86-0231.

[26] Yu, S-T, McBride, B. J., Hsieh, K. C., and Shuen, J. S., "Numerical Solution of Hypersonic Inlet Flows with Equilibrium or Finite Rate Chemistry," AIAA Paper 88-0273.

[27] Widhopf, G. F. and Wang, J. C. T., "A TVD Finite-Volume Technique for Nonequilibrium Chemically Reacting Flows," AIAA Paper 88-2711.

[28] Grossmann, B. and Cinnella, P., "The Computation of Nonequilibrium, Chemically Reacting Flows," *Computers & Structures,* Vol. 30, No. 1/2, pp. 79–93, 1988.

[29] Li, C. P., "Implicit Methods for Computing Chemically Reacting Flow," NASA, TM-58274, Aug. 1986.

[30] Li, C. P., "Chemistry-Split Techniques for Viscous Reactive Blunt Body Flow Computations," AIAA Paper 87-0282.

[31] Balakrishnan, A., "Application of a Flux-Split Algorithm to Chemically Relaxing, Hypervelocity Blunt Body Flows," AIAA Paper 87-1578.

[32] Song, D. J. and Lewis, C. H., "Hypersonic Finite-Rate Chemically Reacting Viscous Flows Over an Ablating Carbon Surface," AIAA Paper 84-1731.

[33] Candler, Graham and MacCormack, R., "The Computation of Hypersonic Ionized Flow in Chemical and Thermal Nonequilibrium," AIAA Paper 88-0511.

[34] Gnoffo, P. A., "Hypersonic Flows Over Biconics Using a Variable-Effective-Gamma Parabolized-Navier-Stokes Code," AIAA Paper 83-1666.

[35] Balakrishnan, A., Davy, W. C., and Lombard, C. K., "Real Gas Flowfields About Three-Dimensional Configurations," *Journal of Spacecraft and Rockets,* Vol. 22, 1985, pp. 46–53.

[36] Glaz, H., Colella, P., "Nonequilibrium Effects in Oblique Shock-Wave Reflection," *AIAA Journal,* Vol. 26, No. 6, June 1988.

[37] Palmer, G., "An Improved Flux-Split Algorithm Applied to Hypersonic Flows in Chemical Equilibrium," AIAA Paper 88-2693.

[38] Park, C., "Nonequilibrium Hypersonic Flows," Sec. 5-3 (unpublished notes).

[39] "MACSYMA Reference Manual – Version 10," Mathlab Group, Laboratory for Computer Science, MIT, January 1983.

[40] Steger, J. L. and Warming, R. F., "Flux Vector Splitting of the Inviscid Gasdynamic Equations with Application to Finite Difference Methods," NASA TM-78605, June 1979.

[41] Yee, H. C., "Numerical Approximation of Boundary Conditions with Applications to Inviscid Equations of Gas Dynamics," NASA TM-81265, March 1981.

[42] Thompkins, W. T., Jr. and Bush, R. H., "Boundary Treatments for Implicit Solutions to Euler and Navier-Stokes Equations," NASA CP-2201, Oct. 1981.

[43] Anderson, D. A., Tannehill, J. C., and Pletcher, R. H., *Computational Fluid Mechanics and Heat Transfer,* McGraw-Hill Book Company, 1984.

[44] Hirschfelder, J. O., Curtiss, C. F., and Bird, R. B., *Molecular Theory of Gases and Liquids,* John Wiley & Sons, Inc., 1954.

[45] Anderson, J. D., *Modern Compressible Flow with Historical Perspective,* McGraw-Hill Book Company, 1982.

[46] Park, C., "Convergence of Computation of Chemical Reacting Flows," AIAA Paper 85-0247.

[47] Lee, J. H., "Basic Governing Equations for the Flight Regimes of Aeroassisted Orbital Transfer Vehicles," from *Thermal Design of Aeroassisted Orbital Transfer Vehicles,* Edited by Nelson, H. F., Progress in Astronautics and Aeronautics, Vol. 96.

[48] Li, C. P., "Time-Dependent Solutions of Nonequilibrium Dissociating Flow Past a Blunt Body," *Journal of Spacecraft and Rockets,* Vol. 8, No. 7, July 1971, pp. 812–814.

[49] Anderson, J. D., *Hypersonic and High Temperature Gas Dynamics,* McGraw-Hill Book Company, 1989.

[50] Anderson, J. D., "A Time-Dependent Analysis for Vibrational and Chemical Nonequilibrium Nozzle Flows," *AIAA Journal,* Vol. 8, No. 3, March 1970.

[51] Bussing, Thomas and Scott Eberhardt, "Chemistry Associated with Hypersonic Vehicles," AIAA Paper 87-1292.

[52] Cleary, J. W., "An Experimental and Theoretical Investigation of the Pressure Distribution and Flow Fields of Blunted Cones at Hypersonic Mach Numbers," NASA-TN-D-2969, Aug. 1965.

[53] Hoffmann, K. A., Chiang, T. L., and Bertin, J. J., "Effect of the Grid System on the Solution of Euler Equations," *Numerical Grid Generation in Computational Fluid Mechanics,* Pineridge Press, 1988, pp. 185–194.

[54] Huber, P. W., "Hypersonic Shock-Heated Flow Parameters for Velocities to 46,000 Feet Per Second and Altitudes to 323,000 Feet," NASA TR-R-163, Dec. 1963.

[55] Lobb, R. K., "Experimental Measurement of Shock Detachment Distance on Spheres Fired in Air at Hypervelocities," in *The High Temperature Aspects of Hypersonic Flow,* ed. W. C. Nelson, Pergammon Press, MacMillan Co., New York, 1964.

VITA

Ting-Lung Chiang was born in Taipei, Taiwan, Republic of China, on October 10, 1960, the eldest son of Gia-Kau Chiang and Sue-Yi Wang Chiang. In September, 1978, the author began his undergraduate studies at Tatung Institute of Technology, Taipei. He graduated in 1982 with the Bachelor of Science degree in Mechanical Engineering, ranking first in his graduating class. In the next two years, he was commissioned as a second lieutenant and served as a munitions technical officer in an ordnance troop of the Republic of China Army. In September of 1984, he entered the Graduate School at the University of Texas at Austin. In December of 1985, he was awarded a Master's degree in Aerospace Engineering and continued his studies toward the degree of Doctor of Philosophy in Aerospace Engineering. During these years, he was supported by the Department of Aerospace Engineering and Engineering Mechanics as a graduate teaching/research assistant.

Publications

"Effect of the Grid System on the Solution of Euler Equations," *Numerical Grid Generation in Computational Fluid Mechanics,* Pineridge Press, 1988, pp. 185–194. (With K. Hoffmann and J. Bertin)

"Inviscid Flow Field Computation of Hypervelocity Projectiles," SAE Paper 881520, 1988. (With K. Hoffmann and J. Bertin)

"Effect of Dynamic Changes in Body Configuration on Shock Structure,"
AIAA Paper 89-0526. (With K. Hoffmann and W. Rutledge)

Permanent address: 16, A2, L191, S1,
Chung-Shan Road
Yung-Ho, Taipei, Taiwan
Republic of China

This dissertation was typeset[1] with LaTeX by Jeanie Paterson.

[1] LaTeX document preparation system was developed by Leslie Lamport as a special version of Donald Knuth's TeX program for computer typesetting. TeX is a trademark of the American Mathematical Society. The LaTeX macro package for The University of Texas at Austin dissertation format was written by Khe-Sing The.